**The Hong Kong Polytechnic University**

**Department of Applied Physics**

# A New Lead-free Transparent Electro-Optic Ceramic for Optoelectronic Application

**Li Faliang**

A thesis submitted in partial fulfillment of the requirements

for the degree of Doctor of Philosophy

December 2012

# CERTIFICATE OF ORIGINALITY

I hereby declare that this thesis is my own work and that, to the best of my knowledge and belief, it reproduces no material previously published or written, nor material that has been accepted for the award of any other degree or diploma, except where due acknowledgement has been made in the text.

_____ (Signed)

LI Faliang (Name of student)

# Abstract

The most widely used electro-optic (EO) materials in the integrated optics are single crystals and ceramics. As compared to the EO single crystals, the EO ceramics have several advantages, such as strong EO responses, ceramic ruggedness, easy fabrication, low fabrication cost and large available size. However, most of the EO ceramics available in the marked contain a large amount of lead (e.g. PLZT). For environmental protection reason, there is a need of replacing the lead-based materials by environmental-friendly lead-free materials. In this work, new lead-free transparent ceramics with good EO properties have been successfully developed. Via the co-modifications with Li and Bi, the optical transparency of potassium sodium niobate $(K_{0.5}Na_{0.5})NbO_3$ ceramics has been improved. The $(K_{0.5}Na_{0.5})_{1-x}Li_xNb_{1-x}Bi_xO_3$ (KNNLB-100x) ceramics with $x \geq 0.05$ become optically transparent. If proper antireflection coatings are applied on the surfaces to eliminate the reflection loss, the transmittance of the ceramics can reach as high as 95% in the near-IR region. The ceramics also exhibit a strong linear EO effect, giving a high effective linear EO coefficient (120-200 pm/V), which is about 10 times greater than that of $LiNbO_3$ crystal (a widely used EO material in industries). The ceramics are also as good as the PMN-PT single crystals with rhombohedral structure and better than those with tetragonal structure.

Hot-press sintering is a mature technique and is widely used in industries to produce pore-free ceramics. In this work, it is used to fabricate the KNNLB ceramics so as to improve their densification and hence optical quality to crystal-like

transparency. The effects of sintering pressure on the microstructure, optical, dielectric and electro-optic properties of the KNNLB-5-2 (i.e. KNNLB-5 ceramic added with 2 mol% excess $Bi_2O_3$) are investigated. It is found that the sintering pressure is effective in enhancing the optical transmittance of the KNNLB-5-2 ceramics. A low sintering pressure (e.g. 2 MPa) is enough to enhance the optical transmittance, and the transmittance becomes saturated at around 10 MPa. Unlike the lead-based EO ceramics, the sintering pressure does not have significant effect on the grain growth. It is effective in improving the densification of the KNNLB-5-2 ceramics. The enhancement in the optical transmittance should be partly due to the reduction of defects such as pores. Due to the better densification, the dielectric properties are also improved. However, the EO responses of the ceramics are not dependent on the sintering pressure.

The effects of the co-modification with Li and Bi are investigated. It is found that the grain growth of the ceramics is considerably suppressed by the co-modification with Li and Bi. The ceramics generally possess a dense and fine-grained structure, and the light scattering by the grains (< 0.5 μm) become negligible. Our results also reveal that the co-modification induces a transformation of crystal structure from orthorhombic to nearly cubic. As a result, the optical anisotropy and hence the scattering of light at the grain boundaries are greatly reduced. The co-modification also induces a diffuse phase transition, making the ceramics become more relaxor-like and contain more polar nano-regions. The amount of domain walls and then the resulting light scattering are further eliminated. Accordingly, the KNNLB-100x ceramics with $x \geq 0.05$ become optically transparent,

giving a high optical transmittance (~60%) in the near-IR region. Owing to the large distortion of $BO_6$ octahedron and increase in $\varepsilon_r$ arisen from the substitution of $Li^+$ in the KNN lattices, the Li/Bi co-modified ceramics exhibit strong EO response, giving a large effective linear EO coefficient (120-200 pm/V).

The effects of excess $Bi_2O_3$ on the microstructure, optical, dielectric and electro-optic properties of KNNLB-5 (as examples) are investigated. It is found that the excess $Bi_2O_3$ does not have significant effect on the grain growth of the ceramics. Although the crystal structure of the ceramics added with excess $Bi_2O_3$ becomes more cubic and the ferroelectric behavior becomes more relaxor-like, their optical and EO properties remain unchanged, giving a high optical transmittance (~60%) in the near IR-region and a large effective linear EO coefficient (~120 pm/V).

The feasibility of preparing the transparent EO KNNLB ceramics by pressureless sintering is investigated. Due to the effective suppression of the grain growth by the Bi-doping, the KNNLB ceramics prepared by pressureless sintering also possess a fine-grained structure. However, our results reveal that the excess $Bi_2O_3$ is effective in promoting uniform densification under pressureless sintering. Because of the reduction of defects such as pore, the KNNLB-10 ceramics added with 4 and 6mol% excess $Bi_2O_3$ possess a dense structure and become optical transparent, exhibiting a high optical transmittance (60-70%) in the near-IR region. The good optical transparency may also be resulted from the changes to the more cubic-like crystal structure and more relaxor-like characteristics arisen from the diffusion of the excess $Bi^{3+}$ into the A-sites of the lattices. Nevertheless, the EO

responses of the ceramics become weakened, showing a low effective linear EO coefficient of 40 pm/V and 29 pm/v, respectively.

# List of Publications

Kwok, K. W., **Li, F. L.**, Lin, D. M. A novel lead-free transparent ceramic with high electro-optic coefficient. *Funct. Mater. Lett.*, Vol. 4, No.3, PP. 237-240 (2011).

**Li, F. L.**, Kwok, K. W. Fabrication of transparent electro-optic $(K_{0.5}Na_{0.5})_{1-x}Li_xNb_{1-x}Bi_xO_3$ lead-free ceramics. *J. Eur. Ceram. Soc.*, Vol. 33, No.1, PP. 123-130 (2011).

**Li, F. L.**, Kwok, K. W. $K_{0.5}Na_{0.5}NbO_3$-based Lead-free Transparent Electro-optic Ceramics Prepared by Pressureless Sintering. *J. Am. Ceram. Soc.*, in press.

Li, K., **Li, F. L.**, Wang, Y., Kwok, K. W., Chan, H. L. W. Hot-pressed $K_{0.48}Na_{0.52}Nb_{1-x}Bi_xO_3$ (x = 0.05-0.15) lead-free ceramics for electro-optic applications. *Mater. Chem. Phys.*, Vol. 131, No.1-2, PP. 320-324 (2011).

Wu, X., Kwok, K. W., **Li, F. L.** Upconversion fluorescence studies of sol–gel-derived Er-doped KNN ceramics. *J. Alloys Compd.*, Vol. 580, PP. 88-92 (2013).

# Acknowledgments

From the bottom of my heart, I would like to express my sincere gratitude firstly to Dr. Kwok, my chief supervisor, for his patience and valuable guidance throughout my years of graduate studies. Without his broad knowledge and academic insight, my study would not go on smoothly. Without his immense zeal plunged into my research work, I would not finish my thesis successfully.

I am grateful to all those who have helped me during the writing of this thesis. I would like to express my heartfelt gratitude to Prof. Li Kun, Prof. Lin Dunming, Dr. Wang Jie and Dr. Albert Choy in our department for their useful help and discussion in experiments. I would like to give my sincere thanks to my colleagues in our department, Miss. Chen Yan, Mr. Wu Xiao, Miss Chan MAN ting, Mr. Zhao Meng, and Mr. Vincent Chan, for their great help and assistance.

Last but not the least, I am deeply indebted to my family and friends for their love and support. Your support encourages me overcome various problems.

# Table of Contents

***Page***

**Abstract** **I**

**List of Publications** **V**

**Acknowledgements** **VI**

**Table of Contents** **VII**

**List of Figures** **XI**

**List of Tables** **XVII**

**List of symbols** **XIX**

**List of Acronyms** **XXI**

**Chapter 1 Introduction** ..... 1

1.1 Background ..... 1

1.2 Motivation of Research ..... 2

1.3 Research Objectives ..... 4

1.4 Thesis Outline ..... 5

**Chapter 2 Literature Review** ..... 7

2.1 Electro-Optic Effect In Crystals ..... 7

2.1.1 Refractive Index ..... 7

2.1.2 Optical Birefringence ..... 8

2.1.3 Linear EO Effect and EO Coefficients ..... 12

2.2 Relaxor Ferroelectric....15
2.3 Lead-Based EO Ceramics....16
2.3.1 PLZT Ceramics....17
2.3.2 PMN-PT Ceramics....20
2.4 Current Lead-Free EO Ceramics....21
2.5 Factors Affecting Transparency of Ceramics....24
2.6 Sodium Potassium Niobate-based Ceramics....26
2.7 Hot-Press Sintering Technique....30
**Chapter 3 Fabrication and Characterization of KNNLB Ceramics**....33
3.1 Fabrication of KNNLB Ceramics....33
3.1.1 Raw Materials....34
3.1.2 Powder Preparation....34
3.1.3 Calcination....35
3.1.4 Shaping....35
3.1.5 Binder Burnout....37
3.1.6 Sintering....38
3.1.7 Poling and Short-Circuit Aging....41
3.2 Characterization of KNNLB Ceramics....43
3.2.1 Structural Characterization....43
3.2.2 Ferroelectric Hysteresis Loop Measurement....47
3.2.3 Density Measurement....49
3.2.4 Dielectric Measurement....49
3.2.5 Linear Electro-Optic Coefficient Measurement....50
**Chapter 4 Effects of Sintering Pressure**....58

4.1 Introduction ..... 58

4.2 Optical Properties ..... 59

4.3 Microstructure ..... 62

4.4 Dielectric Properties ..... 65

4.5 Electro-Optic Properties ..... 66

4.6 Conclusions ..... 67

**Chapter 5 Effects of Lithium and Bismuth Co-modification** ..... 69

5.1 Introduction ..... 69

5.2 Optical Properties ..... 70

5.3 Microstructure ..... 73

5.4 Crystalline Structure ..... 75

5.5 Dielectric Properties ..... 78

5.6 Ferroelectric Properties ..... 85

5.7 Electro-Optic Properties ..... 86

5.8 Conclusions ..... 88

**Chapter 6 Effects of Excess Bismuth** ..... 89

6.1 Introduction ..... 89

6.2 Crystalline Structure ..... 90

6.3 Microstructure ..... 91

6.4 Optical Properties ..... 93

6.5 Dielectric Properties ..... 97

6.6 Ferroelectric Properties ..... 99

6.7 Electro-Optic Properties ..... 100

6.8 Conclusions ..... 101

**Chapter7 Preparing Transparent EO Ceramics by Pressureless Sintering**.....
.....103

7.1 Introduction .....103

7.2 Optical Properties.....104

7.3 Crystalline Structure.....105

7.4 Microstructure .....108

7.5 Dielectric Properties.....110

7.6 Ferroelectric Properties .....111

7.7 Electro-Optic Properties.....112

7.8 Conclusions .....114

**Chapter 8 Conclusions**.....115

**References** .....118

# List of Figures

Figure 2.1 Optical indicatrix or index ellipsoid for a uniaxial crystal, $n_x = n_y \neq n_z$ . The optic axis is parallel to the z-axis. ..... 11

Figure 2.2 Perovskite cell of PLZT. ..... 18

Figure 2.3 Phase diagram of PLZT at room temperature (Hartling, 1987). ..... 19

Figure 2.4 Phase diagram of the PMN-PT solid solution system (Shrout, 1990) ..... 21

Figure 2.5 Representative sample of transluent (1-x)KNN-xSTO (x=0.2) ceramics with the thickness of 0.25 mm (Kosec, 2004). ..... 22

Figure 2.6 Temperature dependence of the $\varepsilon'$, measured at several frequencies in KNN-STO samples of different compositions (Bobnar, 2004). ..... 22

Figure 2.7 Dispersion of the field induced linear EO coefficient $r_{33}$ and the quadratic $R_{33}$ coefficient in KNN–STO ceramics (Kroupa, 2005). ..... 23

Figure 2.8 Light transmission through polycrystalline (Krell, 2006). ..... 25

Figure 2.9 Influences of porosity (a) and grain size (b) on the light transmission through $Al_2O_3$ (Krell, 2006) ..... 26

Figure 2.10 Binary phase diagram $KNbO_3$-$NaNbO_3$ (Kosec, 2008) ..... 27

Figure 2.11 SEM micrographs obtained for the thermally etched surface of (a) KNN and (b) $(K_{0.5}Na_{0.5})_{0.97}Bi_{0.01}NbO_3$ ceramics (Du, 2007) ..... 29

Figure 2.12 SEM micrographs obtained for the thermally etched surface of KNLBN ceramics: (a) x=0.06, y=0.0 and (b) x=0.06, y=0.005 (Du, 2007).. ..... 30

Figure 2.13 Schematic diagram of hot pressing furnace used for bulk materials. .....31

Figure 3.1 Typical hot-pressing setup for fabricating KNNLB electro-optic ceramics.....39

Figure 3.2 Schematic diagram of the hot-press sintering program for the KNNLB ceramics.....40

Figure 3.3 Schematic diagram of the pressureless sintering program for the KNNLB ceramics.....40

Figure 3.4 Schematic diagram of polarization. .....41

Figure 3.5 Schematic diagram of the d.c. poling circuit for ceramic sample...42

Figure 3.6 Detailed geometry of X-ray reflection.....44

Figure 3.7 Schematic diagram of an SEM set-up.....45

Figure 3.8 Electron beam interaction. .....46

Figure 3.9 A typical *P-E* loop for a ferroelectric material. .....47

Figure 3.10 Schematic diagram of the hysteresis loop measurement. .....48

Figure 3.11 Schematic diagram of the dielectric measurement setup. .....50

Figure 3.12 Schematic diagram of electrodes for the EO measurement. .....51

Figure 3.13 The schematic arrangement of the optical and electronic components in the modified Sénarmont system.....52

Figure 4.1 Photographs of the KNNLB-5-2 ceramics: (a) 0 MPa; (b) 2 MPa; (c) 3 MPa; (d) 6 MPa; (e) 10 MPa; (f) 20 MPa .....59

Figure 4.2 Optical transmittance spectra for the KNNLB-5-2 ceramics.....60

Figure 4.3 Plots of $(\alpha h\nu')^2$ against $h\nu'$ for the KNNLB-5-2 ceramics with different pressure, from which the optical band gap energy $E_g$ is obtained by extrapolating the linear portion of the curve to zero. .....62

Figure 4.4 SEM micrographs of the thermally etched surfaces of the KNNLB-5-2 ceramics with different pressure. .....63

Figure 4.5 SEM micrographs of the fracture surfaces of the KNNLB-5-2 ceramics with different pressure. .....64

Figure 4.6 Variations of $\varepsilon_r$ and tanδ for the KNNLB-5-2 ceramics sintered under different pressure, measured at 100 kHz and room temperature. ..65

Figure 4.7 Variations of $r_c$ (measured at 1kHz and room temperature) for the KNNLB-5-2 ceramics sintered under different pressures. .....66

Figure 5.1 Photograph of the KNNLB-100x transparent ceramics: (a) x = 0.02; (b) x = 0.03; (c) x = 0.05; and (d) x = 0.07 .....70

Figure 5.2 Optical transmittances measured at different wavelengths for the KNNLB-100x ceramics.....71

Figure 5.3 Optical transmittance spectra for the KNNLB-100x ceramics. .....71

Figure 5.4 Plots of $(\alpha h\nu')^2$ versus $h\nu'$ for the KNNLB-100x ceramics, from which the optical band gap energy $E_g$ is obtained by extrapolating the linear portion of the curve to zero. .....72

Figure 5.5 SEM micrographs of the fracture surfaces of the KNNLB-100x ceramics: (a) x = 0; (b) x = 0.03; (c) x = 0.05; (d) x = 0.07. .....73

Figure 5.6 SEM micrographs of the thermally etched surfaces of the KNNLB-100x ceramics: (a) x = 0.04; (b) x = 0.06. .....74

Figure 5.7 XRD patterns for the KNNLB-100x ceramics. .....76

Figure 5.8 Temperature dependences of $\varepsilon_r$ for the KNNLB-100x ceramics. ....78

Figure 5.9 Plots of $1/\varepsilon_r$ versus $T$ for the KNNLB-100x ceramics. The symbols denote the experimental data, while the solid lines denote the least-squares fitting lines to the Curie-Weiss law. .....80

Figure 5.10 Variations of $T_B$, $T_m$ and $\Delta T_m$ with x for the KNNLB-100x ceramics.....80

Figure 5.11 Plots of $\ln(1/\varepsilon_r - 1/\varepsilon_m)$ versus $\ln(T-T_m)$ for the KNNLB-100x ceramics. The symbols denote the experimental data, while the solid lines denote the least-squares fitting lines to the modified Curie-Weiss law. ..81

Figure 5.12 Temperature dependences of $\varepsilon_r$ and tanδ at different frequencies for the NNLB-100x ceramics: (a) x = 0; (b) x = 0.03; (c) x = 0.06; (d) x = 0.09.....82

Figure 5.13 Variations of $\varepsilon_r$ and tanδ (measured at 100 kHz and room temperature) with x for the KNNLB-100x ceramics. .....84

Figure 5.14 Hysteresis loops of KNNLB-100x ceramics at room temperature. .....85

Figure 5.15 The composition dependence of $P_r$ and $E_c$. .....86

Figure 6.1 XRD patterns for the KNNLB-5-y ceramics. .....90

Figure 6.2 SEM images of the thermally etched surfaces of the KNNLB-5-y ceramics: (a) y=1; (b) y=3.....93

Figure 6.3 SEM images of the fracture surfaces of the KNNLB-5-y ceramics: .....93

Figure 6.4 Photograph of the KNNLB-5-y transparent ceramics: (a) y=0; (b) y=1; (c) y=2; (d) y=3; (e) y=4.....94

Figure 6.5 Optical transmittances measured at different wavelength for the KNNLB-5-y ceramics .....95

Figure 6.6 Optical transmittance spectra for the KNNLB-5-y ceramics.....95

Figure 6.7 Plots of $(\alpha hv')^2$ versus $hv'$ for the KNNLB-5-y ceramics, from which the optical band gap energy $E_g$ obtained by extrapolating the linear region of the curve to zero.....96

Figure 6.8 Temperature dependence of $\varepsilon_r$ for the KNNLB-5-y ceramics. .....97

Figure 6.9 Variations of $\varepsilon_r$ and tanδ with y for KNNLB-5-y ceramics at room temperature and 100 kHz .....98

Figure 6.10 Hysteresis loops (at 100 Hz) of KNNLB-5-y ceramics at room temperature.....99

Figure 6.11 Variations of $P_r$ and $E_c$ for KNNLB-5-y ceramics at room temperature and 100 Hz .....100

Figure 6.12 Variations of $r_c$ and $P_s$ (at room temperature) for the KNNLB-5-y ceramics.....101

Figure 7.1 Photograph of the KNNLB-10-z transparent ceramics with the thickness of 0.5mm: (a) z=0; (b) z=2; (c) z=4; (d) z=6; (e) z=8. .....104

Figure 7.2 (a) Optical transmittance spectra for the KNNLB-10-z ceramics; (b) Optical transmittances measured at 633 nm for the KNNLB-10-z ceramics .....105

Figure 7.3 XRD patterns for the KNNLB-10-z ceramics. .....106

Figure 7.4 X-ray photoelectron spectroscopy (XPS) core-level spectrum of Bi4*f* for the KNNLB-10-6 ceramic .....107

Figure 7. 5 SEM images of the fracture surfaces of the KNNLB-10-z ceramics: .....108

Figure 7. 6 Photographs of the KNNLB-10-z ceramics. .....109

Figure 7.7 Temperature dependence of $\varepsilon_r$ and tanδ for the KNNLB-10-z ceramics at 100 kHz .....110

Figure 7.8 Hysteresis loops (at 100 Hz) of KNNLB-10-z ceramics at room temperature .....111

Figure 7. 9 The composition dependence of $P_r$ and $E_c$ .....112

Figure 7. 10 The plot of the phase retardations as a function of an a.c. applied field with a modulation frequency 1 kHz for the KNNLB-10-4 and KNNLB-10-4 ceramics .....113

# List of Tables

Table 2.1 History of the development of electro-optic ceramic.....17

Table 2.2 EO coefficients of PLZT with different compositions (Moulson, 2003, Bailey, 2004).....20

Table 2.3 Some physical properties of air-fired and hot-pressed ceramic.....32

Table 3.1 Feed materials for various shaping methods and the type of product.. ..... 36

Table 4.1 $E_g$ for the KNNLB-5-2 ceramics at different pressure.....62

Table 4.2 Average grain size of KNNLB-5-2 ceramics at different applied pressure.....64

Table 4.3 The density of KNNLB-5-2 ceramics at different applied pressure.64

Table 5.1 Optical band gap energy $E_g$ for the KNNLB-100x ceramics..... 72

Table 5.2 Density for the KNNLB-100x ceramics ..... 74

Table 5.3 Average grain size for the KNNLB-100x ceramics.....74

Table 5.4 Lattice constants *a*, *b* and *c* for the KNNLB-100x ceramics ..... 77

Table 5.5 Degree of diffuseness $\gamma$ for the KNNLB-100x ceramics ..... 81

Table 5.6 Effective linear EO coefficient $r_c$ for the KNNLB-100x ceramics..87

Table 6.1 Lattice constants *a*, *b* and *c* for the KNNLB-5-y ceramics.....91

Table 6.2 Density results for the KNNLB-5-y ceramics..... 92

Table 6.3 Average grain size for the KNNLB-5-y ceramics.....92

Table 6.4 Optical band gap energy $E_g$ for the KNNLB-5-y ceramics.....96

Table 7.1 Lattice constants *a*, *b* and *c* for the KNNLB-10-z ceramics ..... 107

Table 7.2 Average grain size for the KNNLB-10-z ceramics..... 109

Table 7.3 Density results for the KNNLB-10-z ceramics ..... 109

# List of Symbols

| Symbol | Description |
|---|---|
| $n$ | Refractive index |
| $n_e$ | Extraordinary refractive index |
| $n_o$ | Ordinary refractive index |
| $\Delta n$ | Birefringence, $n_e$- $n_o$ |
| $v$ | Speed of light |
| $c$ | The speed of light in vacuum |
| $\mu$ | Permeability |
| $\varepsilon_r$ | Relative permittivity |
| $\varepsilon_0$ | Vacuum permittivity |
| $D$ | Dielectric displacement |
| $E$ | Electric field |
| $\varepsilon_{ij}$ | Dielectric permittivity tensor |
| $k$ | Wave vector |
| U | Energy density |
| $\eta$ | Impermeability |
| $P$ | Electric polarization |
| $P_r$ | Remnant polarization |
| $P_s$ | Spontaneous polarization |
| $\chi$ | Susceptibility |
| $r_{ijk}$ | Linear electro-optic coefficient |
| $R_{ijkl}$ | Quadratic electro-optic coefficient |
| $r_c$ | Effective linear electro-optic coefficient |
| $R_c$ | Effective quadratic electro-optic coefficient |
| $\lambda$ | Wavelength |
| $Y$ | Young's modulus |
| $d_{33}$, $d_{31}$ | Piezoelectric Constant |
| $Q_m$ | Mechanical quality factor |

| | |
|---|---|
| $g_{31}$, $g_{33}$ | Piezoelectric voltage constant |
| $k_t$, $k_p$ | Electromechanical coupling factor |
| $T_C$ | Curie temperature |
| $L$ | Thickness of sample |
| $E_c$ | Electric coercive field |
| $A$ | Area of sample |
| $\rho$ | Density |
| $C$ | Capacitance |
| tanδ | Dielectric loss |
| Γ | Phase retardation |
| $d$ | Electrode spacing for EO sample |
| T | Transmittance |
| $E_g$ | Optical band gap energe |
| $\alpha$ | Absorption coefficient |
| $h$ | Plank's constant |
| $v'$ | Photon frequency |
| $T_m$ | The temperature at maximum $\varepsilon_r$ |
| $T_B$ | Curie-Weiss temperature |
| $\gamma$ | Diffusion coefficient |
| $a$, $b$, $c$ | Lattice constant |

# List of Acronyms

| Acronyms | Description |
|---|---|
| EO | electro-optic |
| ADP | ammonium dihydrogen phosphate, $NH_4H_2PO_3$ |
| KDP | potassium dihydrogen phosphate, $KH_2PO_4$ |
| KNN | sodium potassium niobate, $(K_{0.5}Na_{0.5})NbO_4$ |
| PLZT | lanthanum-modified lead zirconate titanate, $Pb_{1-x}La_{x(}Zr_y,Ti_{1-y})_{1-0.25x}O_3$ |
| XRD | X-ray diffraction |
| LNO | $LiNbO_3$ |
| PZT | lead zirconate titante, $Pb(Zr_x,Ti_{1-x})O_3$ |
| KNNLB | $(K_{0.5}Na_{0.5})_{1-x}Li_xNb_{1-x}Bi_xO_3$ |
| PVA | polyvinyl alcohol |
| SEM | scanning electron microscope |
| *P-E* loop | ferroelectric hysteresis loop |
| PERPIC | ferroelectric picture |
| FERICON | a new type of image storage and display device |

# Chapter 1 Introduction

## 1.1 Background

In 1875 John Kerr carried out experiments on glass and observed a quadratic dependence of refractive index ($n$) on electric field $E$. This is called the Kerr electro-optic (EO) effect. A linear EO effect called Pockels effect was observed in quartz by Wilhelm Röntgen and August Kundt independently in 1883. Pockels analyzed the phenomenon and pointed that the EO effect was due to the direct field-induced change of refractive index. A theory of the linear EO effect was then developed by him in 1894 (Pockels, 1894). Only non-centrosymmetric crystal materials exhibit the Pockels EO effect, while all transparent media basically show the Kerr EO effect. The quadratic effect is typically much weaker than the linear effect.

For most of the materials, a relatively high electric voltage (tens and even hundreds of kilovolts) is needed to induce the EO effects, in particular for the Kerr effect. So the investigation of the EO effects and their applications had been restricted for a long time. Since the discovery of strong electro-optical properties in crystals of KDP ($KH_2PO_4$) (Bass, 1962) and some isomorphous compounds, the study of electro-optics has attracted considerable attention. Nowadays, electro-optical crystals have been widely used in modulators and deflectors. The electro-optic materials can also manipulate the laser input without the use of the

mechanical components. The resulting single-element beam control leads to rapid and programmable modulation with low optical loss.

## 1.2 Motivation of Research

In recent years, the demand for developing new EO materials with high performance continues to increase along with the rapid development of optoelectronic techniques. There are disadvantages for the existing EO materials. For liquid crystals, the main disadvantage is the stability of the molecules. Under an external electric field, the charge amount within the liquid crystal layer changes with time, and thus destabilizing the state of the liquid crystal molecules (Konuma, 2009). On the other hand, the photo- and thermal-stability with time are the main drawbacks of EO polymers (Kuo, 2006, Sinyukov, 2004). Because of the small size, the application of EO film is limited. EO single crystals also have drawbacks such as low electro-optic effect, small size, susceptibility to moisture, high cost, and difficulty in being prepared with proper chemical stoichiometry, which make them difficult for widespread applications. In contrast, electro-optic ceramics have advantages of stronger EO responses, ceramic ruggedness, easy fabrication, low fabrication cost and large available size, and hence they have been used in various EO applications, such as optical filters, switches, modulators and data processing devices (Hartling, 1987, Jiang, 2005).

Nowadays the most widely used EO ceramics in the market are lanthanum-modified lead zirconate titanate-based EO ceramics (Hartling, 1987, Uchino, 2000) because of their strong EO effect. However, the high lead content of

the materials raises serious environmental concerns. It has been known that lead can get into the environment during the sintering processing because of the evaporation. Once absorbed by a human body, the toxicity of lead presents serious threat to human health. Moreover, lead can accumulate in human organisms and is difficult to remove.

Potassium sodium niobate ($K_{0.5}Na_{0.5}NbO_3$) is considered as one of the best candidates for lead-free piezoelectric ceramics and has been studied extensively (Saito, 2004, Kakimoto, 2004, Guo, 2005). Because of the high volatility of alkali components during sintering, pure KNN ceramic is difficult to densify by ordinary sintering method. A number of studies have been carried out to improve the sinterability by using the formation of new solid solutions with other ferroelectrics, such as KNN-$BaTiO_3$ (Park, 2006), KNN-$SrTiO_3$ (Bobnar, 2004), KNN-$LiNbO_3$ (Kakimoto, 2004), KNN-$LiSbO_3$ (Zang, 2006), and KNN-$LiTaO_3$ (Guo, 2005). The other way to improve the densification of KNN ceramics is using special sintering methods, such as hot-pressing (Erling, 2005), hot isostatic pressing (HIP) (Jaeger, 1962), cold isostatic pressing (CIP) (Kakimoto, 2004), spark plasma sintering (Wang, 2004, Wang, 2002), and hot forging (Ahn, 1987).

Although the sinterability of KNN can be improved by different methods, there are few works reporting an improvement in the optical properties of the ceramics. It has been known that the light scattering at large grains, grain boundaries and pores can reduce the optical property of a material. Fine grains, less grain boundaries, good density and pure phase are hence the essential factors for ceramics possessing good optical property (Andreas, 2006, Moulson, 2003, Grimm, 1971). Obviously, good optical property is the prerequisite of an EO ceramic.

It has been shown that the grain growth of KNN ceramics is dramatically suppressed and the density is enhanced with Bi doping (Wang, 2008). Due to the large difference in ionic radii, the substitution of $Li^+$ in the KNN lattices will cause a large distortion of the $BO_6$ octahedron (Mgbemere, 2011, Rubio-Marcos, 2010), which can improve the EO effect (Shih, 1982). These hence suggest that, by the co-modification of Li and Bi, the KNN ceramic may exhibit good optical and EO properties. However, there are no studies investigating the optical or EO properties of Li and Bi-doped KNN ceramics.

The hot-press sintering method was first reported by Hartling (Hartling 1971) for fabricating PLZT transparent ceramics (Stojanovic, 2001, Santos, 2001, Stojanovic, 2000). This technique is promising and has been used to prepare dense and high performance KNN ceramics successfully (Jaeger, 1962).

## 1.3 Research Objectives

The objectives of this study are as follows:

1) To develop a new lead-free transparent ceramic with strong EO response and high transparency for optoelectronic applications. The potassium sodium niobate $(K_{0.5}Na_{0.5})NbO_3$ perovskite solid solution will be used as the base composition in this investigation. Modifiers such as lithium and bismuth will be adopted to improve the EO response as well as the transparency of the ceramics.
2) To determine the optimum processing conditions, including the type and amount of modifiers and the sintering methods, for fabricating dense and

transparent ceramics. The hot-press sintering technique will be used as the main method for fabricating the ceramics.

3) To study the crystalline structure and physical properties of the ceramics: the physical properties to be investigated include the phase transition, ferroelectric properties, optical properties and electro-optic properties.
4) To investigate the relationship between the composition, processing conditions and physical properties of the ceramics.

## 1.4 Thesis Outline

The main objective of the present work is to fabricate Li and Bi co-modified KNN (KNNLB) transparent EO ceramics by hot-press sintering. The optical properties, microstructure, dielectric, ferroelectric and EO properties of the ceramics are studied. The thesis consists of eight chapters:

Chapter 1 gives a brief introduction of the motivation and objectives of the present work. The contents of the thesis are also outlined in this chapter.

Chapter 2 gives a review of the EO materials. According to the crystal morphology, the common electro-optic materials can be divided into five main groups: liquid crystals, single crystals, organic polymers, films and ceramics. The limitations of various EO materials are also presented.

Chapter 3 introduces the fabrication methods for KNNLB ceramics. The characterization methods of the crystalline structure, ferroelectric, dielectric, optical and electro-optic properties are described.

Chapter 4 reports the effects of the sintering pressure on the microstructure

and optical properties of the ceramics.

Chapter 5 shows the effects of Bi and Li on the microstructure and physical properties of the ceramics fabricated by hot-press sintering. The physical properties include the phase transition, ferroelectric properties, optical properties and electro-optic properties.

Chapter 6 discusses the effects of excess Bi on the physical properties of the KNNLB ceramics prepared by hot-press sintering.

Chapter 7 presents the fabrication of the KNNLB ceramics by pressureless sintering.

Conclusions are given in Chapter 8.

# Chapter 2 Literature Review

This chapter covers the background theory of electro-optic (EO) effect, relaxor behavior and reviews of current EO ceramics. A review of current research status of lead-free materials with special focus on sodium potassium niobate (KNN), which is the basic material system in this work, is also given. As good optical property is the prerequisite for an EO ceramic, the factors that affect the optical property are reviewed. The hot-press sintering method, which has been used to improve the sinterability of ceramics in this work, is reviewed.

## 2.1 Electro-Optic Effect In Crystals

### 2.1.1 Refractive Index

Refraction is the bending of a wave when it enters from one medium to another medium where it travels at a different speed. The bending depends on the indexes of refraction (refractive indexes) of the two media and is described quantitatively by Snell's Law, which relates the angle of incidence $\theta_1$ to angle of refraction $\theta_2$ as:

$$\frac{\sin\theta_1}{\sin\theta_2} = \frac{v_1}{v_2} = \frac{n_1}{n_2} \tag{2.1}$$

where $v_1$ and $v_2$ are the wave speeds in the respective media, and $n_1$ and $n_2$ are the refractive indexes.

The refractive index of an isotropic material is defined as (Nye, 1976):

$$n = \frac{c}{v} \tag{2.2}$$

where $c$ is the speed of light in vacuum and $v$ is the speed of light in the material.

The speed of light in a vacuum is given by

$$c = \frac{1}{\sqrt{\mu_0 \varepsilon_0}} \tag{2.3}$$

where $\mu_0$ and $\varepsilon_0$ are the permeability and permittivity of vacuum respectively. According to Maxwell's equations, the speed of electromagnetic wave in a material can be expressed as

$$v = \frac{1}{\sqrt{\mu_0 \mu_r \varepsilon_0 \varepsilon_r}} \tag{2.4}$$

where $\mu_r$ and $\varepsilon_r$ are the relative permeability and relative permittivity of the material, respectively (Maxwell's equations n.d.). For non-magnetic materials, the relative permeability ($\mu/\mu_0$) is approximately equal to 1, and then $v$ can be written as:

$$v = \frac{c}{\sqrt{\varepsilon_r}} \tag{2.5}$$

Substituting Eq. 2.5 into Eq. 2.2 gives:

$$n = \sqrt{\varepsilon_r} \tag{2.6}$$

### 2.1.2 Optical Birefringence

For an anisotropic material, the dielectric displacement $D$ is related to the applied electric field $E$ as:

$$D_i = \varepsilon_0 (\varepsilon_r)_{ij} E_j \tag{2.7}$$

where $i, j = 1, 2, 3$. Eq. 2.7 can also be written in the form of matrix:

$$\begin{bmatrix} D_1 \\ D_2 \\ D_3 \end{bmatrix} = \varepsilon_0 \begin{bmatrix} (\varepsilon_r)_{11} & (\varepsilon_r)_{12} & (\varepsilon_r)_{13} \\ (\varepsilon_r)_{21} & (\varepsilon_r)_{22} & (\varepsilon_r)_{23} \\ (\varepsilon_r)_{31} & (\varepsilon_r)_{32} & (\varepsilon_r)_{33} \end{bmatrix} \begin{bmatrix} E_1 \\ E_2 \\ E_3 \end{bmatrix} \tag{2.8}$$

For a lossless and non-optically active material, the relative permittivity tensor $(\varepsilon_r)_{ij}$ is represented by a real symmetric matrix, in which $(\varepsilon_r)_{xy}=(\varepsilon_r)_{yx}$, $(\varepsilon_r)_{yz}=(\varepsilon_r)_{zy}$ and $(\varepsilon_r)_{zx}=(\varepsilon_r)_{xz}$. By rotating the coordinate axes, a new diagonal matrix can be obtained:

$$\begin{bmatrix} D_x \\ D_y \\ D_z \end{bmatrix} = \varepsilon_0 \begin{bmatrix} (\varepsilon_r)_{xx} & 0 & 0 \\ 0 & (\varepsilon_r)_{yy} & 0 \\ 0 & 0 & (\varepsilon_r)_{zz} \end{bmatrix} \begin{bmatrix} E_x \\ E_y \\ E_z \end{bmatrix} \tag{2.9}$$

The new coordinate system is called the principal-axis system.

The energy density U is given as:

$$U = \frac{1}{2} D_i E_i \tag{2.10}$$

For convenience, a relative impermeability tensor $\eta_{ij}$ is defined as:

$$\eta_{ij} = \frac{1}{(\varepsilon_r)_{ij}} \tag{2.11}$$

Since $(\varepsilon_r)_{ij}$ is real and symmetric, $\eta_{ij}$ is also real and symmetric. From Eq. 2.7 and Eq. 2.11,

$$E_i = \frac{1}{\varepsilon_0} \eta_{ij} D_j \tag{2.12}$$

Substituting Eq. 2.12 into Eq. 2.10 gives

$$\eta_{11}D_1^2 + \eta_{22}D_2^2 + \eta_{33}D_3^2 + 2\eta_{23}D_2D_3 + 2\eta_{31}D_3D_1 + 2\eta_{12}D_1D_2 = 2U\varepsilon_0 \tag{2.13}$$

This is an equation for an ellipsoid of constant energy density in the *D* space.

Let

$$X_i = \frac{D_i}{\sqrt{2\varepsilon_0 U}} \tag{2.14}$$

Where $i$=1, 2 and 3. Eq. 2.13 becomes

$$\eta_{11}X_1^{\ 2} + \eta_{22}X_2^{\ 2} + \eta_{33}X_3^{\ 2} + 2\eta_{23}X_2X_3 + 2\eta_{31}X_3X_1 + 2\eta_{12}X_1X_2 = 1 \tag{2.15}$$

Substituting Eq. 2.6 and Eq. 2.11 into Eq. 2.15 gives

$$\frac{X_1^{\ 2}}{n_{11}^2} + \frac{X_2^{\ 2}}{n_{22}^2} + \frac{X_3^{\ 2}}{n_{33}^2} + 2\frac{X_2X_3}{n_{23}^2} + 2\frac{X_3X_1}{n_{31}^2} + 2\frac{X_1X_2}{n_{12}^2} = 1 \tag{2.16}$$

The surface described by Eq.2.16 is called the optical indicatrix or index ellipsoid. For simplicity, Eq. 2.16 (written in tensor notation) can be re-written in matrix notation as:

$$\frac{X_1^{\ 2}}{n_1^2} + \frac{X_2^{\ 2}}{n_2^2} + \frac{X_3^{\ 2}}{n_3^2} + 2\frac{X_2X_3}{n_4^2} + 2\frac{X_3X_1}{n_5^2} + 2\frac{X_1X_2}{n_6^2} = 1 \tag{2.17}$$

In rewriting the equation, the scheme: 11 $\rightarrow$ 1, 22 $\rightarrow$ 2, 33 $\rightarrow$ 3, 23 or 32 $\rightarrow$ 4, 13 or 31 $\rightarrow$ 5 and 12 or 21 $\rightarrow$ 6 is adopted. In the principal-axis system, Eq. 2.17 becomes

$$\frac{x^2}{n_x^2} + \frac{y^2}{n_y^2} + \frac{z^2}{n_z^2} = 1 \tag{2.18}$$

where $n_1$, $n_2$ and $n_3$ are called the principal refractive indexes. Eq. 2.18 defines the optical indicatrix in the principal-axis system as shown in Fig. 2.1. $n_x$, for example, is the refractive index for a plane wave with the polarization parallel to the $x$ axis and travelling along a direction normal to the x-axis.

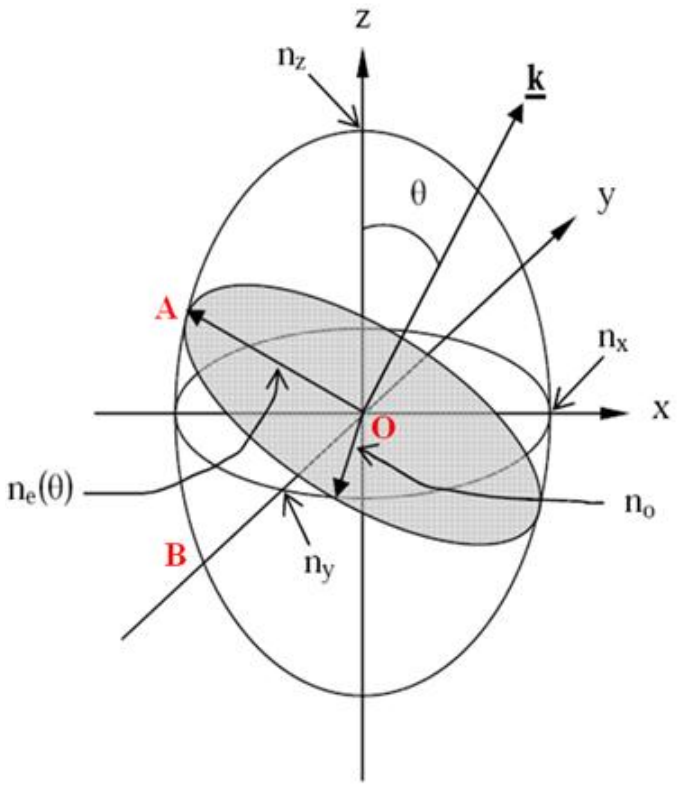


Figure 2.1 Optical indicatrix or index ellipsoid for a uniaxial crystal, $n_x = n_y \neq n_z$ . The optic axis is parallel to the z-axis.

For a uniaxial crystal (e.g.; crystals with hexagonal, tetragonal and trigonal symmetry) with an optic axis along z axis, $n_x = n_y = n_o$ (ordinary refractive index) and $n_z = n_e$ (extraordinary refractive index). The optic axis is also called the extraordinary axis. For positive uniaxial crystals (e.g.; quartz $SiO_2$ and rutile $TiO_2$), $n_e > n_o$, i.e.; the wave with the polarization parallel to the z axis travels slower than the wave with the polarization parallel to the x or y axis (Eq. 2.2). On the other hand, negative uniaxial crystals (e.g. calcite $CaCO_3$ and ruby $Al_2O_3$) have $n_e < n_o$. The difference between the two indexes, $\Delta n = n_e - n_o$, is called the birefringence. So, there will be no birefringence for a plane wave travelling along the optical axis.

For a plane wave travelling along an arbitrary direction $\vec{k}$ in a positive uniaxial crystal, the corresponding refractive indexes can be determined from the optical indicatrix as follows:

(1) Draw a straight line through the origin and along the wave vector $\vec{k}$.

(2) Locate the central section of the indicatrix which passes through the origin and is normal to $\vec{k}$ (i.e., shaded region in Fig. 2.1). In general, it will be an ellipse.

(3) The axes of the elliptical section define the polarization directions of the two waves with the wave vector $\vec{k}$ that can propagate through the crystal.

(4) The wave with the polarization parallel to the major axis will travel at a slower speed, and the corresponding refractive index $n_e(\theta)$ is equal to the semi-axis OA.

(5) The wave with the polarization parallel to the minor axis will travel at a faster speed, and the corresponding refractive index $n_o(\theta)$ is equal to the semi-axis OB.

(6) If the angle between the wave vector $\vec{k}$ and the optic axis is $\theta$, $n_o(\theta)$ is constant, while $n_e(\theta)$ is given as:

$$\frac{1}{n_e^2(\theta)} = \frac{\cos^2\theta}{n_o^2} + \frac{\sin^2\theta}{n_e^2} \tag{2.19}$$

### 2.1.3 Linear EO Effect and EO Coefficients

When an external electric field is applied to a crystal, ion displacement is induced and the refractive index is changed. This is called the electro-optic (EO) effect. Generally, subject to a low-frequency or static electric field, the charge distribution in the crystal will be re-arranged. In a macroscopic context the EO

effect can be described starting from a power series expansion of the polarization *P* (Goovaerts, 2001)

$$P_i = \varepsilon_0(\chi_{ij}^{(1)} + \chi_{ijk}^{(2)}E_k + \chi_{ijkl}^{(3)} + \cdots)E_j \tag{2.20}$$

where $\chi_{ij}^{(1)}$ is the linear susceptibility, $\chi_{ijk}^{(2)}$ and $\chi_{ijkl}^{(3)}$ are the second- and third-order nonlinear susceptibilities of the material, respectively, $E_j$ is the electric field, *i*, *j*, *k*, *l* = 1, 2, 3, 4. For low $E_j$, Eq. 2.20 can be approximated as

$$P_i = \varepsilon_0\chi_{ij}^{(1)}E_j \tag{2.21}$$

For an isotropic material,

$$D_i = \varepsilon_0 E_i + P_i \tag{2.22}$$

Combining Eq. 2.6, 2.7, 2.21 and 2.22 gives:

$$n_{ij}^2 = (\varepsilon_r)_{ij} = \delta_{ij} + \chi_{ij}^{(1)} \tag{2.23}$$

This describes the linear optical properties of a medium.

When an electric field is applied to a nonlinear optical material, the second term containing $\chi_{ijk}^{(2)}$ in Eq. 2.20 causes a change in the refractive index. According to Eq. 2.20, the change is linearly proportional to the electric field. This linear EO effect is called the Pockels effect. Similarly, the third term containing $\chi_{ijkl}^{(3)}$ in Eq. 2.20 causes a change in the refractive index that is proportional to the square of the electric field. This quadratic EO effect is called Kerr effect.

For convenience, the change in the refractive index can be described as the modulation of the optical impermeability by the external electric field

$$\Delta\eta_{ij} = \Delta(\frac{1}{n_{ij}^2}) = r_{ijk}E_k + R_{ijkl}E_kE_l + \cdots \tag{2.24}$$

where *i*, *j*, *k*, *l* = 1, 2, 3, 4. Eq. 2.24 can also be written in matrix notation as:

$$\Delta\eta_p = \Delta\left(\frac{1}{n_p^2}\right) = r_{pk}E_k + R_{pq}E_kE_l + \cdots \tag{2.25}$$

where *p*, *q* = 1, 2, 3, .., 6. The higher-order terms are neglected for low electric field. The first and second terms represent the linear EO effect (Pockels effect) and quadratic EO effect (Kerr effect), respectively. $r_{pk}$ and $R_{pq}$ are the linear and quadratic EO coefficients, respectively.

For the linear EO effect,

$$\Delta\left(\frac{1}{n_p^2}\right) = r_{pk}E_k \tag{2.26}$$

or

$$\begin{bmatrix} \Delta\left(\frac{1}{n_1^2}\right) \\ \Delta\left(\frac{1}{n_2^2}\right) \\ \Delta\left(\frac{1}{n_3^2}\right) \\ \Delta\left(\frac{1}{n_4^2}\right) \\ \Delta\left(\frac{1}{n_5^2}\right) \\ \Delta\left(\frac{1}{n_6^2}\right) \end{bmatrix} = \begin{bmatrix} r_{11} & r_{12} & r_{13} \\ r_{21} & r_{22} & r_{23} \\ r_{31} & r_{32} & r_{33} \\ r_{41} & r_{42} & r_{43} \\ r_{51} & r_{52} & r_{53} \\ r_{61} & r_{62} & r_{63} \end{bmatrix} \begin{bmatrix} E_1 \\ E_2 \\ E_3 \end{bmatrix} \tag{2.27}$$

where the $6\times3$ matrix, $r_{pk}$, is also called the first-order EO matrix. The linear electro-optic effect occurs only in materials lacking inversion symmetry. Depending on the crystal symmetry, some of the EO coefficients may become zero and some of them may be related to each other. For example, the EO matrix for crystals possessing the point group symmetry $\bar{4}2m$ (such as ADP and KDP) has the form as:

$$r_{pk} = \begin{bmatrix} 0 & 0 & 0 \\ 0 & 0 & 0 \\ 0 & 0 & 0 \\ r_{41} & 0 & 0 \\ 0 & r_{41} & 0 \\ 0 & 0 & r_{63} \end{bmatrix} \tag{2.28}$$

For crystals of class 3m (such as $LiNbO_3$), the EO matrix has the form as:

$$r_{pk} = \begin{bmatrix} 0 & -r_{22} & r_{13} \\ 0 & r_{22} & r_{13} \\ 0 & 0 & r_{33} \\ 0 & r_{42} & 0 \\ r_{41} & 0 & 0 \\ r_{22} & 0 & 0 \end{bmatrix} \tag{2.29}$$

And the EO matrix for crystals of the class 4mm (such as $BaTiO_3$) has the form as:

$$r_{pk} = \begin{bmatrix} 0 & 0 & r_{13} \\ 0 & 0 & r_{13} \\ 0 & 0 & r_{33} \\ 0 & r_{51} & 0 \\ r_{51} & 0 & 0 \\ 0 & 0 & 0 \end{bmatrix} \tag{2.30}$$

## 2.2 Relaxor Ferroelectric

Materials exhibiting a domain structure and spontaneous polarization at temperatures below the Curie point are defined as ferroelectric materials. The spontaneous polarization makes the ferroelectric material present polarization-electric field (*P*-*E*) hysteresis loop. Relaxor ferroelectrics are those

ferroelectric materials that exhibit a broad phase transition from the paraelectric to ferroelectric state, a strong frequency dependence of the relative permittivity and a temperature-dependant remnant polarization. The relative permittivity maximum of relaxor ferroelectrics does not correspond to a transition from non-polar phase to a ferroelectric polar phase, such as lead magnesium niobate (Smolenskii, 1958). Frequency dispersion of the dielectric maximum, slim hysteresis loop, and the optical isotropy at the temperature below the dielectric maximum without external field is another distinct features for the relaxor ferroelectrics (Cross, 1987).

For relaxor ferroelectrics, the temperature-dependent relative permittivity obeys the modified Curie-Weiss law (Uchino, 1982),

$$\frac{1}{\varepsilon_r} - \frac{1}{\varepsilon_m} = \frac{(T - T_m)^{\gamma}}{C_1} \tag{2.31}$$

where $\varepsilon_m$ is the maximum value of $\varepsilon_r$, $T_m$ is the temperature of $\varepsilon_m$, $C_1$ is the Curie-like constant, and $\gamma$ is the diffusion coefficient. $\gamma$ can have a value ranging from 1 for a normal ferroelectric to 2 for an ideal relaxor ferroelectric. Owing to the large dielectric and electromechanical effects, relaxor ferroelectrics are widely used in capacitors, sensors, actuators, and transducers (Newnham, 1991, Uchino, 1996).

## 2.3 Lead-Based EO Ceramics

The lead-based EO ceramics mainly include $(Pb_{1-x}La_x)(Zr_yTi_{1-y})_{1-x/4}O_3$ with $0.08<x<0.12$ (PLZT) and $(1-x)Pb(Mg_{1/3}Nb_{2/3})O_3$-$xPbTiO_3$ with $0.10<x<0.35$ (PMN-PT). These lead-based EO ceramic are introduced in the following sections.

### 2.3.1 PLZT Ceramics

Because of the porosity, grain boundaries, and internal refraction at boundaries, transparent ceramics could not be fabricated before 1960s. By late 1969, the first transparent ferroelectric ceramic $Pb_{1-x}La_x(Zr_yTi_{1-y})_{1-x/4}O_3$ (PLZT) was successfully developed (Hartling, 1971). Since then, various methods have been developed for fabricating the transparent EO ceramics (Thomson, 1974, Murata, 1976, Snow, 1973). The history from 1965 to 1979 of the evolution of the EO ceramics is outlined in Table 2.1 (Dekker, 1991).

Table 2.1 History of the development of electro-optic ceramic.

| Year | Development |
|---|---|
| 1965 | Hot-pressing techniques developed for PZT ceramics |
| 1966 | Optical scattering properties of Fe materials measured, polarization dependence defined |
| 1967 | Optical birefringent properties of FE materials measured, polarization dependence defined |
| 1968 | Reduced scattering measured in La-doped PZT |
| 1969 | Development of transparent PLZT ceramics; phase diagram and properties defined |
| 1970 | Development of oxygen hot-press technique |
| 1970 | Development of chemical process for EO ceramics |
| 1970 | FERPIC strain-biased device for image storage |
| 1971 | EO goggles for eye protection; transverse –mode device |
| 1971 | Ceramic device for image storage |
| 1971 | Longitudinal mode in quadratic PLZT reported |
| 1972 | PLZT ceramics sintered to optical quality |
| 1972 | FERICON device for image storage |
| 1974 | Photoinduced $\Delta n$ changes in PLZT reported |
| 1975 | Vacuum/oxygen-sintered transparent PLZT ceramics |
| 1976 | Photoferroelectric image storage devices |

1979 Ion implantation in image storage devices

Owing to the large nonlinear EO coefficient, fast responses and high optical transmittance in the visible wavelength region, PLZT ceramics are good candidates for optical waveguide applications. PLZT possesses a perovskite structure with the formulation of $ABO_3$, as shown in Fig. 2.2. $La^{3+}$ substitutes part of $Pb^{2+}$ and they occupy the A-site, while the B-site is occupied by $Zr^{4+}$ and $Ti^{4+}$. The structure is shown in Fig. 2.2. is undistorted.

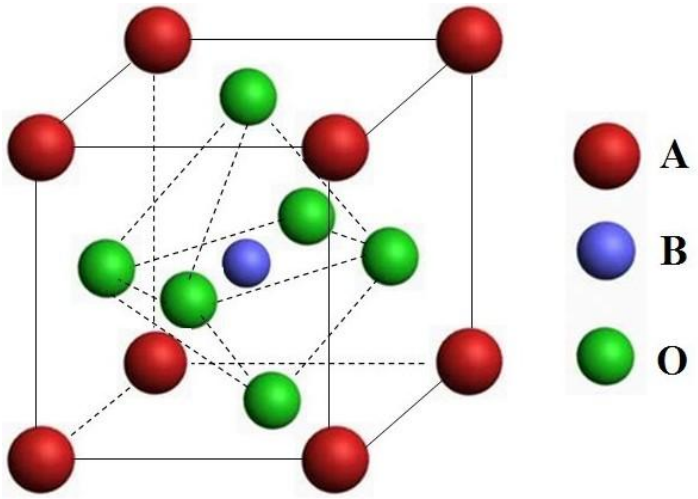


Figure 2.2 Perovskite cell of PLZT.

The perovskite structure can also be visualized as a corner-linked $BO_6$ oxygen octahedron. For PLZT crystal, $Zr^{4+}$ and $Ti^{4+}$ locate at the center (B-site) of the octahedron while $La^{3+}$ and $Pb^{2+}$ fill up the dodecahedral hole (A-site) between the oxygen octahedral. The stability and distortion of a perovskite structure formed by various cations can be empirically predicted by the Goldschmidt tolerance factor:

$$t = \frac{(R_A + R_O)}{\sqrt{2}(R_B + R_O)} \tag{2.32}$$

where $t$ is called Goldschmidt tolerance factor, $R_A$, $R_B$ and $R_O$ are the ionic radii of the A cation, B cation and oxygen, respectively (Senyshyn, 2005). For a perfectly

fit perovskite structure, the tolerance factor is 1.0. As $0.95 < t < 1.0$, the structure is cubic. The structure tends to be slightly distorted but non-ferroelectric when $t <$ 0.95, and those with $t$ slightly greater than 1.0 are ferroelectric (Wood, 1951, Keith, 1954).

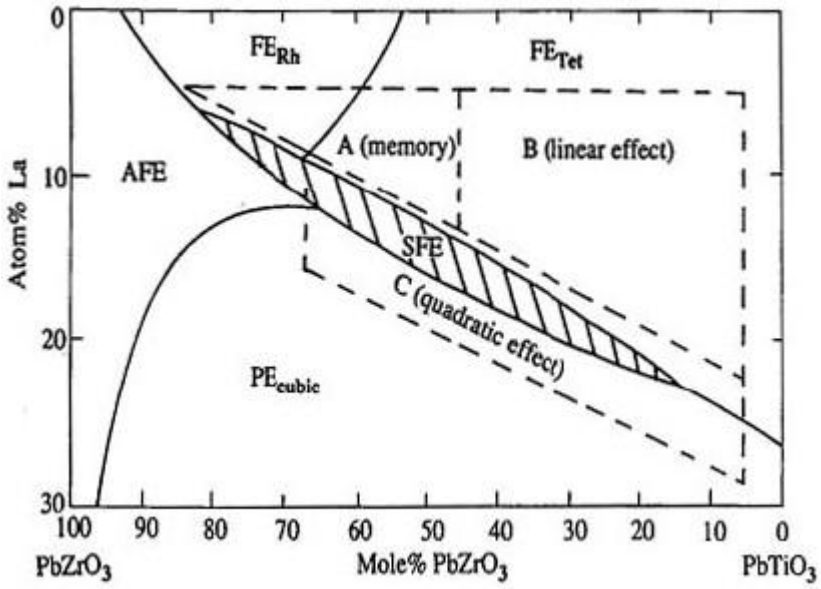


Figure 2.3 Phase diagram of PLZT at room temperature (Hartling, 1987).
AFE: antiferroelectric; $FE_{Rh}$: ferroelectric rhombohedral;
$PE_{cubic}$: paraelectric cubic; $FE_{Tet}$: ferroelectric tetragonal

The phase diagram of PLZT at room temperature is shown in Fig. 2.3. Depending on the composition, PLZT ceramics present three types of EO responses: memory, linear and quadratic. The memory materials are largely located in the ferroelectric rhombohedral phase region with stable and electrically switchable optical states. The linear compositions possess the area encompassing the tetragonal phase with nonswitching and linear EO effect. The quadratic compositions are located along the phase boundary separating the ferroelectric and paraelectric phases with quadratic EO effect. A large range of compositions have been

investigated. Table 2.2 shows the EO coefficients for PLZT ceramics with different compositions (Moulson, 2003, Bailey, 2004).

Table 2.2 EO coefficients of PLZT with different compositions (Moulson, 2003, Bailey, 2004).

| Composition La/Zr/Ti | $R_c$ ($10^{-16}m^2/V^2$) | $r_c$($10^{-12}$m/V) |
|---|---|---|
| 8.5/65/35 | 38.60 | --- |
| 9/65/35 | 3.80 | --- |
| 9.5/65/35 | 1.50 | --- |
| 10/65/35 | 0.80 | --- |
| 11/65/35 | 0.32 | --- |
| 12/65/35 | 0.16 | --- |
| 8/70/30 | 11.7 | --- |
| 8/40/60 | --- | 1.0 |
| 8/65/35 | --- | 5.2 |

### 2.3.2 PMN-PT Ceramics

PLZT ceramic is the widely used EO ceramic. However, there are some disadvantages of it, such as sensitive to temperature variation, significant field induced and polarization dependent scattering losses. $Pb(Mg_{1/3}Nb_{2/3})O_3$-$PbTiO_3$ (PMN-PT) is another important lead-based EO ceramic (Zou, 2004). It is a relaxor ferroelectric with minimal hysteresis, which resolves the issue of high hysteresis experienced by the PLZT EO ceramics. PMN-PT ceramic is suitable for almost all the visible to mid-IR optical applications because of the remarkably good transparency over a wide range of 500 nm-7000 nm. Moreover, the EO coefficient of PMN-PT is about 2 to 5 times larger than that of PLZT, which significantly lowers the applied voltage for achieving the same phase shift (Jiang, 2005). Similar

to PLZT, PMN-PT also possesses the perovskite structure, in which the A-site is occupied by $Pb^{2+}$ and B-site is filled by $Mg^{2+}$, $Nb^{5+}$ and $Ti^{4+}$ cations.

As shown in Fig. 2.4, the phase diagram of PMN-PT can be mainly divided into two parts at room temperature: rhombohedral, relaxor side specific for materials with small PT amount, and tetragonal, ferroelectric with high PT content. Ran *et al*. have reported the quadratic EO coefficient of transparent PMN-PT ceramics: $R_{11}=5.1683\times10^{-14}$ $m^2/V^2$ and $R_{12}=6.106\times10^{-14}$ $m^2/V^2$ (Ran, 2011).

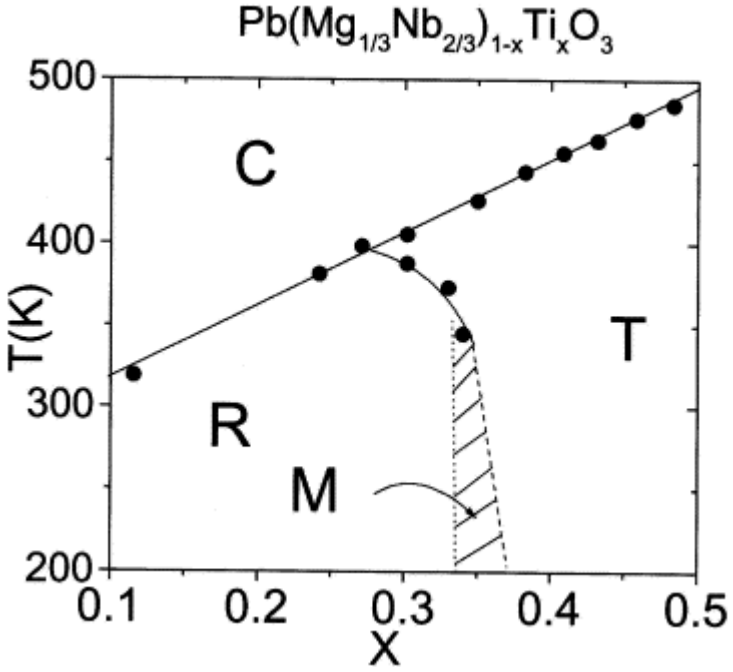


Figure 2.4 Phase diagram of the PMN-PT solid solution system (Shrout, 1990)
C: cubic; T: tetragonal; R:rhombohedral; M:monoclinic.

## 2.4 Current Lead-Free EO Ceramics

Most of the lead-free ceramics are opaque and hence there are few works reporting the EO properties of them. Recently, Jan Kroupa *et al*, have found that the $(1-x)K_{0.5}Na_{0.5}NbO_3$-$xSrTiO_3$ with $0.15<x<0.25$ (KNN-STO) ceramics exhibit good

optical properties (Bobnar, 2004, Kroupa, 2005, Kosec, 2004). The ceramics possess a pseudo-cubic perovskite structure, a high density and uniform distribution of fine grains and pores (Fig. 2.5).

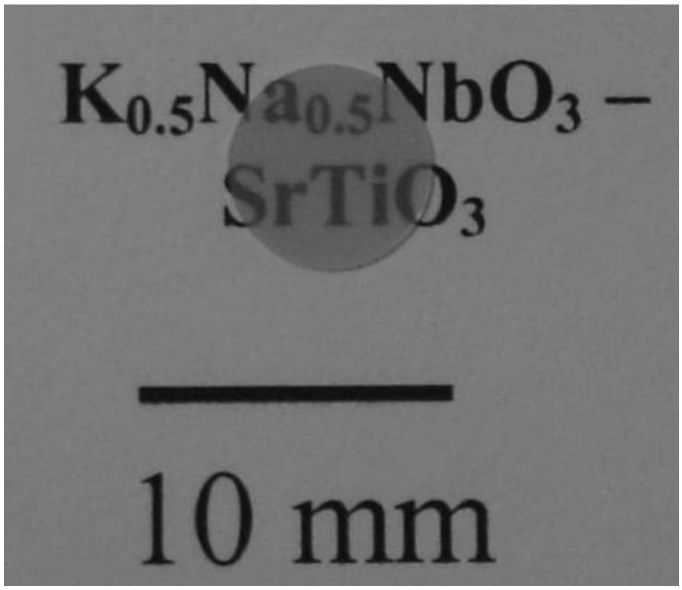


Figure 2.5 Representative sample of transluent (1-x)KNN-xSTO (x=0.2) ceramics with the thickness of 0.25 mm (Kosec, 2004).

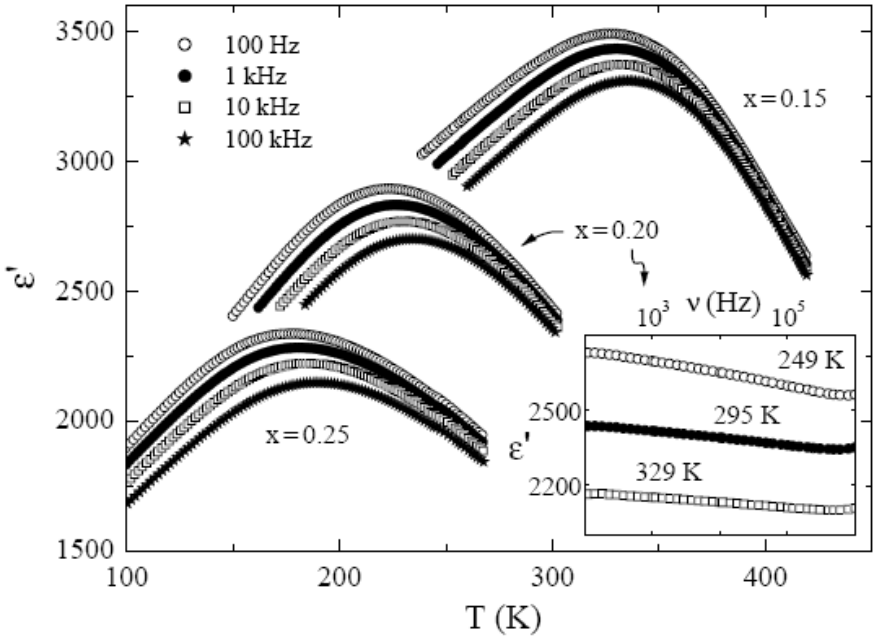


Figure 2.6 Temperature dependence of the $\varepsilon'$, measured at several frequencies

in KNN-STO samples of different compositions (Bobnar, 2004).

They also show the relaxor-like dielectric characteristics, such as a broad dispersive dielectric maximum, Vogel-Fulcher temperature dependence of the characteristic relaxation frequency, and paraelectric-to-glass crossover in the temperature dependence of the dielectric nonlinearlity (Fig. 2.6).

Moreover, the authors have also showed that the KNN-STO-0.2 ceramic is a typical quadratic EO material, exhibiting a considerably large quadratic EO coefficient ($n^3R_{33}$~$1.9\times10^{-16}$ $m^2/V^2$), which is suggested to be connected with its relaxor properties (Kroupa, 2005). The linear EO coefficient induced under a high electric field of 10 kV/cm of the ceramic has also been measured ($n^3r_{33}$~$190\times10^{-12}$ m/V). Both the field-induced linear EO coefficient and quadratic EO coefficient exhibit similar frequency dependence as shown in Fig. 2.7.

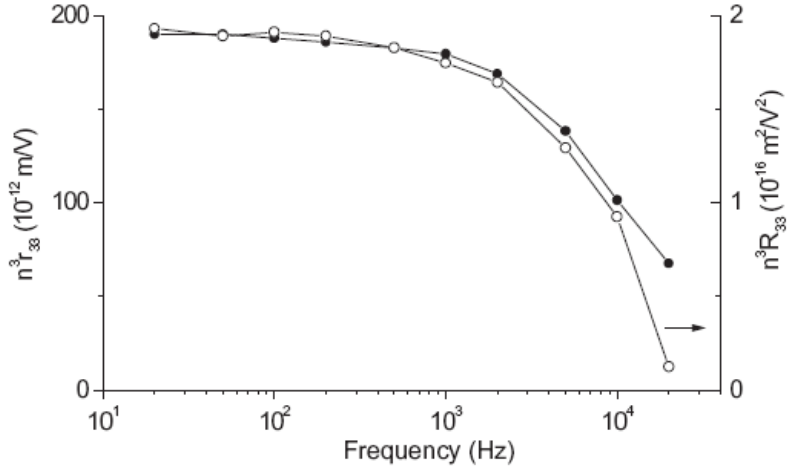


Figure 2.7 Dispersion of the field induced linear EO coefficient $r_{33}$ and the quadratic $R_{33}$ coefficient in KNN–STO ceramics (Kroupa, 2005).

## 2.5 Factors Affecting Transparency of Ceramics

The ceramics used as EO materials must exhibit good optical transparency. It has been shown that the scattering of light at the surfaces, grains, grain boundaries, pores, and second-phase inclusions are the main factors affecting the transmittance of ceramics (Moulson, 2003, Krell, 2006, Grimm, 1971), as shown in Fig. 2.8.

Diffuse scattering of light at rough surfaces reduces the intensity of incident light and therefore lowers the transparency of ceramic. This can be avoided by properly preparing or polishing the surfaces as the diffuse scattering of light at smooth surfaces can be neglected (Apetz, 2003). Effects of surface roughness on the optical properties should be considered (Retherford, 2001). Furthermore, the reflection loss at the air-ceramic interfaces, caused by the difference between the refractive indexes of air and ceramics, will reduce the transmittance of incident light (Apetz, 2003). The reflection loss at the surfaces of the ceramic can be calculated by $R=(n-1)^2/(n+1)^2$, where $R$ is the reflectance and $n$ is the refractive index of ceramic. Application of antireflection coating at the air-ceramic interfaces can eliminate the reflection loss.

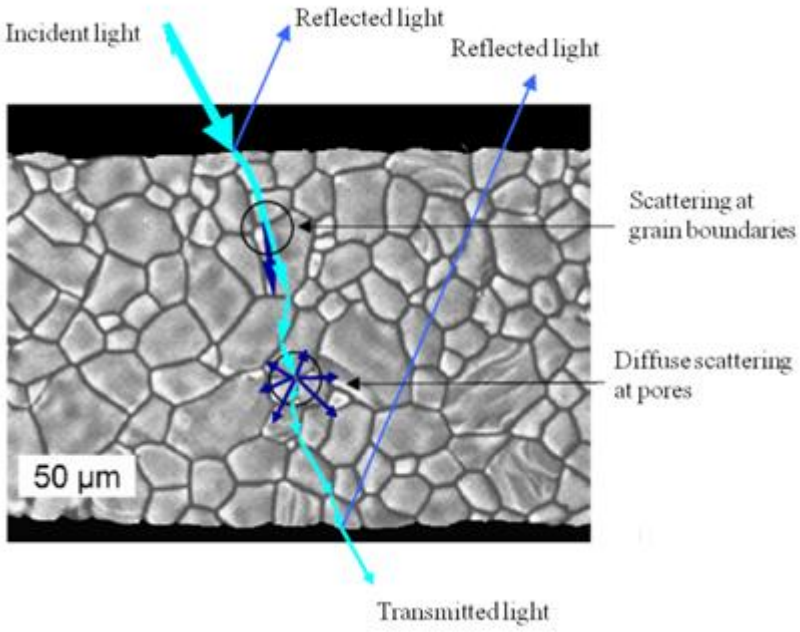


Figure 2.8 Light transmission through polycrystalline (Krell, 2006).

As shown in Fig. 2.8, diffuse scattering can also take place at the sites of second phases (such as pores or impurities) with different refractive indexes. Therefore, high density and purity are required for good transparent property. The studies of transparent Nd-doped YAG ceramics have showed that the optical transparency is improved significantly when the porosity is lower than 0.01% (Zhang, 2012). According to the Mie scattering theory, the incident light will be scattered significantly by grains of size close to the wavelength of light. Therefore, the grain size is an important factor for obtaining transparent ceramics. The influences of porosity and grain size for $Al_2O_3$ have been evaluated (Apetz, 2003) and are represented in Fig. 2.9. The influence of porosity (Fig. 2.9a) is calculated for a homogeneous material, while the effect of grain size is studied based on a ceramic with zero porosity (Fig. 2.9b).

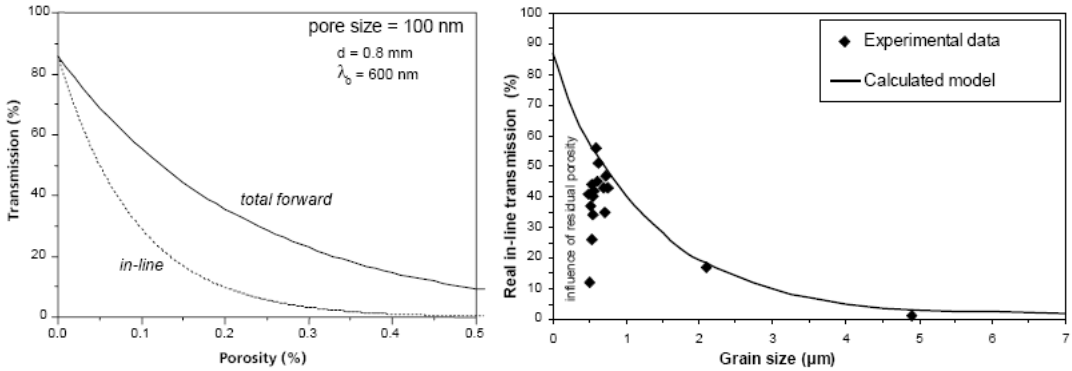


(a) (b)

Figure 2.9 Influences of porosity (a) and grain size (b) on the light transmission through $Al_2O_3$ (Krell, 2006).

## 2.6 Sodium Potassium Niobate-based Ceramics

Because of the strong EO response and good mechanical properties, PLZT ceramics have been widely used in different fields (Moulson, 2003). However, the well-known environmental hazard of lead has aroused attention on lead-free materials. Ferroelectric sodium potassium niobate, $K_{0.5}Na_{0.5}NbO_3$ (KNN), has been considered as a promising candidate to replace lead-based ceramics for their high Curie temperature and good piezoelectric properties (Saito, 2004, Egerton, 1959). Owing to the high electromechanical coupling factor and low dielectric constant, it is particularly suitable for ultrasonic device applications (Egerton, 1959).

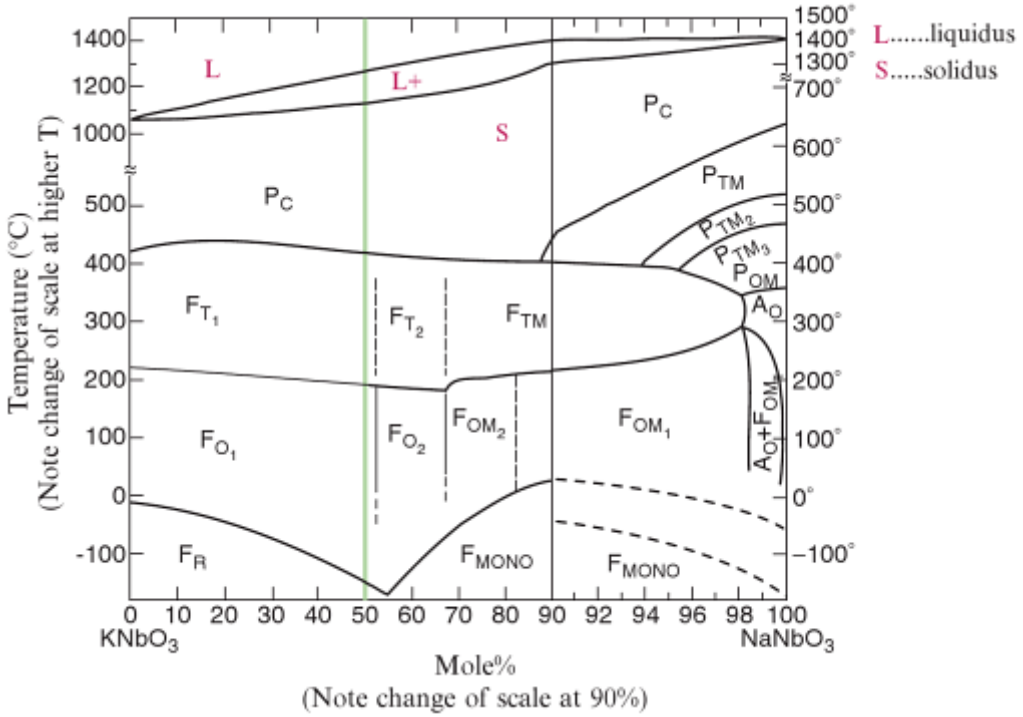


Figure 2.10 Binary phase diagram $KNbO_3$-$NaNbO_3$ (Kosec, 2008).
P: paraelectric; F: ferroelectric; A: antiferroelectric; C: cubic; T: tetragonal
O: orthorhombic; R: rhombohedral; MON: monoclinic; M: multiple cell.

$K_xNa_{1-x}NbO_3$ is a ferroelectric system with a perovskite structure. The A-site is shared by $K^+$ and $Na^+$ while the B-site is occupied by $Nb^{4+}$. It is a mixed system of orthorhombic ferroelectric potassium niobate ($KNbO_3$) and orthorhombic sodium niobate ($NaNbO_3$). As shown in Fig. 2.10, $K_xNa_{1-x}NbO_3$ exhibits a complicated phase diagram with several structural phase transitions. $K_xNa_{1-x}NbO_3$ was first reported as a ferroelectric by Shirane *et al*. (Shirane, 1954), but its good piezoelectric properties were given by Egerton *et al*. a few year later (Egerton, 1959). KNN shows the highest electromechanical coupling coefficient and moderate dielectric susceptibility (Shirane, 1954, Haertling, 1967), and its remnant

polarization reaches a maximum and decreases towards the both end members, whereas the coercive field has its minimum (Haertling, 1967).

However, there are a few drawbacks hindering the wide industrial use of KNN. Owing to the high volatility of alkali metal compounds, stringent manufacturing conditions and low reaction temperatures are generally required. The phase stability of pure KNN ceramics is limited to 1140$^{o}$C according to the phase diagram (Egerton, 1959). Therefore, high temperature sintering is also not desirable. Moreover, the pores cannot be easily eliminated with the grain growth because of the quadrate morphology of the grain for pure KNN (Maeder, 2004). Consequently, KNN generally exhibits poor densification behavior under the conventional pressureless sintering conditions.

Various methods have been developed to improve the sinterability of KNN ceramics. One way is to form new solid solutions with other ferroelectrics, such as KNN-$LiNbO_3$ (Guo, 2004) and KNN-$SrTiO_3$ (Kroupa, 2005). Generally, the relative density of KNN ceramics fabricated by conventional sintering is about 90-95%. It has been shown that the relative density of KNN-$SrTiO_3$ ceramics fabricated by pressureless sintering can achieve above 99% (Kosec, 2004). For KNN-$LiNbO_3$ ceramics, the relative density is about 97% and their piezoelectric and electromechanical responses are enhanced, giving $d_{33}$=200-235 pC/N, $k_p$=0.38-0.44, and $k_t$=0.44-0.48. It has also been shown that the content of $LiNbO_3$ should remain below 8%, otherwise secondary phases begin to appear in the KNN-$LiNbO_3$ system.

Various sintering aids, such as CuO and $MnO_2$, have also been exploited to improve the sinterability of KNN ceramics. Copper has been found as an effective

sintering aid, which can increase the relative density to about 97.5% and decrease the sintering temperature down to 950$^{o}$C (Matsubara, 2004, Chen, 2007, Park, 2008, Park, 2007). It improves the sinterability by creating a liquid phase during sintering. The optimum content of the sintering aid is about 0.5%. On the other hand, the doping of $Bi_2O_3$ can also increase the relative density of KNN to above 99% (Fig. 2.11) and hence improve the piezoelectric properties (Du, 2007). For the $(K_{0.5}Na_{0.5})_{0.97}Bi_{0.01}NbO_3$ ceramics, $d_{33}$=164 pC/N, $k_p$=0.47, and $Q_m$=120.

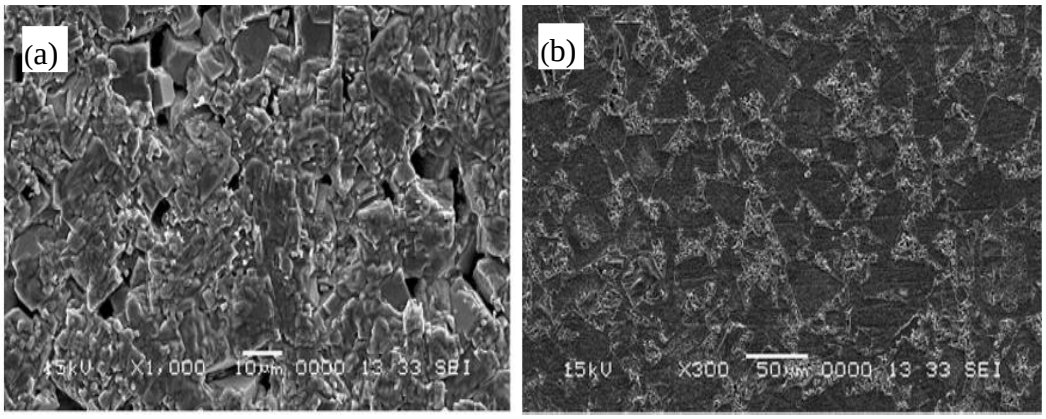


Figure 2.11 SEM micrographs obtained for the thermally etched surface of (a) KNN and (b) $(K_{0.5}Na_{0.5})_{0.97}Bi_{0.01}NbO_3$ ceramics (Du, 2007).

Li and Bi co-modified KNN ceramics, $[(K_{(1-x)/2}Na_{(1-x)/2}Li_x)_{1-3y}Bi_y]NbO_3$, have been studied by Du *et al* (Du, 2007). In their work, both $Li^+$ and $Bi^{3+}$ enter the A-site for replacing $K^+$ and $Na^+$. The grain growth is inhibited by the doping of Bi and the microstructure of the ceramics becomes uniform and fine (Figure 2.12). For the ceramic with x=0.06 and y=0.005, the piezoelectric properties become optimum, giving $d_{33}$=185 pC/N, $k_p$=0.43 and $k_t$=0.45.

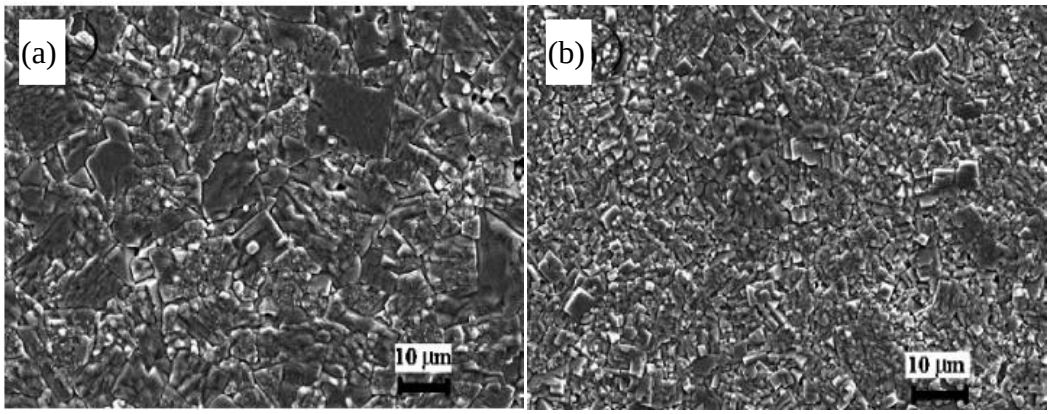


Figure 2.12 SEM micrographs obtained for the thermally etched surface of KNLBN ceramics. (a) x=0.06, y=0.0 and (b) x=0.06, y=0.005 (Du, 2007).

Another way to improve the densification of KNN ceramics is using special sintering method, such as hot-pressing (Ringgaard, 2005), hot isostatic pressing (HIP) (Jaeger, 1962), cold isostatic pressing (CIP) (Guo, 2004), spark plasma sintering (Wang, 2004, Wang, 2002), and hot forging (Wang, 2004). Hot-press sintering is used to overcome the poor densification of usually less than 96% theoretical density of KNN (Birol, 2006, Du, 2006). Hot isostatic pressing of KNN yields the relative density of above 99% and a finer grained microstructure compared to conventional sintering (Egerton, 1959, Jaeger, 1962). Spark plasma sintering is highly effective in enhancing sinterability of materials, inducing better densification with minimized grain growth. It's reported that more than 99% relative density and grain sizes between 200 nm and 500 nm can be obtained (Li, 2006).

## 2.7 Hot-Press Sintering Technique

Hot-press sintering technique is a process that produces dense ceramics through the application of heat and pressure simultaneously (Basu, 2011). Hot-press

sintering is widely used to consolidate metal and ceramic powders to fully density with controlled microstructure. In the process, pressure and heat are applied to a green sample simultaneously, as shown in Fig. 2.13 (Fang, 2005, Viswanathan, 2006). The green sample is embedded in a mold filled fully with powders in order to obtain uniform pressure across the sample and prevent high-temperature reactions with surrounding materials. Uniaxial pressure can be applied statically or dynamically. Heat can be provided directly (induction or wire resistance) or indirectly (convection or radiation). The main advantage of this technique in comparison to the pressureless sintering is the reduction in the process time due to the application of the pressure (Viswanathan, 2006)

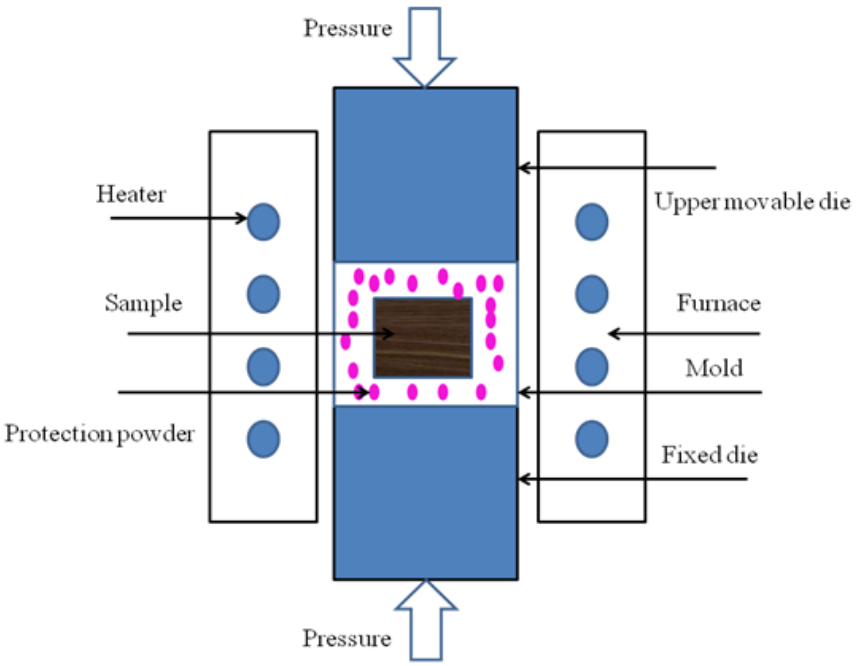


Figure 2.13 Schematic diagram of hot pressing furnace used for bulk materials.

The hot-press sintering method was first reported by Hartling (Hartling, 1971) for fabricating PLZT transparent ceramics (Stojanovic, 2001, Santos, 2001,

Stojanovic, 2000). As the hot-press sintering can improve the density of samples effectively, it has been used in various material fabrication, such as nano-SiC ceramics (Ma, 1998), $Si_3N_4$-based ceramics (Kido, 2005), and dental glass-ceramics (Gonzaga, 2008). Table 2.3 compares the properties of KNN ceramics sintered by hot-press and pressureless sintering (Egerton, 1959, Jaeger, 1962).

Table 2.3 Some physical properties of air-fired and hot-pressed ceramic.

| Physical Quantity | KNN (Pressureless) | KNN (Hot-press) |
|---|---|---|
| $\varepsilon_r$ | 290 (100 kHz) | 420 (100 kHz) |
| $Y$ (GPa) | 104 | 104 |
| $\rho$ (g/cm$^3$) | 4.25 | 4.46 |
| $d_{31}$ (pC/N) | -32 | -49 |
| $d_{33}$ (pC/N) | 80 | 160 |
| $g_{31}$ (mVm/N) | 12.6 | 13.1 |
| $g_{33}$ (mVm/N) | 31.5 | 43 |
| $k_p$ | 0.36 | 0.45 |
| $k_{31}$ | 0.22 | 0.27 |
| $k_{33}$ | 0.51 | 0.53 |
| $P_s$ | 22 | --- |
| $P_r$ | 18 | --- |

# Chapter 3 Fabrication and Characterization of KNNLB Ceramics

## 3.1 Fabrication of KNNLB Ceramics

The ceramics for this study were prepared by the conventional solid-state reaction. Two sintering methods, hot-press and pressureless sintering, were used to densify the ceramics. Three groups of samples have been fabricated; they are:

(a) $(K_{0.5}Na_{0.5})_{0.95}Li_{0.05}Nb_{0.95}Bi_{0.05}O_3$ + y mol% excess $Bi_2O_3$, with y = 0, 1, 2, 3, 4. The samples are abbreviated as KNNLB-5-y.

(b) $(K_{0.5}Na_{0.5})_{1-x}Li_xNb_{1-x}Bi_xO_3$ with x varying from 0 to 0.09. The samples are abbreviated as KNNLB-100x.

(c) $(K_{0.5}Na_{0.5})_{0.9}Li_{0.1}Nb_{0.9}Bi_{0.1}O_3$ + z mol% excess $Bi_2O_3$ with z = 0, 2, 4, 6, 8. The samples are abbreviated as KNNLB-10-z.

Generally, six main stages are included in the fabrication of the KNNLB ceramics; namely: selection of raw materials, preparation of precursor powders, calcination, shaping, binder burnout and sintering. In order to avoid contamination by impurities that could affect the properties of the ceramics, all the equipments and apparatuses were cleaned using pure ethanol and acetone before the experiments.

### 3.1.1 Raw Materials

The label on a chemical container shows only the approximate composition of its contents and the maximum levels of certain impurities. Moreover, the moisture content is difficult to be specified accurately as it depends on the ambient humidity, the method of storage and the particle size. For non-hygroscopic materials the moisture content varies from less than 0.1% to more than 1%, which is much less than the hygroscopic materials (Moulson, 2003). Chemical composition, particle size and degree of aggregation are the important aspects of a raw material, which should be considered in selecting the raw materials. In this study, reagent grade metal oxides or oxalate powders: $K_2C_2O_4$ (99.5%), $Na_2C_2O_4$ (99.5%), $Nb_2O_5$ (99.99%), $CH_3COOLi\ H_2O$ (99.5%) and $Bi_2O_3$ (99.99%) were used for fabricating the ceramics.

### 3.1.2 Powder Preparation

As inhomogeneity can be detected optically much more easily than electrically, precursor powders with higher purity, better homogeneity and high-reactivity are essentially required for fabricating transparent EO ceramics. Accordingly, a solution coating approach, which entailed coating the sodium-potassium-lithium (Na-K-Li) precursor solution on the niobium and bismuth oxide powders, was applied in this study to prepare the precursor powders (Li, 2009). Stoichiometric amounts of $K_2C_2O_4$, $Na_2C_2O_4$ and $CH_3COOLi\ H_2O$ were first dissolved in deionized water. $Nb_2O_5$ and $Bi_2O_3$ powders were then added and mixed thoroughly

to obtain a homogeneous suspension, which was then dried and grinded to obtain the precursor powders for the calcination.

### 3.1.3 Calcination

Although the precursor powders can be immediately pressed into a shape and sintered at high temperatures, an intermediate heating process at a relatively low temperature called calcination is preferred. The purpose of the calcination process is to cause the constituents to interact by inter-diffusion of their ions for forming a chemically and crystallographically uniform structure. Although the required final phase may not be completely formed after the calcination, the remaining chemical gradients may promote the formation of homogeneous body during sintering. The calcination conditions are hence important parameters which can affect the densification of the ceramics during sintering. In general, the calcined material is a porous and fragile solid because of the limited amount of sintering. So a grinding process is required to produce fine powders for shaping. In this study, the calcination was carried out at 850°C for 5 h, and the calcined powders were ball-milled in alcohol using zirconia balls for 24 h and then dried.

### 3.1.4 Shaping

Various processes have been developed to shape the calcined powders into different final forms (Table 3.1) (Moulson, 2003). In general, an organic binder is required to give the dry forms a sufficient strength to avoid breakage during the handlings before sintering. Obviously, the binder must be able to be eliminated

completely after sintering. Otherwise the residue will produce disruptive effect on the sintered ceramics. In this study, a polyvinyl alcohol (PVA) solution was used as the binder for shaping and strengthening the dry forms. The concentration of the PVA solution is about 5 wt% in water. The solution was mixed thoroughly with the calcined powder in a weight ratio of 0.3:1. The mixture was then pressed into green disk samples with a diameter of 15 mm. A uniaxial pressure of ~400 MPa was used so as to remove the air inside and to obtain a well-packed disk sample. For the hot-press sintering, the thickness of the green samples was ~2.6 mm, while samples of thickness ~1.3 mm were prepared for the pressureless sintering.

Table 3.1 Feed materials for various shaping methods and the type of product.

| Shaping method | Type of feed material | Type of shape |
|---|---|---|
| Dry-pressing | Free-flowing granules | Small simple shapes |
| Isostatic pressing | Fragile granules | Larger more intricate shapes |
| Calendering; viscous plastic processing | Plastic mass based on an elastic polymer | Thin plated<br>Simple shapes |
| Extrusion | Plastic mass using a viscous polymer solution | Elongated shapes of constant cross-section |
| Jiggering | Stiff mud containing clay | Large simple shaped |
| Injection moulding | Organic binder giving fluidity when hot | Complex shapes |
| Slip-casting | Free-flowing cream | Mainly hollow shapes |
| Ban-casting | Free-flowing cream | Thin plates and sheets |
| Screen-printing | Printing ink consistency | Thin layers on substrates |

### 3.1.5 Binder Burnout

The organic binder provides plasticity for shaping and green compact strength for handling (Reed, 1988, Richerson, 1992). Removal of the organic binder from the green samples after pressing and before sintering is a critical step. Thermal decomposition is generally used to remove the organic binder (Clark, 1988). Upon heating, the organic binder will decompose, generating various kinds of gasses and producing a gas pressure in the green samples. If the pressure increases too fast, cracks or voids will be generated and the green samples will break. Accordingly, the heating rate, temperature and duration time are the key processing parameters, which have to be optimized to burnout the organic binder completely as quickly as possible without damaging or breaking the green samples (Ewsuk, 1995).

In this study, the PVA organic binder was burned out at 850°C for 2 h. The green disk samples were placed on an alumina plate and embedded with sintered ceramic powders of the same composition. The samples were then heated in a muffle furnace under an oxygen-rich environment so that carbon dioxide instead of carbon monoxide was produced. For burning out the binder effectively, the temperature was first increased at a rate of 3°C/min to 600°C. Then the temperature was increased at a slower rate of 1°C/min and kept at 850°C for 2 h to completely burn out the binder. For hot-press sintering, the samples were then cooled down to room temperature. For pressureless sintering, the samples were heated immediately to higher temperatures for the sintering process.

### 3.1.6 Sintering

After the binder burnout process, the samples were heated at high temperatures for densification. The process is completed either by solid state or liquid phase sintering, and the driving force for it is the decrease in surface energy resulted from the disappearance of the solid-vapour surface. For solid state sintering, the process takes place at the temperature of about 0.8 to 0.9 $T_m$ ($T_m$ is the melting temperature in *K*). First, owing to the sufficient mobility, the constituent ions diffuse from convex surfaces (where their energy is high) to the concavities at particle contact points (where their energy is lower), and thus leading to changes in microstructure. At this stage, no noticeable densification is resulted. Mass transport from grains to pores then occurs to achieve the densification. This is a process arisen from the diffusion of vacancies from regions close to the pore surface (having a higher vacancy concentration as compared to the equilibrium concentration in the bulk) to the grain boundaries. In liquid phase sintering, a small amount of liquid is formed at the sintering temperature, which can facilitate the movement of ions via dissolving them at high energy sites and precipitating at low energy sites. For both solid state and liquid phase sintering, due to the reduction in overall grain boundary energy, densification is normally accompanied by significant grain growth. A number of factors, such as the particle size, heating schedule and chemical composition, can affect the grain size, which may affect the mechanical and electrical properties of the ceramics to a great extent.

In this study, two solid state sintering methods, hot-press and pressureless sintering, were used to fabricate the KNNLB ceramics. Fig. 3.1 shows the experimental setup for the hot-press sintering. The hot-press sintering method was first reported by Hartling (Hartling, 1971) for fabricating PLZT transparent ceramics (Stojanovic, 2001, Santos, 2001, Stojanovic, 2000). The method has also been successfully used to sinter other ceramics for improving the sinterability (Ma, 1998). The bending strength, relative density, hardness and fracture toughness of $Si_3N_4$-based ceramics were improved by hot-press sintering (Kido, 2005). Dental glass-ceramics have been fabricated by hot-press sintering successfully (Gonzaga, 2008).

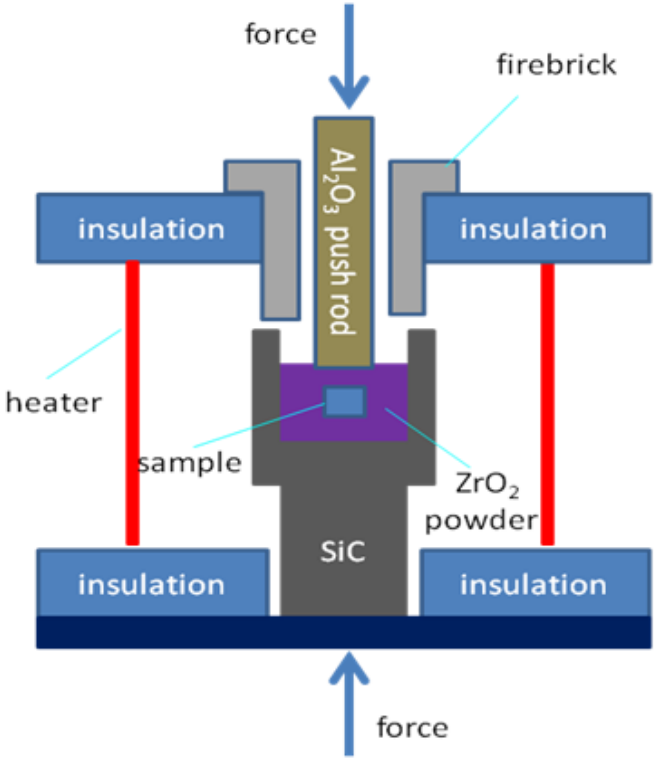


Figure 3.1 Typical hot-pressing setup for fabricating KNNLB electro-optic ceramics.

As shown in Fig. 3.1, the green sample was embedded in a tungsten carbide mold filled fully with zirconium dioxide powders so that a pressure could be applied uniformly across the sample. The high pressure was applied by a hydraulic system to the sample through an $Al_2O_3$ rod. A computerized system was used to control the temperature and pressure. Fig. 3.2 shows the temperature and pressure profiles used for sintering the KNNLB samples.

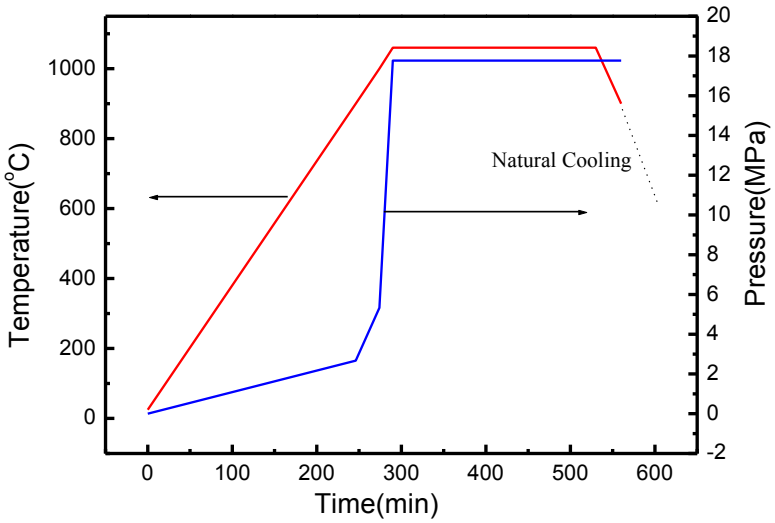


Figure 3.2 Schematic diagram of the hot-press sintering program for the KNNLB ceramics.

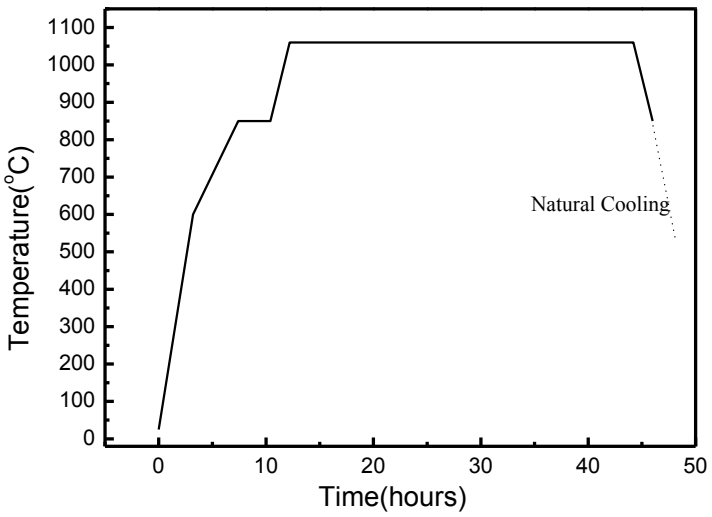


Figure 3.3 Schematic diagram of the pressureless sintering program for the KNNLB ceramics.

For pressureless sintering, the samples were placed on an alumina plate and embedded with sintered ceramic powders of the same composition and heated in a muffle furnace right after the calcination process to high temperatures for densification. The temperature profile for the process is shown in Fig. 3.3.

### 3.1.7 Poling and Short-Circuit Aging

After sintering, the ceramics were polished to different thicknesses for various measurements. For optical measurements, the ceramics were polished with 1-μm diamond paste to obtain smooth and parallel surfaces. The thickness of the ceramics was 0.5 mm. For other measurements, the ceramics were simply polished with fine silicon carbide abrasive papers to obtain parallel surfaces. The thickness of the sample was in the range of 0.5 to 1 mm.

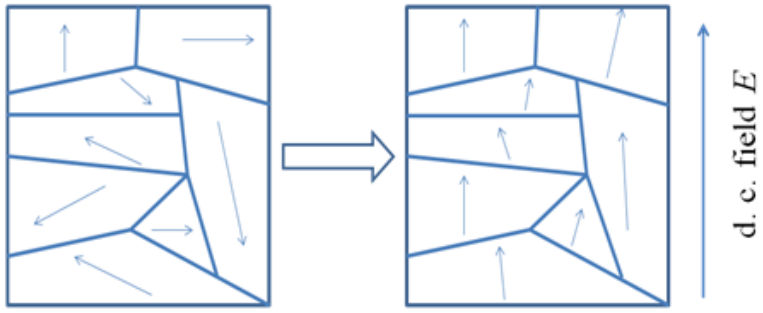


(a) (b)

Figure 3.4 Schematic diagram of polarization.
(a) before poling; (b) after poling.

As shown in Fig. 3.4, the ferroelectric domains in the as-sintered KNNLB ceramics are randomly oriented, so that the material is isotropic. An external

electric field is required to align the domains to the field direction so as to induce the linear electro-optic response. This process is called poling. The poled ceramics are anisotropic, possessing a net permanent polarization. In this work, Au/Cr electrodes were deposited on the top and bottom surfaces of the ceramics by magnetron sputtering for poling and subsequent measurements. The poling circuit is shown in Fig. 3.5. The sample was first heated in an oil bath to a temperature of 150°C. A d.c. electric field of 5.0 kV/mm was then applied for 30 min to fully polarize the sample. After that, the sample was cooled down with the electric field kept on. To remove the charges which may inject into the sample during the poling process, the samples were short-circuited by wrapping in an aluminum foil at room temperature for 24 h.

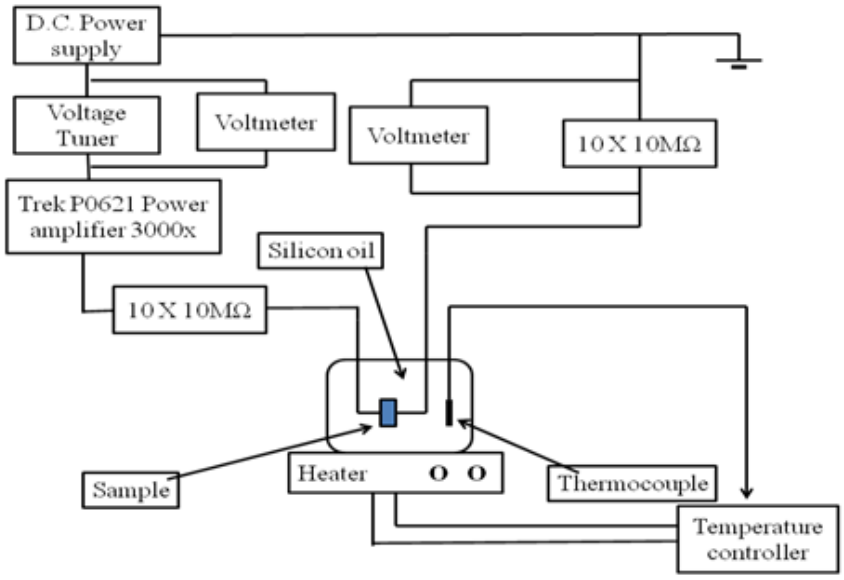


Figure 3.5 Schematic diagram of the d.c. poling circuit for ceramic sample.

## 3.2 Characterization of KNNLB Ceramics

The characterization methods for the structural, electrical, optical and electro-optical properties of the KNNLB ceramics are described in the following sections.

### 3.2.1 Structural Characterization

#### 3.2.1.1 X-ray Diffraction

In this study, the crystalline structure of the KNNLB ceramics was investigated using a Rigaku SmartLab high-resolution diffraction system equipped with CuKα radiation (λ = 0.154 nm). The common $\theta$-$2\theta$ scan was conducted to reveal the crystalline phase and lattice parameters of the ceramics.

X-ray diffraction (XRD) is a versatile, non-destructive method for obtaining information about the crystalline structures such as phases, orientation, lattice parameters and strain of single crystals, ceramics, and thin films. It is also widely used to determine the atomic arrangement and measure the thickness of thin films and multi-layers. The interaction of X-rays with a crystalline material is a complex process, often described as a diffraction phenomenon. It consists of the scattering and interference effects. The scattering of X-ray is related to the interaction between X-rays and crystal lattices of the materials. The X-rays diffracted from different crystal planes interfere with each other, producing a diffraction pattern

upon the change of incident angle of the X-ray beam. The detailed geometry of XRD is shown in Fig. 3.6.

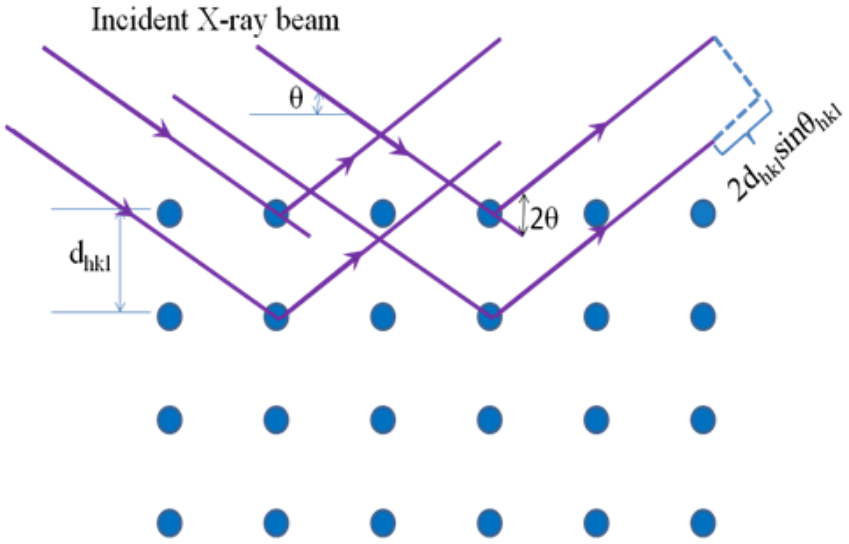


Figure 3.6 Detailed geometry of X-ray reflection.

As shown in Fig. 3.6, when the X-ray beams are diffracted from a given crystal plane, they travel the same distance and then remain in phase with each other. However, there is a path difference $2d_{hkl}\sin\theta_{hkl}$ between the beams diffracted from adjacent crystal planes. $d_{hkl}$ is the interplanar spacing of the {hkl} set of lattice planes with Miller indices h, k, l, and $\theta_{hkl}$ is the incident angle of the beam. According to Bragg's Law, constructive interference between the rays occurs when their path difference is equal to an integral number n of wavelengths:

$$2d_{hkl}\sin\theta_{hkl} = n\lambda \qquad (3.1)$$

where n is called the order of diffraction and λ is the wavelength of the X-ray.

### 3.2.1.2 Scanning Electron Microscope

In this study, a JEOL JSM-6490 scanning electron microscope was used to examine the microstructure of the KNNLB ceramics. The scanning electron microscope (SEM) is a type of electron microscope capable of producing high resolution images of a sample surface. A schematic diagram of a SEM is shown in Fig. 3.7.

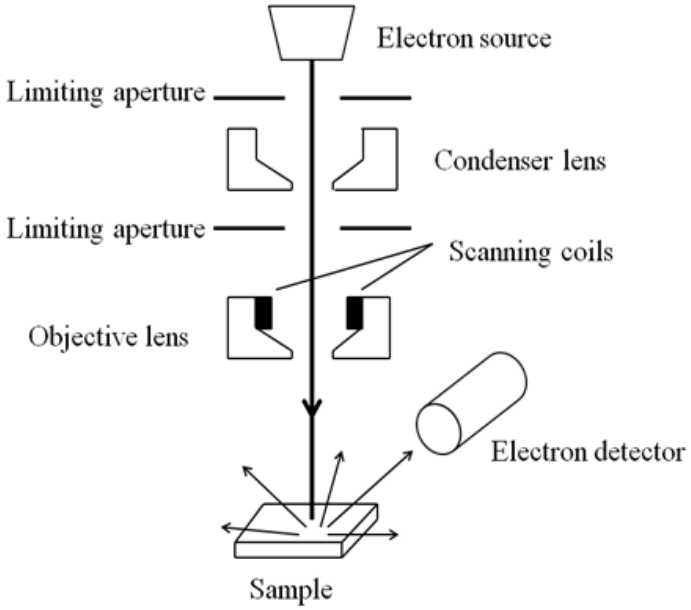


Figure 3.7 Schematic diagram of an SEM set-up.

Owing to the production mechanism, SEM images exhibit three-dimensional characteristics and then are useful for examining the surface structure of a sample. In operation, a narrow beam of accelerated electrons is focused on and scanned across the specimen surface. Three types of radiations will be generated by the interaction of the incident electron beam with the atoms of the specimen (Fig. 3.8):

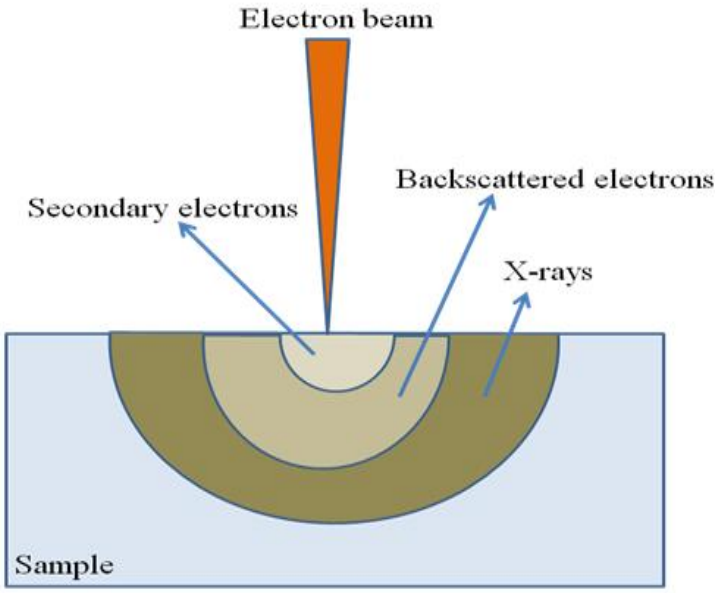


Figure 3.8 Electron beam interaction.

(1) Secondary electrons. These electrons are weekly bound conduction electrons from the outmost shells of the atoms. They usually have low energy and then only those originated within a few nanometers from the sample surface are collected for forming an image. The brightness of the image is determined by the number of electrons collected by the detector, so the images can show morphology and topography of a sample.

(2) Backscattered electrons. These electrons are scattered by the specimen atoms and reflected backward out of the sample. As heavy atoms with a high atomic number can scatter more electrons, images formed by collecting the electrons contain compositional information. Backscattered electron imaging can then be used to locate regions of different atomic numbers, such as metal voiding and high atomic number impurities. It is also useful in examining samples with relatively smooth surface.

(3) Characteristic X-rays. The incident high-energy electron beam may remove the inner shell electrons of the specimen atoms, forming holes in the shell. When these holes are filled by the outer shell electrons, the energy difference of the electron will be released in the form of X-ray of which the energy is characteristic of the specimen atomic number. So these characteristic X-rays can be used to identify the elements in the sample.

### 3.2.2 Ferroelectric Hysteresis Loop Measurement

The polarization *P* is a double-valued function of the applied electric field *E*. A typical *P*-*E* hysteresis loop is shown in Fig. 3.9. A number of material parameters, such as coercive field ($E_c$), remnant polarization ($P_r$), spontaneous polarization ($P_s$), and saturation polarization ($P_{sat}$), can be determined from the *P*-*E* loop. $E_c$ is commonly used to estimate the d.c. electric field required for poling the ceramic samples, which is about two to three times of $E_c$.

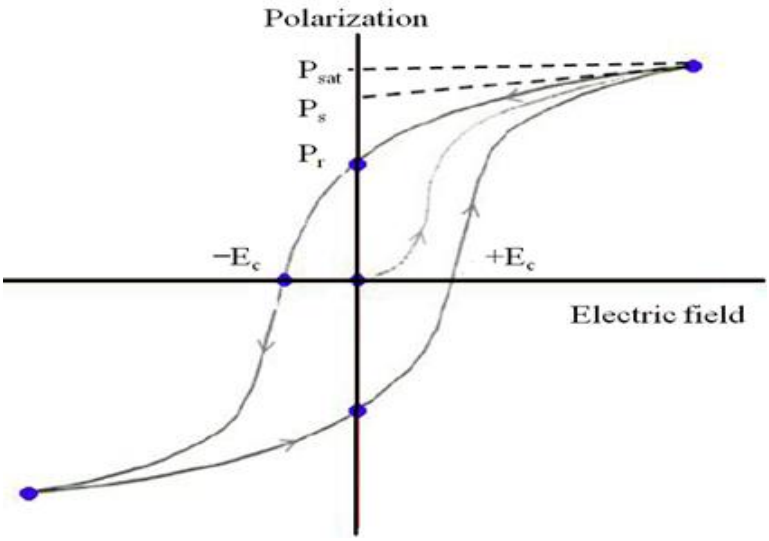


Figure 3.9 A typical *P*-*E* loop for a ferroelectric material.

In this project, a Sawyer-Tower circuit (Sawyer, 1930) is used to measure the ferroelectric hysteresis loop of the KNNLB ceramics. A schematic diagram of the experimental setup is shown in Fig. 3.10. The sample was immersed in a silicone oil bath. A HP 8116A function generator was used to generate an a.c. voltage, which was then amplified by a voltage amplifier (Trek 609D-6) and fed to the sample. A digital oscilloscope (HP 5465A) was used to record the input voltage $V_i$ applied to the sample and the output voltage $V_o$ across the reference capacitor. The polarization of the sample was given as:

$$P = C_{ref}V_o/A \qquad (3.2)$$

where $C_{ref}$ is the capacitance of the reference capacitor and $A$ is the area of electrode on the both surfaces of the sample. A computer program was written to control the whole process.

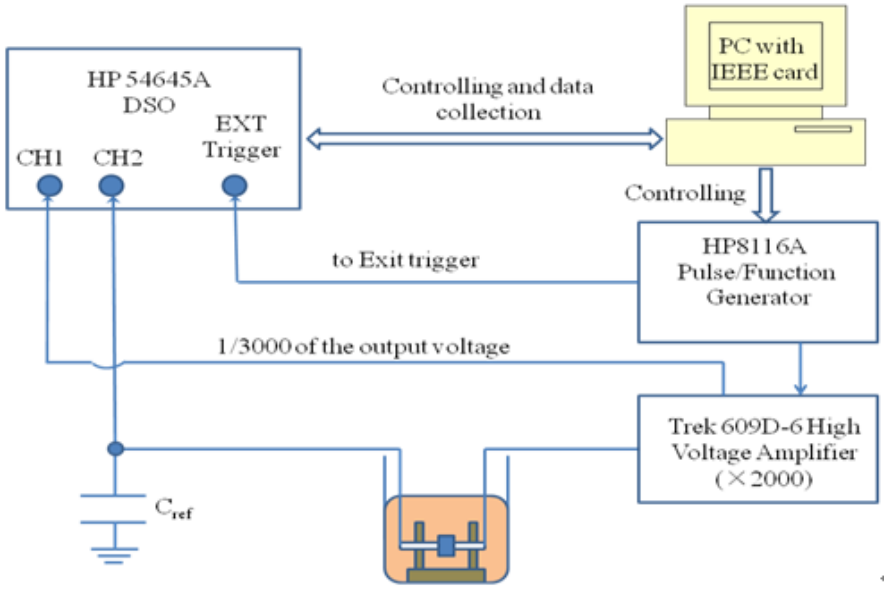


Figure 3.10 Schematic diagram of the hysteresis loop measurement.

### 3.2.3 Density Measurement

The density of a ceramic is an indicator of its quality which is affected by the fabrication conditions, for example, the sintering temperature and pressure. It has been shown that the density will affect the dielectric loss (Zuo, 2008, Singh, 2010), piezoelectric properties (Du, 2007, Guo 2004), and dielectric properties (Singh, 2010) of ceramics. There are a number of ways to measure density. In this work, the measurement based on Archimedes' principle was applied. Following the principle, the mass of the sample in air ($m_{dry}$) and the mass of the sample suspended in water ($m_{water}$) were measured using an electronic balance. With these two parameters and the density of water $\rho_{water}$ (= 1000 kg/m$^3$), the density of the sample $\rho$ was calculated by the following equation:

$$\rho = \frac{m_{dry}}{m_{dry} - m_{water}} \bullet \rho_{water} \qquad (3.3)$$

### 3.2.4 Dielectric Measurement

The dielectric properties of the ceramic samples, including the relative permittivity $\varepsilon_r$ and dielectric loss tanδ, were measured as a function of temperature using a HP 4192A impedance analyzer. The measurement setup is shown in Fig.3.11. The ceramic sample was connected to the impedance analyzer and placed inside a Carbolite furnace. The temperature inside the furnace was measured using a thermocouple connected to a Keithley multimeter. Both the multimeter and impedance analyzer were connected to a computer for controlling and data

collection. The relative permittivity $\varepsilon_r$ of the sample was calculated by:

$$C = \frac{\varepsilon_0 \varepsilon_r A}{L} \tag{3.4}$$

where $C$ is the measured capacitance, $\varepsilon_0$ is the permittivity of free space, $A$ is the electrode area and $L$ is the thickness of the sample.

The relative permittivity $\varepsilon_r$ can be expressed as $\varepsilon_r = \varepsilon' - \varepsilon''$, where $\varepsilon'$ is the real part of the relative permittivity and $\varepsilon''$ is the imaginary part. The dielectric loss tanδ is given by the following equation:

$$\tan\delta = \frac{\varepsilon''}{\varepsilon'} \tag{3.5}$$

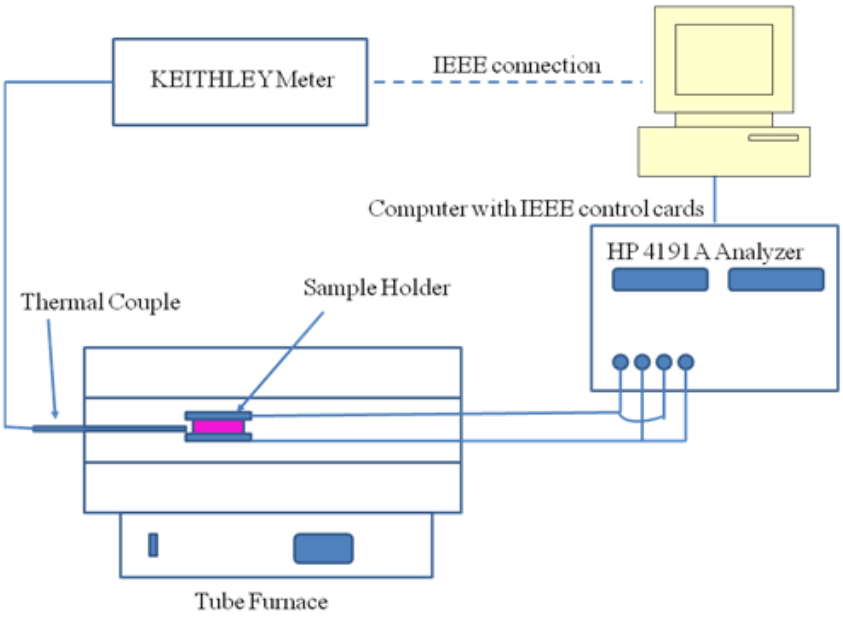


Figure 3.11 Schematic diagram of the dielectric measurement setup.

## 3.2.5 Linear Electro-Optic Coefficient Measurement

Various experimental techniques have been developed to characterize the induced birefringence, electro-optic coefficients and the half-wave voltage of electro-optic materials (Aillerie, 2000). In this study, the modified Sénarmont

method was used to measure the EO coefficients of the KNNLB ceramics. Coplanar electrodes, with a parallel spacing of 1 mm, were adopted for the poling and EO measurement (Fig.3.12). To improve the uniformity of the electric fields, the coplanar electrodes were deposited on both the top and bottom surfaces of the sample.

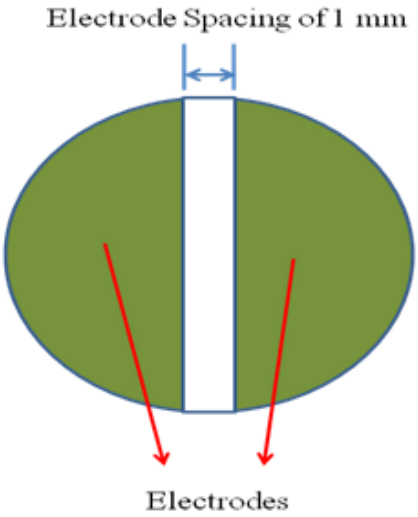


Figure 3.12 Schematic diagram of electrodes for the EO measurement.

A schematic diagram of the experimental setup for the EO measurement is shown in Fig. 3.13. A 2-mW frequency and intensity stabilized He-Ne laser (Model 117A, Spectra-Physics) is used as a light source. The sample is inserted in the light path with its polarization (i.e. the poling direction) aligning along the z-axis. The polarizer and quarter-wave plate are oriented with their optical axes (P and Q) making an angle of $\alpha$ and $\beta$, respectively, with the z-axis. The analyzer will be rotated during the measurement, and its orientation is indexed as $\gamma$, an angle between the optical axes of the analyzer (A) and quarter-wave plate.

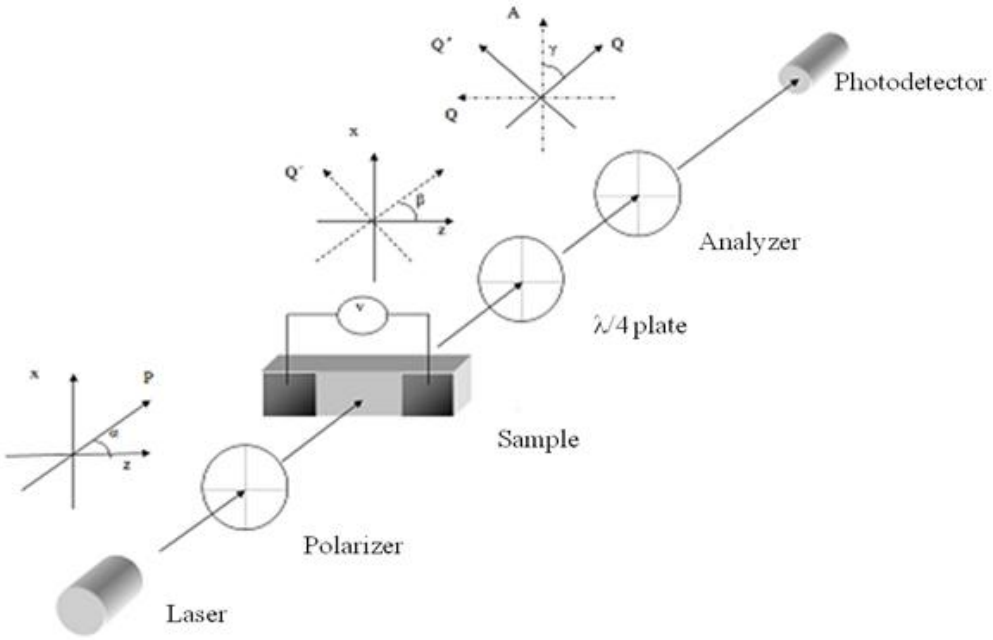


Figure 3.13 The schematic arrangement of the optical and electronic components in the modified S énarmont system.

Let the amplitude of the incident light beam equal $E_{in}$. The two components of the light beam incident normally on the sample are given as:

$$E_x = E_{in} \sin\alpha e^{i(ky+\omega t)} \tag{3.6}$$

$$E_z = E_{in} \cos\alpha e^{i(ky+\omega t)} \tag{3.7}$$

After passing the sample which is subjected to an electric field $E$ along the z-direction, the components become:

$$E_x = E_{in} \sin\alpha e^{ikn_1(E)L} e^{i(ky+\omega t)} \tag{3.8}$$

$$E_z = E_{in} \cos\alpha e^{ikn_3(E)L} e^{i(ky+\omega t)} \tag{3.9}$$

where $L$ is the thickness of the sample (along the y-direction). Define the phase retardation $\Gamma$ as

$$\Gamma=k[n_3(E)-n_1(E)]L \tag{3.10}$$

Eq. 3.9 becomes

$$E_x = E_{in}\cos\alpha e^{ikn_1(E)L}e^{i\Gamma}e^{i(ky-\omega t)} \tag{3.11}$$

After passing through the quarter-wave plate, the light beam, represented in terms of the components along and normal to the optical axis of the quarter-wave plate, Q and Q', respectively, becomes:

$$E_Q = E_{in}[\sin\alpha\sin\beta + \cos\alpha\cos\beta\bullet e^{i\Gamma}]\bullet e^{i(ky-\omega t)+kn_1(E)L} \tag{3.12}$$

$$E_{Q'} = E_{in}[\sin\alpha\cos\beta - \cos\alpha\sin\beta\bullet e^{i\Gamma}]\bullet e^{i\pi/2}e^{i(ky-\omega t)+kn_1(E)L} \tag{3.13}$$

The light beam component which can pass through the analyzer and arrive at the photodetector is given as:

$$\begin{aligned}E_A = E_{in}[&\sin\alpha\sin\beta\cos\gamma + \cos\alpha\cos\beta\cos\gamma\bullet e^{i\Gamma} + \sin\alpha\cos\beta\sin\gamma\bullet e^{i\pi/2}\\ &-\cos\alpha\sin\beta\sin\gamma\bullet e^{i(\Gamma+\pi/2)}]\bullet e^{i(\mathrm{ky}-\omega t)+kn_1(E)L}\end{aligned} \tag{3.14}$$

In practice, α and β are set as 45°. Then Eq. 3.14 becomes

$$E_A = \frac{E_{in}}{2}[\cos\gamma + \cos\gamma\bullet e^{i\Gamma} + \sin\gamma\bullet e^{i(\Gamma+\pi/2)}]\bullet e^{i(ky-\omega t)+kn_1(E)L} \tag{3.15}$$

Using Euler's formula, Eq. 3.15 can be written as

$$E_A = \frac{E_{in}}{2}\{[\cos\gamma + \cos(\Gamma-\gamma)] + i\bullet[\sin\gamma + \sin(\Gamma-\gamma)]\}\bullet e^{i(ky-\omega t)+kn_1(E)L} \tag{3.16}$$

The intensity of the laser beam (which is proportional to $E^2$) is then given as:

$$\begin{aligned}I_A &= \frac{I_{in}}{4}\{2[1+\cos\gamma\cos(\Gamma-\gamma)] + \sin\gamma\sin(\Gamma-\gamma)\}\\ &= \frac{I_{in}}{2}[1+\cos(\Gamma-2\gamma)]\end{aligned} \tag{3.17}$$

The photodetector signal is:

$$V_s = \frac{GI_{in}}{2}[1 + \cos(\Gamma - 2\gamma)] \tag{3.18}$$

where $G$ is a constant depending on the properties of the photodetector.

The fully poled KNNLB ceramics possess uniaxial symmetry, with the optical axis aligned along the poling direction (i.e., z-direction). In the absence of an applied electric field, the equation of the optical indicatrix for the ceramics is given as:

$$\frac{x^2}{n_o^2} + \frac{y^2}{n_o^2} + \frac{z^2}{n_e^2} = 1 \tag{3.19a}$$

The (x, y, z) coordinate is in the principal-axis coordinate system. $n_o$ and $n_e$ are the ordinary and extraordinary refractive index, which equal to the semi-minor and semi-major axis of the indicatrix, respectively (Fig. 2.1). When an electric field $E_o$ is applied to the ceramics along the z-axis (Fig. 3.13), the optical indicatrix will be modified. For the linear EO (Pockels) effect, the changes in refractive indexes are given as:

$$\begin{bmatrix} \Delta\left(\frac{1}{n_1^2}\right) \\ \Delta\left(\frac{1}{n_2^2}\right) \\ \Delta\left(\frac{1}{n_3^2}\right) \\ \Delta\left(\frac{1}{n_4^2}\right) \\ \Delta\left(\frac{1}{n_5^2}\right) \\ \Delta\left(\frac{1}{n_6^2}\right) \end{bmatrix} = \begin{bmatrix} 0 & 0 & r_{13} \\ 0 & 0 & r_{13} \\ 0 & 0 & r_{13} \\ 0 & r_{51} & 0 \\ r_{51} & 0 & 0 \\ 0 & 0 & 0 \end{bmatrix} \begin{bmatrix} 0 \\ 0 \\ E_o \end{bmatrix} \tag{3.19b}$$

The equation of the optical indicatrix now becomes:

$$(\frac{1}{n_o^2} + r_{13}E_o)x^2 + (\frac{1}{n_o^2} + r_{13}E_o)y^2 + (\frac{1}{n_e^2} + r_{33}E_o)z^2 = 1 \qquad (3.20)$$

The new indicatrix has different dimensions, but is not rotated. The new semi-minor and semi-major axis, i.e. $n_o$(E) and $n_e$(E), respectively, are given as:

$$\frac{1}{n_o^2(E)} = \frac{1}{n_o^2} + r_{13}E_o \qquad (3.21a)$$

$$\frac{1}{n_e^2(E)} = \frac{1}{n_e^2} + r_{33}E_o \qquad (3.21c)$$

or

$$n_o(E) = \frac{n_o}{(1 + n_o^2 r_{13}E_o)^{1/2}} = n_o - \frac{1}{2}n_o^3 r_{13}E_o \qquad (3.22a)$$

$$n_e(E) = \frac{n_e}{(1 + n_e^2 r_{33}E_o)^{1/2}} = n_e - \frac{1}{2}n_e^3 r_{33}E_o \qquad (3.22c)$$

Approximations $r_{13}E_o \ll 1/n_o^2$ and $r_{33}E_o \ll 1/n_e^2$ have been used in deriving Eq. 3.22.

As shown in Fig. 3.13, the laser beam travels along the y-axis incident normally on the sample, i.e. normal to the optical axis of the sample. Following the procedures described in Chapter 2, the refractive indexes for the waves travelling in the sample $n_1$ and $n_3$ are determined to be $n_o$(E) and $n_e$(E), respectively. Accordingly, the phase retardation becomes:

$$\Gamma = \frac{2\pi L}{\lambda}(n_3 - n_1) = \frac{2\pi L}{\lambda}[(n_e - n_o) - \frac{1}{2}(n_e^3 r_{33} - n_o^3 r_{13})E_o] \qquad (3.23)$$

Define the effective EO coefficient $r_c$ as

$$r_c = r_{33} - r_{13}(\frac{n_o}{n_e})^3 \qquad (3.24)$$

Eq. 3.23 becomes

$$\Gamma = \frac{2\pi L}{\lambda}[(n_e - n_o) - \frac{1}{2}r_c n_e^3 E_o] \qquad (3.25)$$

To improve the precision, a lock-in detection technique is adopted in the measurement. A small a.c. voltage is applied to the sample, i.e.

$$E_o = \frac{V_o}{d}\sin \omega t \tag{3.26}$$

where $V_o$ is the amplitude of the applied voltage, $\omega$ is the angular frequency and $d$ is the gap between the coplanar electrode. For this case, Eq. 3.25 becomes:

$$\Gamma = \Gamma_o - \Gamma_m \sin \omega t \tag{3.27}$$

where

$$\Gamma_o = \frac{2\pi L}{\lambda}(n_e - n_o) \tag{3.28a}$$

$$\Gamma_m = \frac{\pi L}{\lambda}\frac{r_c n_e^3 V_0}{d} \tag{3.28b}$$

The detected signal is then:

$$\begin{aligned} V_s &= \frac{GI_{in}}{2}[1+\cos(2\gamma - \Gamma_0 + \Gamma_m \sin \omega t)] \\ &= \frac{GI_{in}}{2}[1+2\cos(2\gamma' + \Gamma_m \sin \omega t)] \end{aligned} \tag{3.29}$$

where $2\gamma' = 2\gamma - \Gamma_o$. Using the Jacobi-Anger expansion and Bessel functions, Eq. 3.29 can be approximated as:

$$V_s = \frac{GI_{in}}{2}(1+\cos 2\gamma' - \Gamma_m \sin 2\gamma' \sin \omega t) \tag{3.30}$$

The d.c. component $V_{s,dc}$ and a.c. component $V_{s,ac}$ of the detected signal are:

$$V_{s,dc} = \frac{GI_{in}}{2}(1+\cos 2\gamma') = GI_{in}\cos^2 \gamma' \tag{3.31a}$$

$$V_{s,ac} = \frac{GI_{in}}{2}\Gamma_m \sin 2\gamma' \sin \omega t = V_{s,ac}\sin \omega t \tag{3.31b}$$

In the measurement, the analyzer will be rotated by 360°, in a step of 2°, i.e.; γ as well as γ' will vary from 0 to 360°. By the measurements of the difference between the maximum and minimum values of $V_{s,dc}$:

$$V_{s,dc,p\text{-}p} = V_{s,dc,\max} - V_{s,dc,\min} = GI_{in} \tag{3.32}$$

and the difference between the maximum and minimum amplitude of $V_{s,ac}$:

$$V_{s,ac,p\text{-}p} = V_{s,ac,\max} - V_{s,ac,\min} = GI_{in}\Gamma_m \tag{3.33}$$

the phase retardation Γ is obtained and the effective EO coefficient $r_c$ can be calculated as:

$$r_c = \frac{\lambda d}{\pi L n_e^3 V_o} \frac{V_{s,ac,p\text{-}p}}{V_{s,dc,p\text{-}p}} \tag{3.34}$$

where $\lambda$ is the wavelength of the laser, $d$ is the electrode spacing, $L$ is the thickness of the sample and $V_o$ is the applied voltage.

# Chapter 4 Effects of Sintering Pressure

## 4.1 Introduction

Because of the high volatility of alkali components, pure KNN ceramics are difficult to densify by ordinary sintering method. One way to improve the densification of KNN ceramics is the use of special sintering methods, such as hot-pressing (Ringgaard, 2005), hot isostatic pressing (HIP) (Jaeger, 1962), cold isostatic pressing (CIP) (Guo 2004), spark plasma sintering (Wang, 2004, Wang, 2002), and hot forging (Ahn, 1987). Among the methods, hot-pressing is a mature sintering technique widely used in industries to produce pore-free ceramics. It can consolidate ceramic powders/nanopowders into highly dense microstructures without inducing exaggerated grain growth. The technique has been applied to prepare KNN ceramics in 1962 (Jaeger, 1962), and the influences of hot-pressing temperature have been studied (Gonzaga, 2008, Kim, 2007).

In this work, the hot-press sintering technique is used to fabricate the KNNLB ceramics so as to improve their densification and hence optical quality to crystal-like transparency. In this chapter, the effect of the pressure applied during the sintering on the optical, structural, dielectric and electro-optic properties of the $(K_{0.5}Na_{0.5})_{0.95}Li_{0.05}Nb_{0.93}Bi_{0.07}O_3$ (KNNLB-5-2) ceramic is studied. The KNNLB-5-2 ceramic has good optical properties, so it is chosen for the investigation of the pressure effect, expecting that its optical properties will be more sensitive to the processing conditions. On the basis of the results, the optimum

pressure is determined and will be used for preparing the other KNNLB ceramics.

## 4.2 Optical Properties

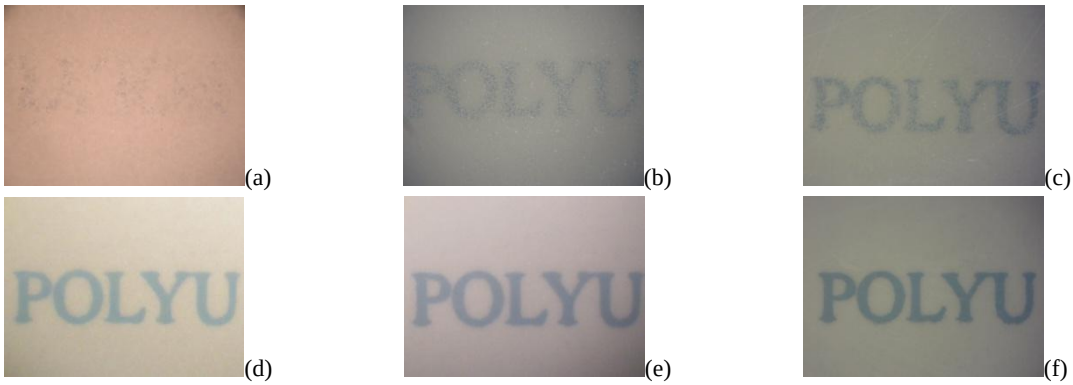


Figure 4.1 Photographs of the KNNLB-5-2 ceramics: (a) 0 MPa; (b) 2 MPa; (c) 3 MPa; (d) 6 MPa; (e) 10 MPa; (f) 20 MPa, the thickness is 0.5 mm

The KNNLB-5-2 ceramics were sintered under different pressures at 1060$^{o}$C for 4 h. The photographs of the KNNLB-5-2 ceramics are shown in Fig. 4.1. The photographs were taken under a stereo-microscope. The letters covered by the samples are in 8 point Times New Roman font. As demonstrated in Fig. 4.1, the ceramic sintered under 0 MPa is opaque. As the pressure increases, the optical transparency improves, and the ceramics sintered under a pressure higher than 6 MPa become optically transparent. It is noted the translucent ceramics (Fig. 4.1 b and c) contain a larger number of white spots, which are uniformly distributed in a transparent "matrix". It is suggested that these white spots are the cause for the poor optical transparency and should be produced from the non-optimized processing conditions.

The optical transmittances T of the KNNLB-5-2 ceramics sintered under different pressures are shown in Fig. 4.2. It can be seen that a low pressure (e.g. 2MPa) is effective in enhancing the transmittance, and the enhancement increases with increasing the pressure and becomes saturated quickly at around 10 MPa. Similar results have been observed for $Ba(La_{0.5}Nb_{0.5})O_3$-$PbZrO_3$-$PbTiO_3$ (Yokosuka, 1992). As shown in Fig. 4.1, the enhancement in transmittance should be partly resulted from the reduction of the white spots.

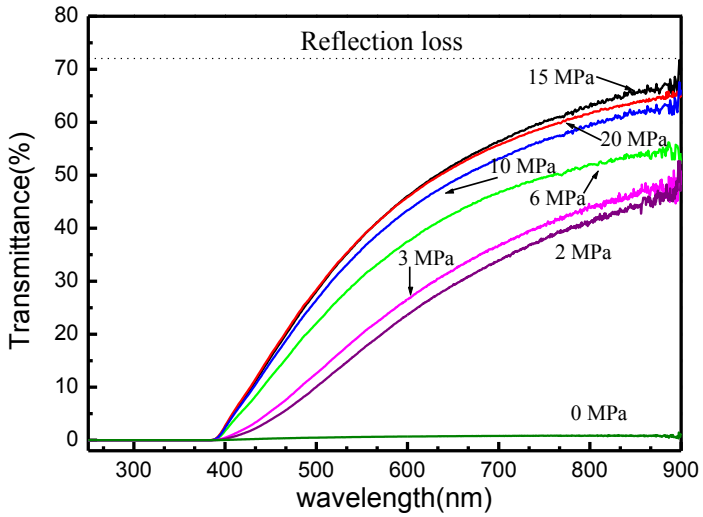


Figure 4.2 Optical transmittance spectra for the KNNLB-5-2 ceramics. The thickness is 0.5 mm.

For each ceramic (except the one sintered under a pressure of 0 MPa), the observed T increases rapidly from zero as the wavelength increases from ~390 nm and then becomes almost saturated in the near-IR region (Fig. 4.2). It can be seen that the KNNLB-5-2 ceramic sintered under a pressure of 15 MPa shows the highest transmittance in the wavelength range studied, and the observed T reaches a high value of 70% in the near-IR region. The reflection loss at the air-ceramic interface can be estimated from $R = (n - 1)^2/(n + 1)^2$, where $R$ is the reflectance and

*n* is the refractive index. By using *n* = 2.257 which is measured on the ceramic at 633 nm using a prism coupler (Metricon Model 2010), the reflection loss arisen at the two air-ceramic interfaces is calculated as ~28%. This indicates that if proper antireflection coating is applied, the transmittance to the ceramic can increase to higher than 90%.

Due to the interband transition, the observed T for the ceramics decreases to zero at wavelengths shorter than 390 nm (Fig. 4.2). According the Tauc equation (Tauc, 1972), the optical band gap energy $E_g$ can be estimated from the absorption spectra. For direct transition, the relationship between $E_g$ and the absorption coefficient $\alpha$ is given as:

$$(\alpha h\nu')^2 = A(h\nu' - E_g) \tag{4.1}$$

where $\nu'$ is the photon frequency, *h* is the Plank's constant and A is a constant. The absorption coefficient can be calculated from the transmittance T by (Naser, 2009)

$$\alpha = \frac{1}{L}\ln(\frac{1}{T}) \tag{4.2}$$

where *L* is the thickness of the sample. Accordingly, the band gap energy $E_g$ can be obtained by plotting $(\alpha h\nu')^2$ versus $h\nu'$ and extrapolating the linear portion of the curve to zero (Fig. 4.3). As shown in Table 4.1, the observed $E_g$ increases slightly from 3.10 to 3.15 eV as the pressure increases from 2 to 20 MPa. This is reasonable that the sintering pressure (one of the processing conditions) does not have significant effect on $E_g$. Our results are close to the reported value for KNN nanorods (3.09 eV) (Wang, 2010). For KNN, the band gap is corresponding to the transition from the top of the valence bands occupied by $O_{2p}$ electron state to the bottom of the conduction bands dominated by the empty $Nb_{4d}$ electron states.

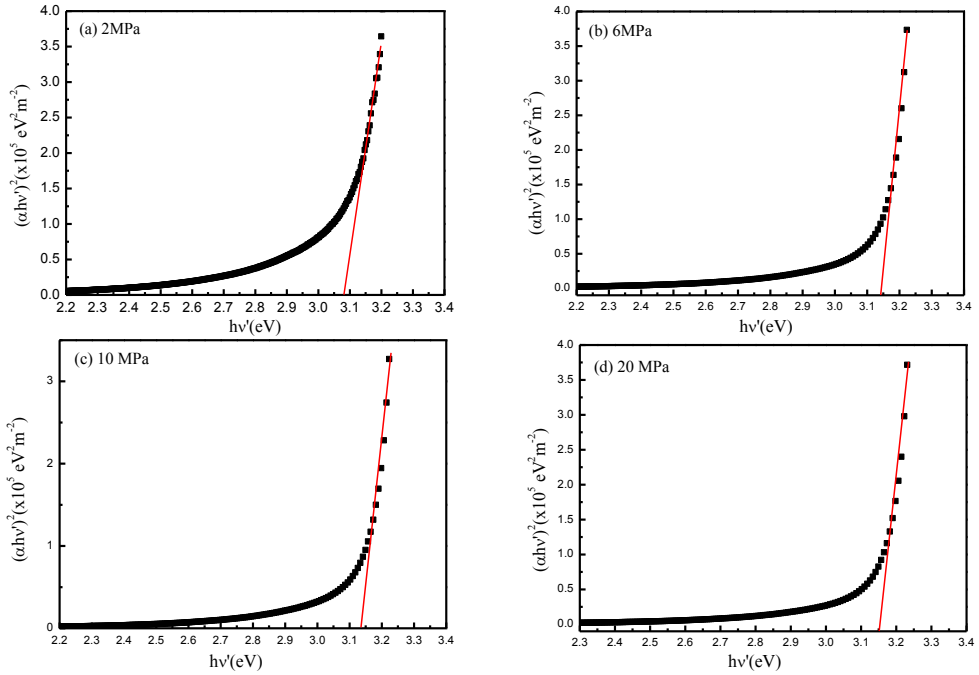


Figure 4.3 Plots of $(\alpha h\nu')^2$ against hν' for the KNNLB-5-2 ceramics with different pressure, from which the optical band gap energy $E_g$ is obtained by extrapolating the linear portion of the curve to zero.

Table 4.1 Optical band gap energy $E_g$ for the KNNLB-5-2 ceramics at different pressure.

| Pressure (MPa) | 0 | 2 | 3 | 6 | 10 | 15 | 20 |
|---|---|---|---|---|---|---|---|
| $E_g$ (eV) | - | 3.08 | 3.09 | 3.14 | 3.14 | 3.15 | 3.15 |

## 4.3 Microstructure

The SEM micrographs of the thermally etched surfaces of the KNNLB-5-2 ceramics sintered under different pressures are shown in Fig. 4.4. The average grain size is determined by the measurement of 200 grains on the SEM micrographs using the linear intercept method with a correction factor of 1.56 (Mendelso, 1969, Krell, 2003), and the results are shown in Table 4.2. It can be seen that all the

ceramics possess fine grains (normally < 0.8 μm) and good densification. Grain size, grain-boundary phase and pores are generally considered as the main factors affecting the transmittance of ceramics (Moulson, 2003, Apetz, 2003). So the good optical transparency of the ceramics sintered under a pressure higher than 6 MPa should be partly resulted from the reduced scattering of visible and IR lights by the fine grains (Apetz, 2003). For the ceramics sintered under a pressure less than 6 MPa, pores are observed from the SEM micrographs of the fracture surfaces of these ceramics (Fig. 4.5). It is suggested that the pores will scatter the light (appeared as white spots) and deteriorate the optical properties of the ceramics.

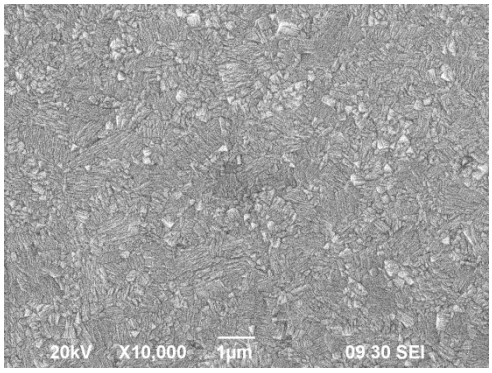


(a) pressure=0 MPa

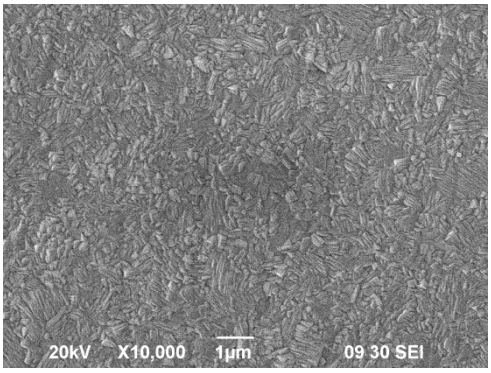


(b) pressure=3 MPa

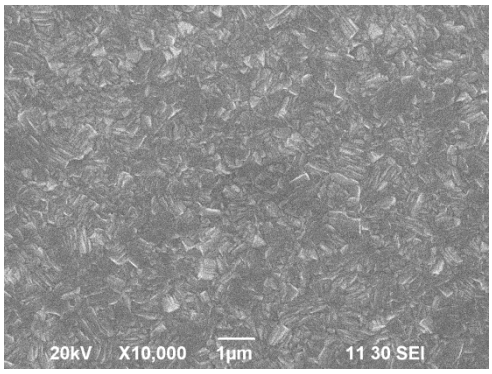


(c) pressure=10 MPa

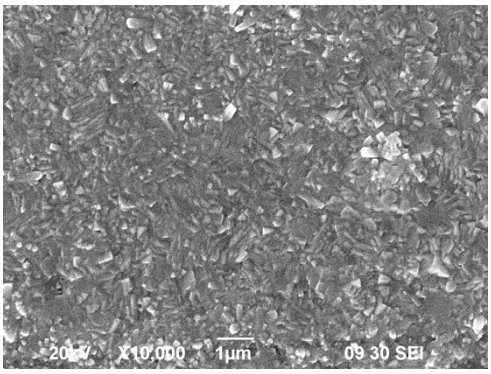


(d) pressure=20 MPa

Figure 4.4 SEM micrographs of the thermally etched surfaces of the KNNLB-5-2 ceramics with different pressure.

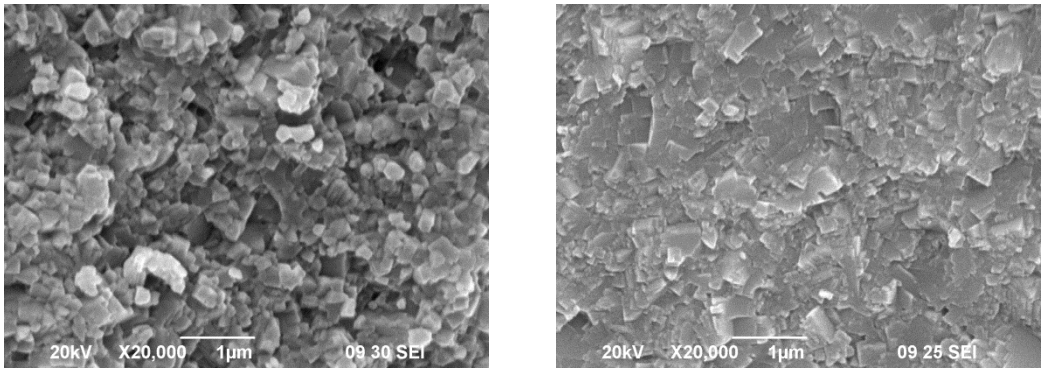


(a) pressure=0 MPa (b) pressure=10 MPa

Figure 4.5 SEM micrographs of the fracture surfaces of the KNNLB-5-2 ceramics with different pressure.

Table 4.2 Average grain size of KNNLB-5-2 ceramics at different applied pressure.

| Pressure (MPa) | 0 | 2 | 3 | 10 | 15 |
|---|---|---|---|---|---|
| Grain size (μm) | 0.80 | 0.78 | 0.73 | 0.56 | 0.55 |

On the basis of the results, it is suggested that the pressure applied in the hot-press sintering does not have significant effect on the grain growth. It is effective only in promoting uniform densification. As Table 4.3 shown, the observed density of the ceramics increases with increasing the sintering pressure, and a relative density of above 98% is obtained for the ceramic sintered under a pressure ≥ 10 MPa.

Table 4.3 The density of KNNLB-5-2 ceramics at different applied pressure.

| Pressure (MPa) | 0 | 2 | 3 | 6 | 10 | 15 | 20 |
|---|---|---|---|---|---|---|---|
| Density ($g/cm^3$) | 4.12 | 4.22 | 4.45 | 4.51 | 4.57 | 4.58 | 4.62 |
| Relative density (%) | 88.6 | 90.8 | 95.7 | 97.0 | 98.3 | 98.5 | 99.4 |

The effects of the sintering pressure on lead-base EO ceramics are different. It will enhance the densification as well as promote the grain growth for PLZT or PMN-PT ceramics, making them possess a dense structure with large grains (normally larger than 5 μm). The grain-boundaries also become thin and the area of

the grain-boundaries becomes small. As a result, the optical scattering at the grain boundaries is reduced and the optical clarity is improved.

## 4.4 Dielectric Properties

Fig. 4.6 shows the relative permittivity $\varepsilon_r$ and dielectric loss tanδ (measured at 100 kHz) for the KNNLB-5-2 ceramics sintered under different pressures. As the pressure increases from 0 to 3 MPa, the observed $\varepsilon_r$ increases from 915 to 1041, and then remains almost unchanged with increasing the pressure. Unlike $\varepsilon_r$, the observed tanδ decreases with increasing pressure and then remains at a value smaller than 0.03 at the pressure higher than 10 MPa. The enhancement in the dielectric properties should be partly due to the improvement in densification, as shown in Table 4.2.

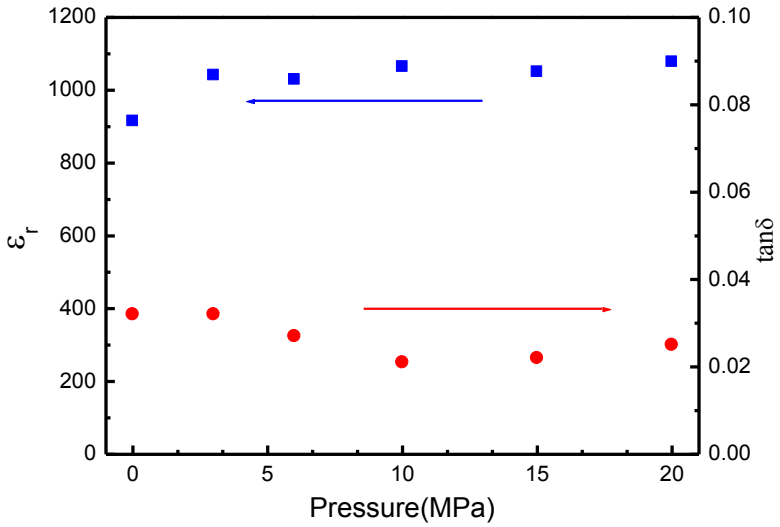


Figure 4.6 Variations of $\varepsilon_r$ and tanδ for the KNNLB-5-2 ceramics sintered under different pressures, measured at 100 kHz and room temperature.

## 4.5 Electro-Optic Properties

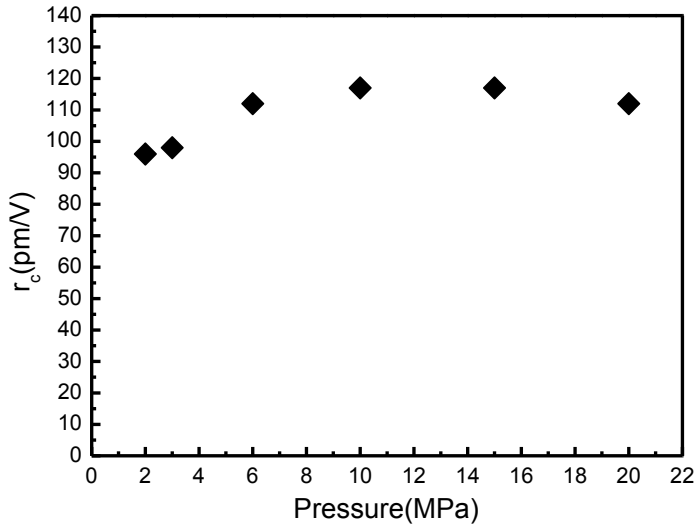


Figure 4.7 Variations of $r_c$ (measured at 1kHz and room temperature) for the KNNLB-5-2 ceramics sintered under different pressures.

Fig. 4.7 shows the effective linear EO coefficient $r_c$ for the KNNLB-5-2 ceramics sintered under different pressures. The ceramics were polarized under a d.c. field of 5 kV/mm at 150$^o$C for 30 min, and the measurements were carried out one day after the poling. A $n_e$ value of 2.257 (approximated by the value of an un-poled sample) was used to calculate the $r_c$ (Eq. 3.34). As shown in Fig. 4.7, the observed $r_c$ for the ceramics sintered under a pressure higher than 6 MPa are almost the same, ~ 115 pm/V. This indicates that the sintering pressure does not affect the EO properties of the ceramics significantly. The relatively lower value (~ 98 pm/V) of the ceramics sintered under lower pressures may be due to the error arisen from the weaker detected signal and the relatively lower relative permittivity (Fig. 4.6).

## 4.6 Conclusions

Lead-free transparent electro-optic $(K_{0.5}Na_{0.5})_{0.95}Li_{0.05}Nb_{0.93}Bi_{0.07}O_3$ ceramics have been successfully fabricated by hot-press sintering under different applied pressures. The effects of sintering pressure on the microstructure, optical, dielectric and electro-optic properties are investigated and the following conclusions are obtained:

(1) The sintering pressure is effective in enhancing the optical transmittance of the KNNLB-5-2 ceramics. A low sintering pressure (e.g., 2 MPa) is enough to enhance the optical transmittance, and the transmittance becomes saturated at around 10 MPa. The enhancement in transmittance should be partly due to the reduction of defects (e.g. white spots).

(2) Unlike the lead-based EO ceramics, the sintering pressure does not have significant effect on the grain growth. The pressure is effectively in improving the densification of the KNNLB-5-2 ceramics. In general, the density of the ceramics increases with increasing the pressure.

(3) Partly due to the improvement in densification, the dielectric properties are enhanced with increasing the sintering pressure. The observed $\varepsilon_r$ increases from 915 to 1041 when the sintering pressure increases from 0 to 3 MPa, and then remains almost unchanged with increasing the pressure. The observed tanδ decreases with increasing pressure and then remains at a value smaller than 0.03 at the pressure higher than 10 MPa.

(4) The sintering pressure does not have significant effects on the optical band gap energy $E_g$ and the effective linear EO coefficient $r_c$. For the KNNLB-5-2 ceramics sintered under a pressure higher than 6 MPa, $E_g$ ~ 3.14 eV and $r_c$ ~115 pm/V. The discrepancies for the ceramics sintered under a lower pressure should be due to the weaker signal arisen from the poorer optical transparency.

(5) Owing to the optimum optical and EO properties, the sintering pressure for the other KNNLB ceramics is selected as 10 MPa.

# Chapter 5 Effects of Lithium and Bismuth Co-modification

## 5.1 Introduction

As a good candidate for lead-free piezoelectric ceramic, the sinterability of KNN has been improved by using different sintering aids. It has been shown that the grain growth of KNN ceramics is dramatically suppressed and the density is enhanced with Bi doping (Wang, 2008). Due to the large difference in ionic radii, the substitution of $Li^+$ in the KNN lattices will cause a large distortion of the $BO_6$ octahedron, which can improve the EO effect. These hence suggest that, by the co-modification of Li and Bi, the KNN ceramic may exhibit good optical and EO properties. In this chapter, the effects of the Li and Bi co-modification on the optical properties, crystallite structure, microstructure, and EO properties of KNNLB ceramics are investigated. $(K_{0.5}Na_{0.5})_{1-x}Li_xNb_{1-x}Bi_xO_3$ (x varying from 0 to 0.09) ceramics (abbreviated as KNNLB-100x) are used for this investigation. The ceramics were sintered at 1060°C for 4 h under a uniaxial pressure of 10 MPa. The sintered ceramics were polished to 0.5mm with 1-μm diamond paste for the following measurements.

## 5.2 Optical Properties


(d) (c) (b) (a)

Figure 5.1 Photograph of the KNNLB-100x transparent ceramics: (a) x = 0.02; (b) x = 0.03; (c) x = 0.05; and (d) x = 0.07.

A photograph of the KNNLB-100x ceramics is shown in Fig. 5.1, while their optical transmittances T measured in the range of 300-900 nm are shown in Figs. 5.2 and 5.3. As demonstrated in Fig. 5.1, the ceramics with $x \leq 0.02$ are opaque. As x increases, the optical transparency improves and the ceramics with $x \geq 0.05$ become optically transparent. The improvement in optical transparency is also revealed in the optical transmittance spectra. As shown in Fig. 5.2, the observed T (at any wavelengths) increases considerably as x increases from 0.02 to 0.05, and then decreases slightly and becomes almost unchanged with increasing x. For each ceramic (with $x \geq 0.04$), the observed T increases rapidly from zero as the wavelength increases from ~390 nm, and becomes almost saturated in the near-IR region (Fig. 5.3).

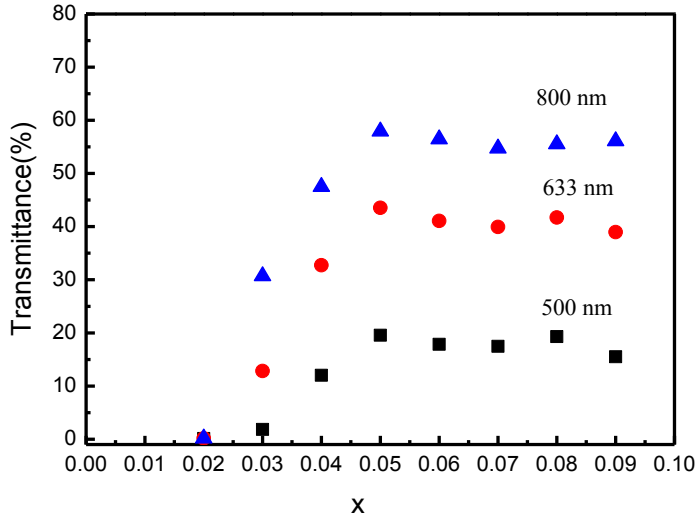


Figure 5.2 Optical transmittances measured at different wavelengths for the KNNLB-100x ceramics.

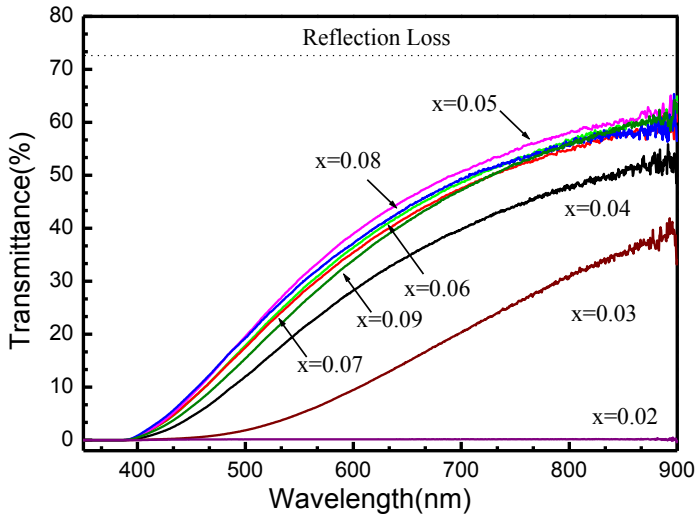


Figure 5.3 Optical transmittance spectra for the KNNLB-100x ceramics.

It can be seen that the KNNLB-5 ceramic exhibits the highest transmittance in the wavelength range studied, and the observed T reaches a high value of 60% in the near-IR region. It is anticipated that the transmittance in the visible region can be further improved by optical-grade polishing. Moreover, if proper antireflection coating is applied to eliminate the reflection loss at the air-ceramic interfaces, the transmittance of the ceramic can be increased to a high value of ~90%. The

reflection loss at the air-ceramic interface can be estimated from $R = (n - 1)^2/(n + 1)^2$, where $R$ is the reflectance and $n$ is the refractive index (2.257).

Due to the interband transition, the observed T for the ceramics decreases to zero at wavelengths shorter than 390 nm (Fig. 5.3). The optical band gap energy $E_g$ for KNNLB-100x ceramics is list in Table 5.1

Table 5.1 Optical band gap energy $E_g$ for the KNNLB-100x ceramics.

| x | 0.03 | 0.04 | 0.05 | 0.06 | 0.07 | 0.08 | 0.09 |
|---|---|---|---|---|---|---|---|
| $E_g$ (eV) | 2.93 | 3.08 | 3.09 | 3.11 | 3.12 | 3.12 | 3.12 |

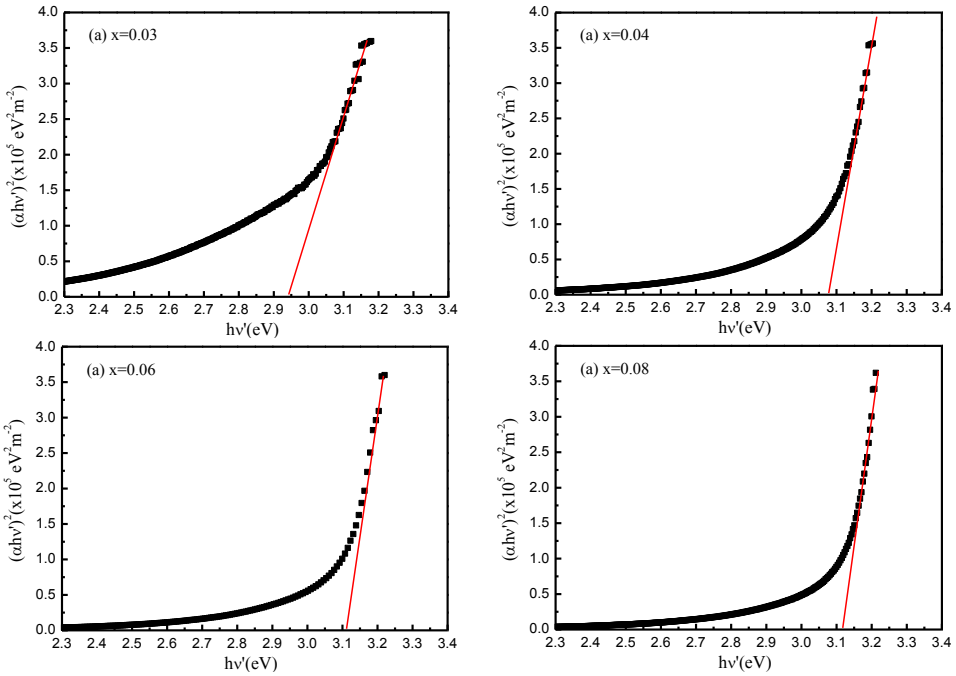


Figure 5.4 Plots of $(\alpha h\nu')^2$ versus hν' for the KNNLB-100x ceramics, from which the optical band gap energy $E_g$ is obtained by extrapolating the linear portion of the curve to zero.

As shown in Table 5.1, the observed $E_g$ increases slightly from 3.08 to 3.12 eV as x increases from 0.04 to 0.09, suggesting that there is only a minor effect of the modifiers (Li and Bi) on the band gap of the ceramics. As the observed T for the KNNLB-3 ceramic is small, the linear portion of the curve is short and hence the

extrapolated $E_g$ value (2.93 eV) may not be accurate enough (Fig. 5.4a). Our results for the ceramics with $x \geq 0.04$ are close to the reported value for KNN nanorods (3.09 eV) (Wang, 2010). For KNN, the band gap is corresponding to the transition from the top of the valence bands occupied by $O_{2p}$ electron state to the bottom of the conduction bands dominated by the empty $Nb_{4d}$ electron states.

## 5.3 Microstructure

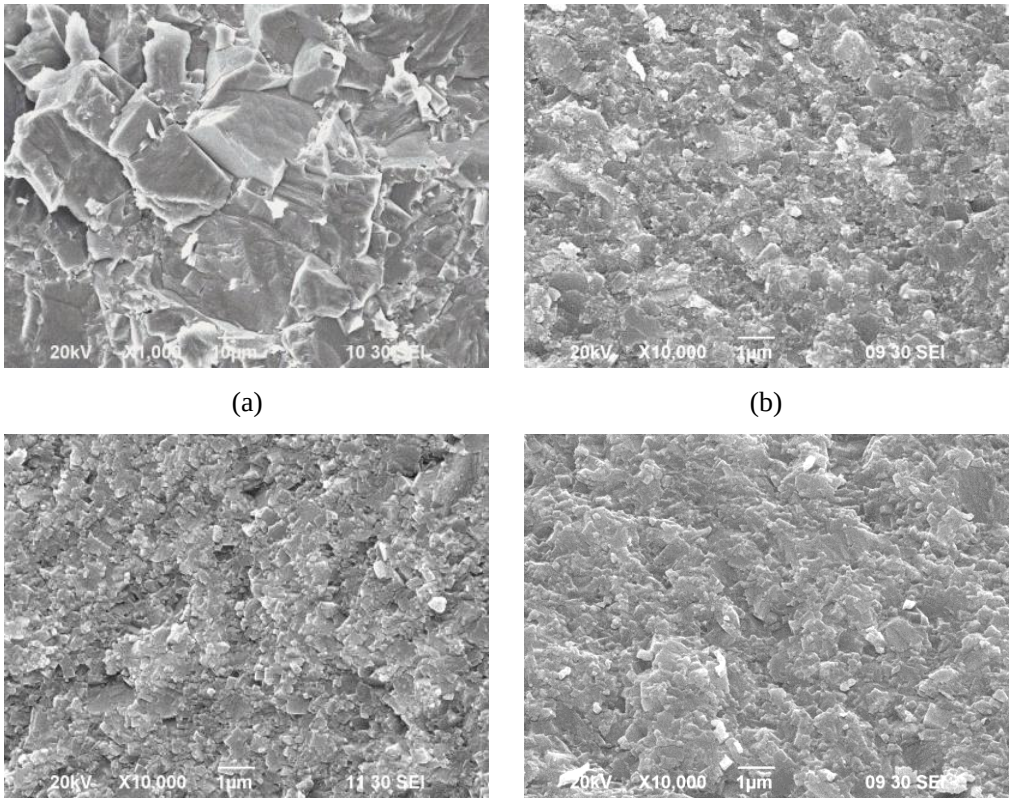


(a) (b)

(c) (d)

Figure 5.5 SEM micrographs of the fracture surfaces of the KNNLB-100x ceramics: (a) x = 0; (b) x = 0.03; (c) x = 0.05; (d) x = 0.07.

Fig. 5.5 shows, as examples, the SEM micrographs of the fracture surfaces of the KNNLB-100x ceramics with x = 0, 0.03, 0.05 and 0.07. Similar results have been observed for the other KNNLB-100x ceramics. It can be seen that all the

ceramics are dense and exhibit cuboid morphologies, which are typical for KNN-based ceramics. The density results and average grain size for the KNNLB-100x ceramics are shown in Table 5.2 and 5.3 separately. It can be seen that with increasing x, the densification is improved and the average grain size decreases. The grains of the modified ceramics (< 1 μm) are substantially smaller than those of the un-modified ceramic (> 20 μm). Similar results have been shown that the grain growth of perovskite ceramics can be significantly suppressed by Bi-doping (Skidmore, 2010, Wang, 2004).

Table 5.2 Density for the KNNLB-100x ceramics.

| x | 0.01 | 0.02 | 0.03 | 0.04 | 0.05 | 0.06 | 0.07 | 0.08 | 0.09 |
|---|---|---|---|---|---|---|---|---|---|
| Density ($g/cm^3$) | 4.30 | 4.33 | 4.38 | 4.43 | 4.57 | 4.61 | 4.62 | 4.66 | 4.68 |
| Relative density (%) | 94.3 | 94.5 | 95.0 | 95.5 | 98.1 | 98.3 | 97.9 | 98.1 | 98.1 |

Table 5.3 Average grain size for the KNNLB-100x ceramics.

| x | 0.01 | 0.02 | 0.03 | 0.04 | 0.05 | 0.06 | 0.07 | 0.08 | 0.09 |
|---|---|---|---|---|---|---|---|---|---|
| Grain size (μm) | 0.76 | 0.72 | 0.70 | 0.69 | 0.67 | 0.67 | 0.66 | 0.66 | 0.62 |

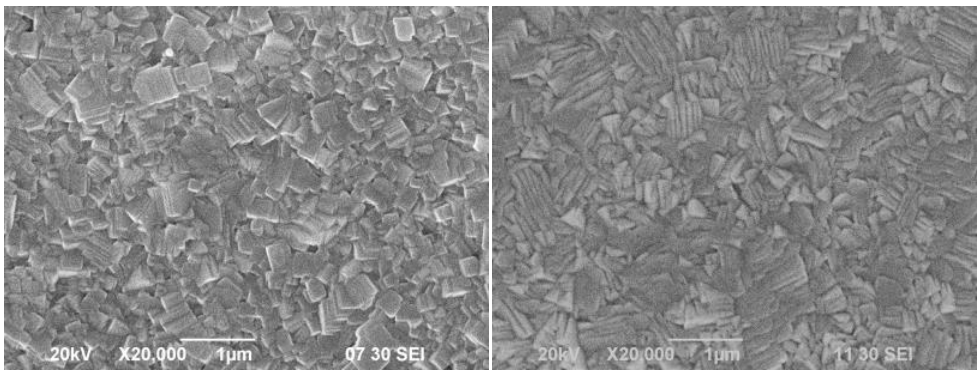


(a) (b)

Figure 5.6 SEM micrographs of the thermally etched surfaces of the KNNLB-100x ceramics: (a) x = 0.04; (b) x = 0.06.

In the KNNLB-x ceramics, $Bi^{3+}$ may concentrate near the grain boundaries and decrease their mobility during the densification. As a result, the mass transportation becomes weakened and the grain growth is inhibited. For the ceramics with $x \geq 0.04$, the grains are even smaller, generally < 0.7 μm (Fig. 5.6 and Table 5.3). Therefore, unlike the lead-based EO ceramics, the good optical transparency of those ceramics (Figs.5.1 – 5.3) should be partly resulted from the reduced scattering of visible and IR lights by the fine grains (Apetz, 2003). Grain size, grain-boundary phase and pores are generally considered as the main factors affecting the transmittance of ceramics (Moulson, 2003, Apetz, 2003). Owing to the hot-press sintering, the microstructure of the lead-based EO ceramics is dense and the grains are large, normally larger than 5 μm (Jiang, 2005). The grain-boundary then becomes thin, the area of the grain-boundary becomes small, and thus the optical scattering is reduced.

## 5.4 Crystalline Structure

The XRD patterns of the KNNLB-100x ceramics are shown in Fig. 5.7. All the ceramics possess a single-phase perovskite structure. This suggests that $Li^+$ and $Bi^{3+}$ have diffused into the KNN lattices, with $Li^+$ entering the $(K_{0.5}Na_{0.5})^+$ sites and $Bi^{3+}$ occupying the $Nb^{5+}$ sites. As the ionic radius ratio of $Bi^{3+}$ (0.96Å) to $O^{2-}$ (1.32 Å) is smaller than 0.732, the $Bi^{3+}$ ions enter the B-sites. After the modification, the two diffraction peaks (202) and (020) of the ceramics become merged together (Fig. 5.7b), suggesting that the lattice constants *a*, *b* and *c* become close to each other. This also suggests that the ceramics may have a tendency to transform into another

phase, e.g., pseudocubic. Similar results have been observed for other KNN-based ceramics, e.g., Ta-modified KNN (Lin, 2008), KNN-$BaTiO_3$ (Lin 2007) and KNN-$AgSbO_3$ (Lin 2009) ceramics.

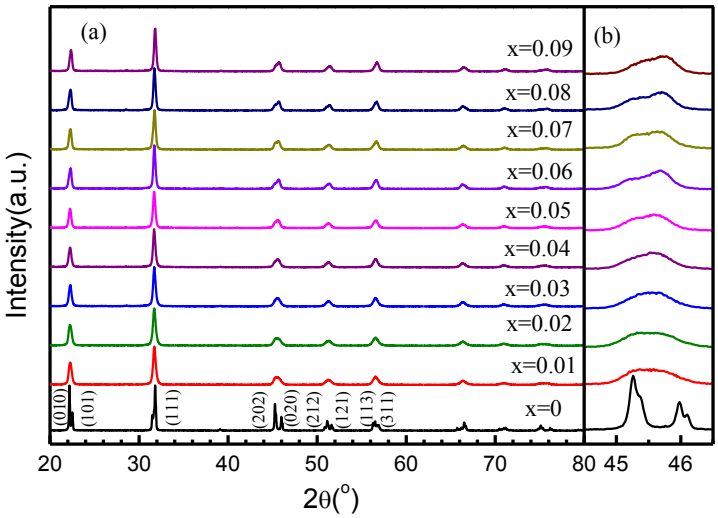


Figure 5.7 XRD patterns for the KNNLB-100x ceramics.

The lattice constants of the ceramics were refined using all the diffraction peaks shown in Fig. 5.7 by the Rietveld method. Although the results on phase transition (given below) suggest that the crystal structure of the KNNLB-1 ceramic may be orthorhombic while the ceramics with $x \geq 0.02$ may be tetragonal, the exact crystal structure of the KNNLB-100x ceramics is not very clear yet. In this work, different crystal models, including tetragonal *P*4*mm*, orthorhombic *Amm*2 and monoclinic *Pm*, have been used for the refinements. Probably due to the cubic-like crystal structure, similar results with reasonably good fits have been obtained for all the models. Both the orthorhombic (Wu, 2008) and monoclinic (Shiratori, 2005, Tellier, 2009) unit cells have been used for the refinement of the KNN cell parameters, and only a small difference between the orthorhombic and monoclinic structures is noted. More detailed investigations are needed to identify the crystal

structure of the KNNLB-100x ceramics. However, with the aim of revealing the cubic-like crystal structure, the calculated lattice parameters together with the reliability factor $R_{wp}$ and goodness-of-fit indicator S using the monoclinic model which provides the best fit are given in Table 5.4 for discussion. The low $R_{wp}$ (<15%) and S (<2) values denote a good fit between the observed and calculated patterns (MAUD n.d.).

As shown in Table 5.4, the lattice constant *c* remains almost unchanged after the co-modification with Li and Bi. On the other hand, as x increases, *a* decreases and *b* increases, and both become saturated at high x. It can also be seen that the difference between *c* and *b* decreases with increasing x. For the ceramics with x ≥ 0.03, the difference is only about ~0.04 Å (or ~ 1%). This suggests that those ceramics possess a cubic-like crystal structure with minimal optical anisotropy. As a result, the light scattering is reduced and the optical transparency is improved (Figs. 5.1 – 5.3). It has been known that one of the major causes for the high transparency of the electro-optically useful PLZT is their cubic-like structure, with *c* being typically about 1% larger than *a* (Moulson, 2003).

Table 5.4 Lattice constants *a*, *b* and *c* for the KNNLB-100x ceramics.

| x | 0 | 0.01 | 0.02 | 0.03 | 0.04 | 0.05 | 0.06 | 0.07 | 0.08 | 0.09 |
|---|---|---|---|---|---|---|---|---|---|---|
| *a* (Å) | 3.999 | 3.981 | 3.981 | 3.978 | 3.974 | 3.975 | 3.970 | 3.973 | 3.968 | 3.970 |
| *b* (Å) | 3.942 | 3.956 | 3.955 | 3.960 | 3.960 | 3.958 | 3.960 | 3.958 | 3.955 | 3.957 |
| *c* (Å) | 4.002 | 4.001 | 4.002 | 3.999 | 3.998 | 3.998 | 3.999 | 3.996 | 3.996 | 3.994 |
| *β* (°) | 90.03 | 90.29 | 90.31 | 90.31 | 90.34 | 90.33 | 90.43 | 90.34 | 90.40 | 90.35 |

## 5.5 Dielectric Properties

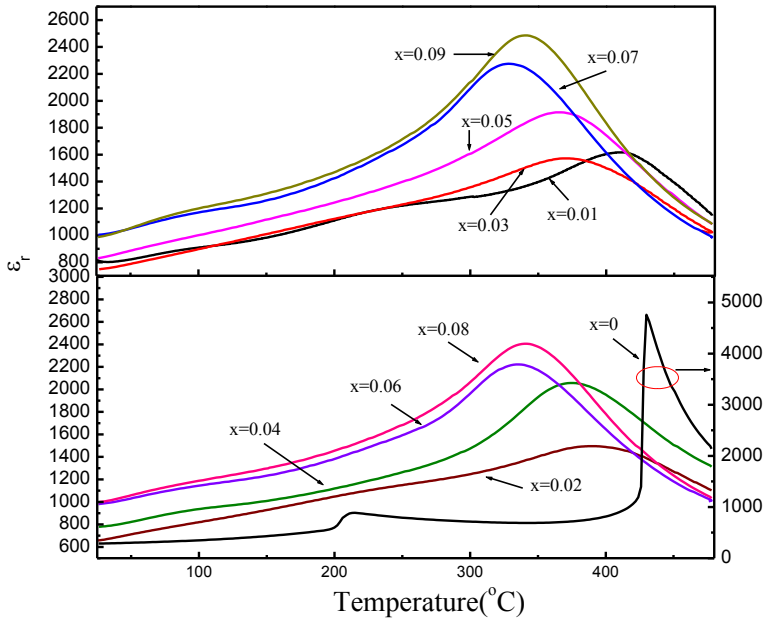


Figure 5.8 Temperature dependences of $\varepsilon_r$ for the KNNLB-100x ceramics.

The temperature dependence of $\varepsilon_r$ for the KNNLB-100x ceramics is shown in Fig. 5.8. To eliminate the contributions of space-charge polarization/ionic conduction at low frequencies and high temperatures, the observed $\varepsilon_r$ at 100 kHz are used for the temperature plots as well as the subsequent analyses. As shown in Fig.5.8, the un-modified (i.e. x = 0) ceramic exhibits two transition peaks: one is associated with the paraelectric cubic-ferroelectric tetragonal phase transition at 425°C and the other is the ferroelectric tetragonal-ferroelectric orthorhombic phase transition at 226°C. After the co-modifications with Li and Bi, all the ceramics exhibit a broadened cubic-tetragonal transition peak at lower temperatures. As x increases from 0 to 0.06, the observed $T_m$ (the temperature of maximum $\varepsilon_r$) decreases from 425 to 330°C, and then remains almost unchanged with increasing x

(see Fig. 5.10). It can also be seen that only the KNNLB-1 ceramic exhibits a very weak tetragonal-orthorhombic transition (~230°C) in the temperature range studied (i.e. 25 - 500°C). As discussed in the previous section, the exact crystal structure of the ceramics is not clear yet. The "disappearance" of the tetragonal-orthorhombic transition in the temperature range studied may be arisen from the cubic-like crystal structure.

The broadening of the cubic-tetragonal transition peaks suggests that a diffuse phase transition is induced in the modified ceramics (Fig. 5.8). For a normal ferroelectric, the relative permittivity $\varepsilon_r$ above the Curie temperature $T_C$ should obey the Curie-Weiss law: $\varepsilon_r = C/(T-T_C)$, where C is the Curie-Weiss constant. Deviation from the Curie-Weiss law can be defined by $\Delta T_m = T_B - T_m$, where $T_B$ is the temperature from which $\varepsilon_r$ starts to follow the law. At $T < T_B$, the paraelectric phase transforms into the ergodic relaxor state and forms the polar nano-regions (Bokov, 2006).

Fig. 5.9 shows, as examples, the plots of $1/\varepsilon_r$ versus T for the ceramics with x = 0, 0.03, 0.06 and 0.09, while the observed $T_B$, $T_m$ and $\Delta T_m$ for all the ceramics are shown in Fig. 5.10. As shown in Fig. 5.9a, the observed $T_B$ is the same as $T_m$ for the KNNLB-0 ceramic, indicating that it is a classical ferroelectric. For the modified ceramics, the observed $\varepsilon_r$ starts to obey the Curie-Weiss laws at a temperature higher than $T_m$. The calculated $\Delta T_m$ increases with increasing x (Fig. 5.10), suggesting that a diffuse phase transition is induced and becomes enhanced in the ceramics with higher x.

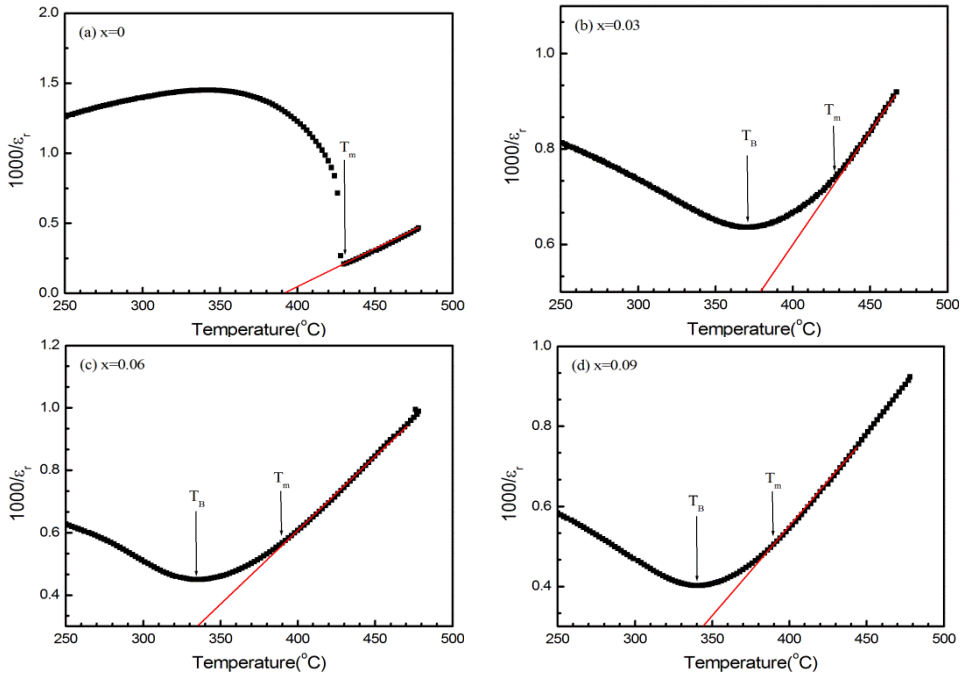


Figure 5.9 Plots of $1/\varepsilon_r$ versus $T$ for the KNNLB-100x ceramics. The symbols denote the experimental data, while the solid lines denote the least-squares fitting lines to the Curie-Weiss law.

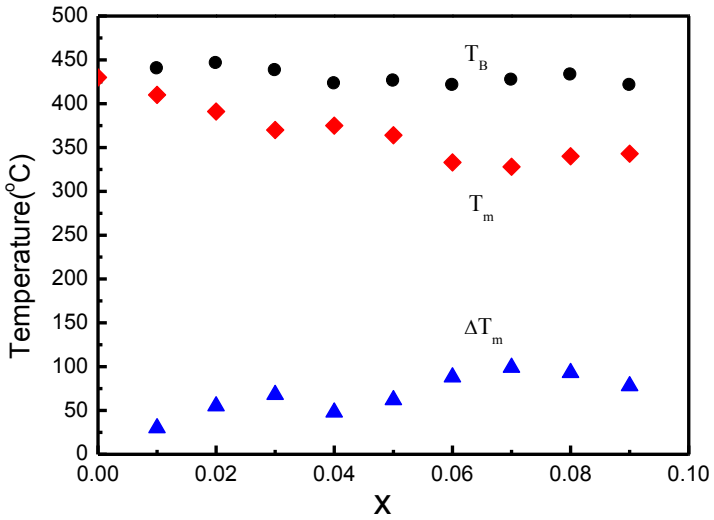


Figure 5.10 Variations of $T_B$, $T_m$ and $\Delta T_m$ with x for the KNNLB-100x ceramics.

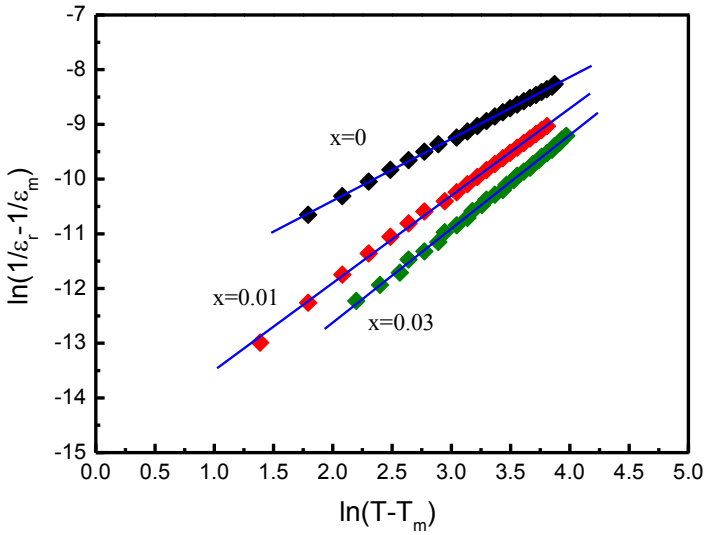


Figure 5.11 Plots of $\ln(1/\varepsilon_r - 1/\varepsilon_m)$ versus $\ln(T-T_m)$ for the KNNLB-100x ceramics. The symbols denote the experimental data, while the solid lines denote the least-squares fitting lines to the modified Curie-Weiss law.

Table 5.5 Degree of diffuseness $\gamma$ for the KNNLB-100x ceramics.

| x | 0 | 0.01 | 0.02 | 0.03 | 0.04 | 0.05 | 0.06 | 0.07 | 0.08 | 0.09 |
|---|---|---|---|---|---|---|---|---|---|---|
| $\gamma$ | 1.04 | 1.67 | 1.72 | 1.87 | 1.80 | 1.81 | 1.81 | 1.87 | 1.74 | 1.73 |

The diffuseness of a phase transition can be determined from the modified Curie-Weiss law (Uchino, 1980),

$$\frac{1}{\varepsilon_r} - \frac{1}{\varepsilon_m} = \frac{(T - T_m)^{\gamma}}{C_1} \qquad (5.1)$$

where $\varepsilon_m$ is the maximum value of $\varepsilon_r$ at $T_m$, $\gamma$ is the degree of diffuseness, and $C_1$ is the Curie-like constant. $\gamma$ can have a value ranging from 1 for a normal ferroelectric to 2 for an ideal relaxor ferroelectric. Fig. 5.11 shows, as examples, the plots of $\ln(1/\varepsilon_r - 1/\varepsilon_m)$ versus $\ln(T-T_m)$ for the KNNLB-x ceramics with x = 0, 0.01 and 0.03. By least-squares fitting the experimental data to the modified Curie-Weiss law, $\gamma$ is determined, giving the results listed in Table 5.5. It can be seen that the observed $\gamma$ for the modified ceramics is quite large, in the range of 1.73 - 1.87. This suggests

that the ceramics, in particular for those with x ≥ 0.03, become more relaxor-like, i.e. more close to a relaxor ferroelectric.

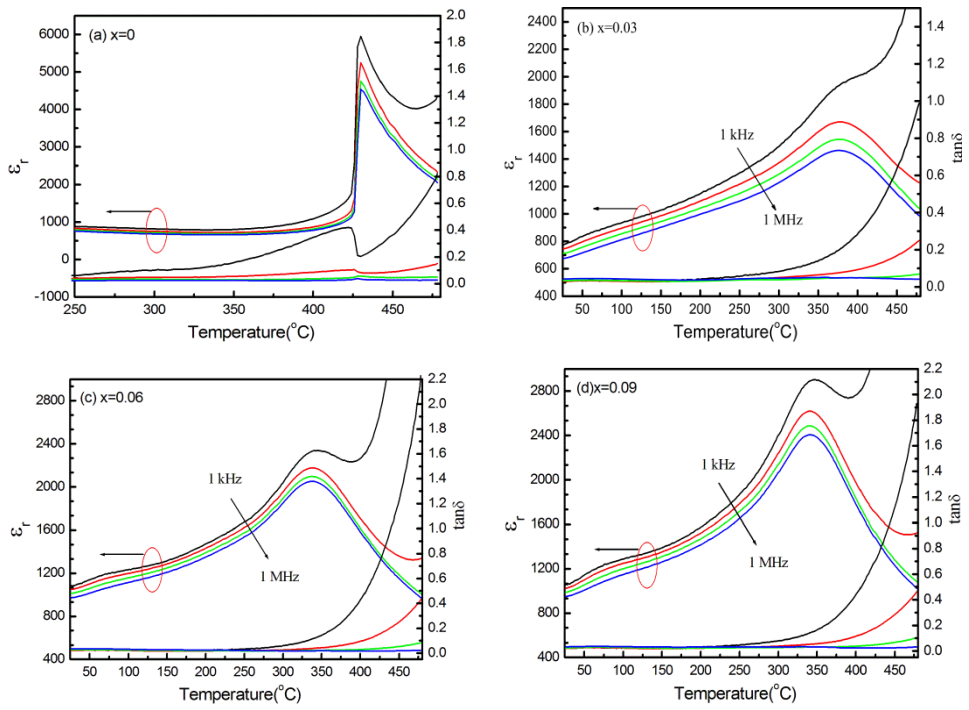


Figure 5.12 Temperature dependences of $\varepsilon_r$ and tanδ at different frequencies for the NNLB-100x ceramics: (a) x = 0; (b) x = 0.03; (c) x = 0.06; (d) x = 0.09.

Fig. 5.12 shows, as examples, the temperature dependences of $\varepsilon_r$ and tanδ measured at 1 kHz, 10 kHz, 100 kHz and 1 MHz for the ceramics with x = 0, 0.03, 0.06, 0.09. Similar results have been observed for the other KNNLB-100x ceramics. For the modified ceramics, the observed $\varepsilon_r$ decreases generally with increasing the frequency. However, unlike the typical relaxor ferroelectrics, an increase in $T_m$ with frequency has not been observed. This may be partly due to the increase in electronic conduction at high temperatures (see the tanδ plots in Fig. 5.12), which causes the observed $\varepsilon_r$ to increase significantly and the transition peak to become distorted asymmetrically with $T_m$ shifted to higher temperatures. It has been

reported that the change in $T_m$ for KNN-based relaxors is not large (Du, 2007, Guo 2004); for instance, it increases only from 145 to 152°C as the frequency increases from 100 Hz to 1 MHz for the 0.9KNN-0.1$SrTiO_3$ relaxor (Guo 2004).

A diffuse phase transition has been observed in a number of $ABO_3$-type perovskites (Guo 2004, Lin 2007, Lin 2009). In those compounds, either the A-sites or the B-sites are occupied by two or more cations. It is known that a large difference in ionic radii of the A-site cations or B-site cations is favorable for the formation of ordered structures (Uchino, 1980). As $Li^+$ (0.68 Å) is much smaller than $Na^+$ and $K^+$ (0.97 and 1.38 Å), the substitution of $Li^+$ in the KNN lattices should be favorable for forming an ordered structure and hence would not induce a diffuse phase transition (Lin 2007). On the other hand, the differences in valences, ionic radii and electronegativities between different ions are the main reasons for the disorder structure (Samara, 2003). As a result, with increasing $Bi^{3+}$ content, the degree of disorder on the B-sites and the local compositional fluctuation in the KNNLB-100x ceramics increase, making the ceramics become more relaxor-like and exhibit a diffuse phase transition. Accordingly, the KNNLB-100x ceramics should contain considerable amount of polar nano-regions (which may have a slightly larger size and higher relaxation frequency as compared with a relaxor ferroelectric (Wei, 2003) ), and hence the light scattering (arisen at the domain walls) is reduced and the optical transparency is improved (Figs. 5.1 – 5.3).

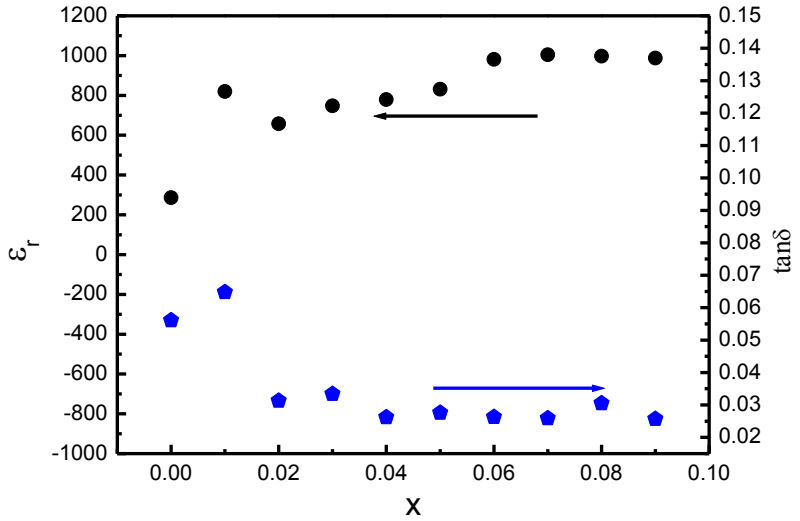


Figure 5.13 Variations of $\varepsilon_r$ and tanδ (measured at 100 kHz and room temperature) with x for the KNNLB-100x ceramics.

The variations of $\varepsilon_r$ and tanδ (measured at 100 kHz and room temperature) with x for the KNNLB-100x ceramics are shown in Fig. 5.13. As x increases from 0 to 0.06, the observed $\varepsilon_r$ increases from 290 to 980, and then remains almost unchanged with increasing x. Unlike $\varepsilon_r$, the observed tanδ decreases with increasing x and then remains at a value smaller than 0.03 at $x \geq 0.04$. The enhancement in the dielectric properties should be partly due to the improvement in densification and partly due to the substitution of $Li^+$ (Lin 2007, Hollenstein, 2007). The low dielectric loss (< 0.03) suggests that the ceramics (with $x \geq 0.04$) are ready for use in practical applications.

## 5.6 Ferroelectric Properties

Fig. 5.14 shows the ferroelectric hysteresis (*P*-*E*) loops for the KNNLB-100x ceramics, while Fig. 5.15 summarizes the variation of the remnant polarization $P_r$ and coercive field $E_c$ with x. The *P*-*E* loops were measured at a frequency of 100 Hz under an electric field of 8.4 kV/mm at room temperature.

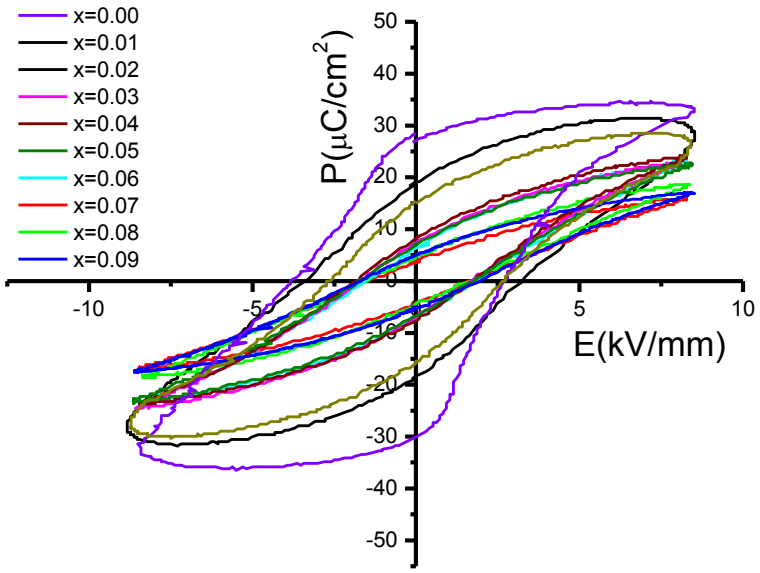


Figure 5.14 Hysteresis loops of KNNLB-100x ceramics at room temperature.

As shown in Fig. 5.15, a small amount of Li and Bi doping (x=0.03) weakens the $P_r$ and $E_c$ significantly. The ferroelectric response of lead free ceramics is favored by the larger grain size, the homogeneous microstructure, and tetragonal symmetry (Rubio-Marcos, 2007). Partly due to the small grain size (see Fig. 5.5) and cubic-like symmetry (see Fig. 5.7), the ceramics with $x \geq 0.03$ exhibit slim *P*-*E* loop. The difference between *c* and *a*/*b* decreases with increasing x (Table 5.2). This is another reason for the slimmer *P*-*E* loop (Hao, 2005). Combined with the

previously shown dielectric properties, KNNLB-100x ceramics with x ≥ 0.01 have relaxor-like characteristics.

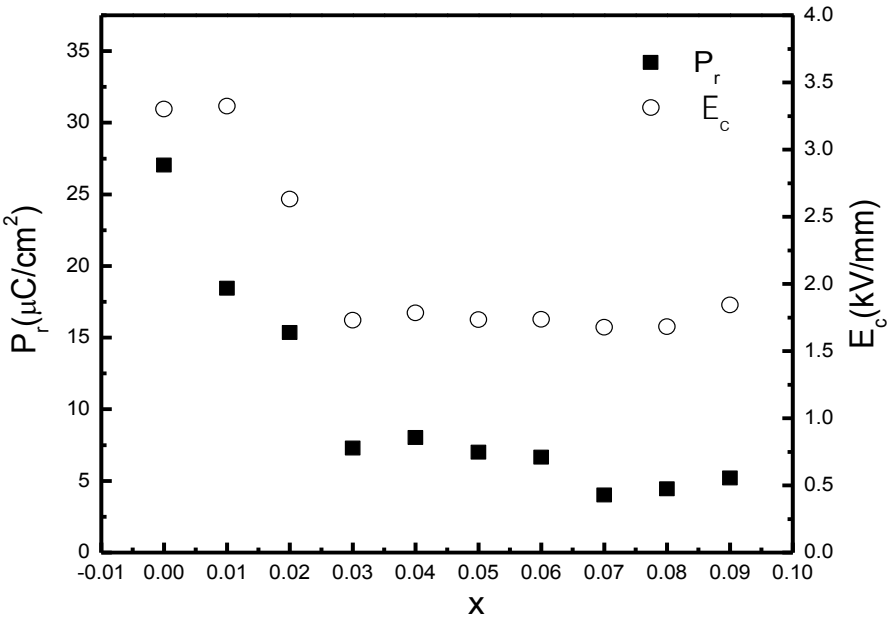


Figure 5.15 The composition dependence of $P_r$ and $E_c$.

## 5.7 Electro-Optic Properties

The effective linear EO coefficient $r_c$ of the KNNLB-100x ceramics have been measured and the results are listed in Table 5.6. The ceramics were polarized under a d.c. field of 5 kV/cm at 150°C for 30 min, and the measurements were carried out one day after the poling. A $n_e$ value of 2.257 (approximated by the value of an un-poled sample) was used in the calculation of $r_c$. As shown in Table 5.4, the observed $r_c$ increases with increasing x. Although a relax behavior is induced, the observed $r_c$ for the KNNLB-x ceramics with x ≥ 0.04 is quite large (120 - 200 pm/V), which is about 6-10 times larger than that of $LiNbO_3$ (19.9 pm/V) (Aillerie, 1989). It is also as good as the PMN-PT single crystals with rhombohedral and tetragonal structures (Wan, 2004)

Table 5.6 Effective linear EO coefficient $r_c$ for the KNNLB-100x ceramics.

| x | 0.03 | 0.04 | 0.05 | 0.06 | 0.07 | 0.08 | 0.09 |
|---|---|---|---|---|---|---|---|
| $r_c$ (pm/V) | 44 | 133 | 121 | 155 | 160 | 168 | 198 |

As compared with the Bi-modified KNN ceramics, the Li/Bi co-modified KNN ceramics generally exhibit larger $r_c$ and $\varepsilon_r$ (Li, 2011, Kwok, 2011). For example, the observed $r_c$ and $\varepsilon_r$ for the KNNLB-7 ceramic are 160 pm/V and 1000, respectively; while those for the $K_{0.45}Na_{0.52}Nb_{0.925}Bi_{0.075}O_3$ ceramic are 43 pm/V and 716 (Li, 2011). The improvement of $r_c$ in the Li/Bi co-modified ceramics should be partly due to the large distortion of $BO_6$ octahedron (Shih, 1982) and partly due to the increase in $\varepsilon_r$ (DrDomenico, 1969, Burns, 1968), both are resulted from the substitution of $Li^+$ in the KNN lattices. On the basis of theoretical calculations, Shih and Yariv have shown that a distorted octahedral structure is a promising mechanism for a strong electro-optic response (Shih, 1982). By considering the ferroelectric phase as a quadratic phase biased with a spontaneous polarization $P_s$, $r_c$ can be related to $\varepsilon_r$ and $P_s$ via a general equation (DrDomenico, 1969, Burns, 1968):

$$r_c = 2\varepsilon_o \varepsilon_r g_c P_s \qquad (5.3)$$

where $g_c$ is the polarization-related quadratic electro-optic coefficient and $\varepsilon_o$ is the vacuum permittivity. The equation has been found to hold in a number of oxygen-octahedra crystals, such as $LiNbO_3$, $LiTaO_3$, $NaBa_2Nb_5O_{15}$, $KSr_2Nb_5O_{15}$, and $0.88Pb(Zn_{1/3}Nb_{2/3})O_3$-$0.12PbTiO_3$ (DrDomenico, 1969, Burns, 1968, He, 2012). It is probable that the $Li^+$ content and then the lattice distortion in the KNNLB-3 ceramic are not large enough to engender a strong electro-optic response.

## 5.8 Conclusions

Lead-free transparent electro-optic ceramics $(K_{0.5}Na_{0.5})_{1-x}Li_xNb_{1-x}Bi_xO_3$ have been successfully fabricated by hot-press sintering. The grain growth of the ceramics is considerably suppressed. The ceramics hence generally possess a dense and fine-grained structure. Our results reveal that the co-modification with Li and Bi induces a transformation of crystal structure from orthorhombic to nearly cubic. As a result, the optical anisotropy and hence the scattering of light at the grain boundaries are greatly reduced. The co-modification also induces a diffuse phase transition, making the ceramics become more relaxor-like and contain more polar nano-regions (i.e., the relaxor characteristics). The amount of domain walls and then the resulting light scattering are further eliminated. For the KNNLB-5 ceramic, the observed T reaches a high value of 60% in the near-IR region. Owing to the large distortion of $BO_6$ octahedron and increase in $\varepsilon_r$ arisen from the substitution of $Li^+$ in the KNN lattices, the Li/Bi co-modified ceramics exhibit strong EO response, giving a large effective linear EO coefficient (120-200 pm/V), which is about a few times larger than that of the Bi-modified KNN ceramics.

# Chapter 6 Effects of Excess Bismuth

## 6.1 Introduction

It has been shown that the grain growth of perovskite ceramics can be significantly suppressed by Bi-doping as well as excess $Bi_2O_3$ (Wang, 2005). It is hence of interest to study the effects of excess $Bi_2O_3$ on the optical properties of the KNNLB ceramics. It is anticipated that the excess $Bi_2O_3$ can further suppress the grain growth of the KNNLB ceramics and then reduce the light scattering by the grains (at the grain boundaries). As excess $Bi_2O_3$ has also been shown to be effective in promoting liquid phase sintering and then densification (Du, 2007, Yu, 2008, Wu, 2010), the grains of the KNNLB may become more uniform after the addition of excess $Bi_2O_3$, which can also reduce the light scattering and hence enhance the optical properties of the ceramics. In this chapter, the effects of excess bismuth on the physical properties, in particular the optical and EO properties, of the KNNLB ceramics are investigated. $(K_{0.5}Na_{0.5})_{0.95}Li_{0.05}Nb_{0.95}Bi_{0.05}O_3$ (KNNLB-5) + y mol% excess $Bi_2O_3$ (y varying from 0 to 4) ceramics (abbreviated as KNNLB-5-y) sintered under a pressure of 10 MPa at 1060°C for 4 h are used for the investigation. The sintered ceramics were polished to 0.5mm with 1-μm diamond paste for the following measurements.

## 6.2 Crystalline Structure

The XRD patterns of the KNNLB-5-y ceramics are shown in Fig. 6.1. It is evident that all the KNNLB-5-y ceramics show a pure perovskite phase. Probably due to the small amount, no secondary phases relating to the excess $Bi_2O_3$ are observed. In fact, some of the excess $Bi_2O_3$ may evaporate during the process. Some of them may also diffuse into the KNN lattices, causing changes of the XRD patterns for the KNNLB-5-y ceramics.

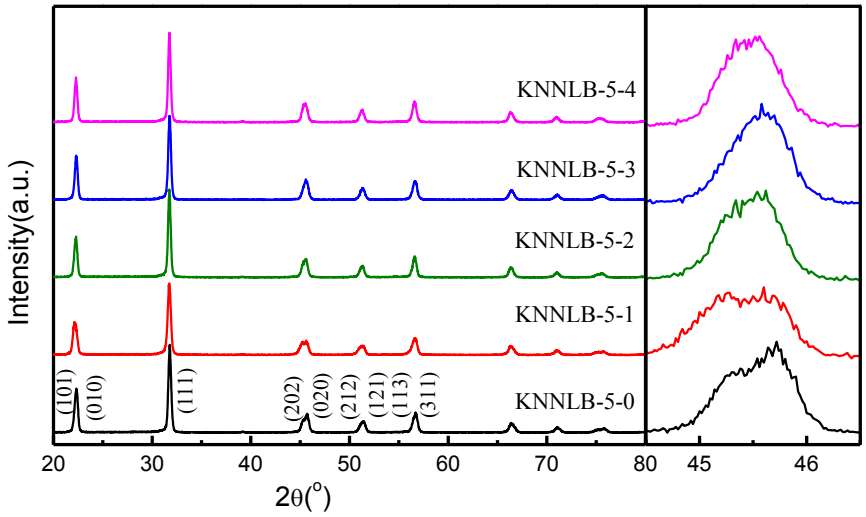


Figure 6.1 XRD patterns for the KNNLB-5-y ceramics.

As shown in Fig. 6.1, as y (the content of excess $Bi_2O_3$) increases, the merged peak of (202) and (020) in the $2\theta$ ranges of 44.5-46.5° becomes sharper. As discussed in the previous chapter, the merging of the (202) and (020) peaks is ascribed to the very similar lattice constants of the ceramics. The lattice constants of the ceramics were refined using all the diffraction peaks shown in Fig. 6.1 by the Rietveld method. Similar to the KNNLB-100x ceramics, a monoclinic *Pm* model was used in the refinement for the KNNLB-5-y ceramics. As shown in Table 6.1,

the lattice constants become closer as y increases. For the KNNLB-5-4 ceramic, the difference between *b* and *c* is only about 0.007Å. This indicates that the crystal structure of the ceramics with excess $Bi_2O_3$ becomes more cubic-like. This may be caused by the distortion of the lattices resulting from the diffusion of the excess Bi ions into the KNN lattice. Because of the similar radii, the excess $Bi^{3+}$ (0.96 Å) may diffuse into the A-sites to compensate the loss of the alkaline elements $Na^+$ (0.97 Å), $K^+$ (1.38 Å) as well as $Li^+$ (0.68 Å). However, owing to the different charges, A-site vacancies will be formed and hence lattice distortion may be resulted. The lattice strain arising from the different ion radii may also be resulted and attributed to the changes in lattice constants. Some of the excess $Bi^{3+}$ may also diffuse into the B-sites for compensating the loss of $Bi^{3+}$.

Table 6.1 Lattice constants *a*, *b* and *c* for the KNNLB-5-y ceramics.

| y | *a* (Å) | *b* (Å) | *c* (Å) | *β* (°) |
|---|---|---|---|---|
| 0 | 3.965 | 3.995 | 3.966 | 90.33 |
| 1 | 4.000 | 3.931 | 4.019 | 90.46 |
| 2 | 3.972 | 3.937 | 4.030 | 90.47 |
| 3 | 3.977 | 3.932 | 4.028 | 90.28 |
| 4 | 3.982 | 3.937 | 3.930 | 90.41 |

## 6.3 Microstructure

Fig. 6.2 shows the SEM micrographs of the thermally etched surfaces of the KNNLB-5-y ceramics while those of the fracture surfaces, as examples, are shown in Fig. 6.3. The density and average grain size of the KNNLB-5-y ceramics are exhibited in Table 6.2 and 6.3 separately.

Table 6.2 Density results for the KNNLB-5-y ceramics.

| y | 0 | 1 | 2 | 3 | 4 |
|---|---|---|---|---|---|
| Density ($g/cm^3$) | 4.57 | 4.55 | 4.57 | 4.59 | 4.70 |
| Relative density (%) | 98.1 | 98.1 | 98.3 | 98.5 | 98.7 |

Table 6.3 Average grain size for the KNNLB-5-y ceramics.

| y | 0 | 1 | 2 | 3 | 4 |
|---|---|---|---|---|---|
| Grain size (μm) | 0.67 | 0.64 | 0.56 | 0.57 | 0.59 |

It can be seen that all the ceramics possess a dense microstructure with basically identical grain shape and similar sizes. It seems that the excess $Bi_2O_3$ does not have significant effect on the grain growth of the ceramics, which is different from the previous research results (Wang, 2005). It has been shown that the excess Bi may aggregate at the grain boundaries impeding the grain growth and hence decrease the grain size (Nagata, 2005). In the KNNLB-5-y ceramics, some of the excess $Bi_2O_3$ may evaporate and some of them may diffuse into the KNN lattices resulting in the changes of the XRD patterns as shown in Fig. 6.1. Some of them may also aggregate at the grain boundaries. However, as the grains of the KNNLB-5-0 ceramic are already very small (< 0.7 μm, Table 6.3), the aggregation may not be able to further impede the grain growth and hence decrease the grain size. This also implies that there may exist a limit of the grain size prepared by the conventional mixed-oxides method.

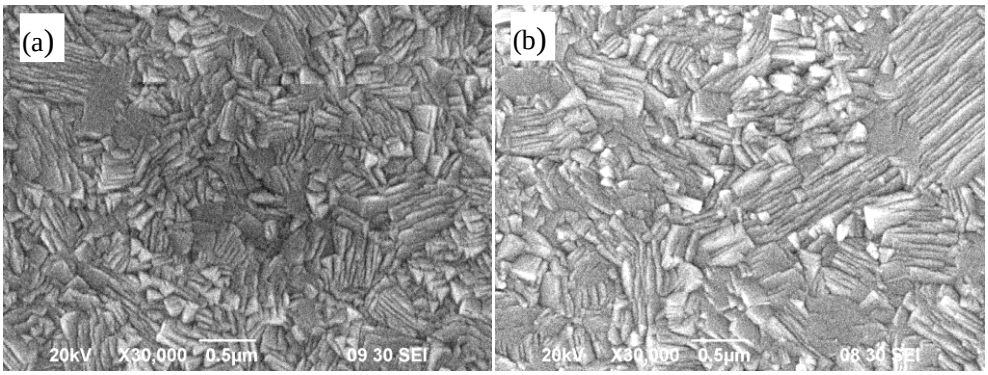


Figure 6.2 SEM images of the thermally etched surfaces of the KNNLB-5-y ceramics: (a) y=1; (b) y=3

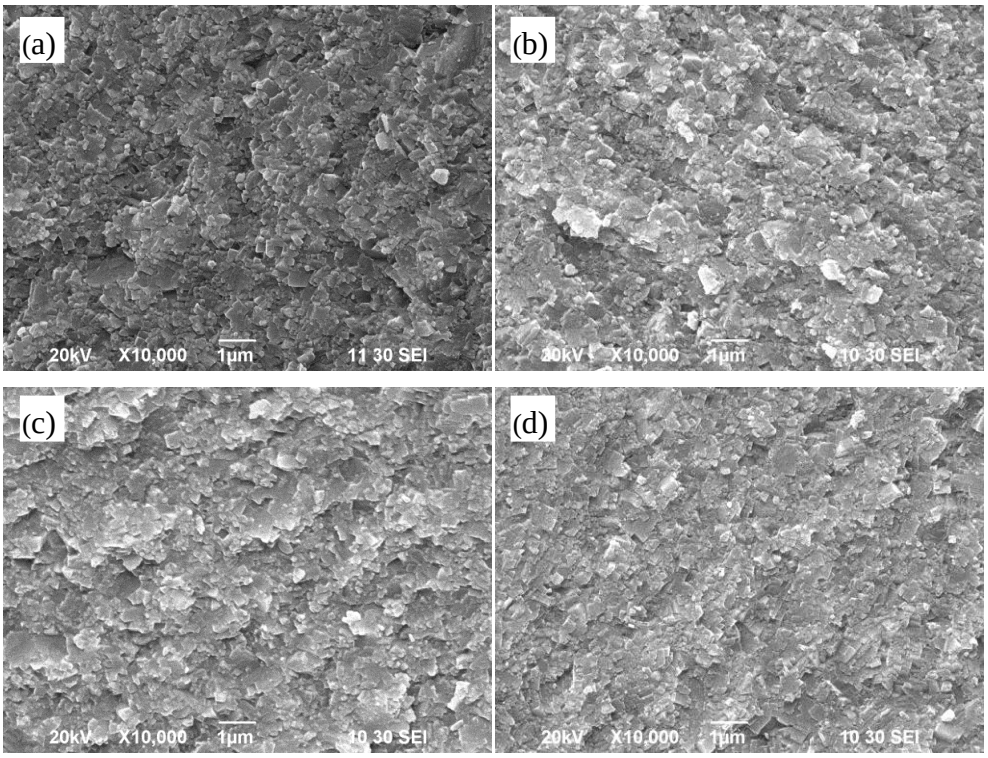


Figure 6.3 SEM images of the fracture surfaces of the KNNLB-5-y ceramics: (a) y=0; (b) y=1; (c) y=2; (d) y=4.

## 6.4 Optical Properties

Fig. 6.4 shows the photograph of the KNNLB-5-y ceramics, while their optical transmittances T measured in the range of 300-900 nm are shown in Figs. 6.5 and

6.6. As demonstrated in Fig. 6.4, all the KNNLB-5-y ceramics are optically transparent. The difference in optical transparency is not large and barely visible, which is also revealed in the optical transmittance spectra (Fig. 6.6).

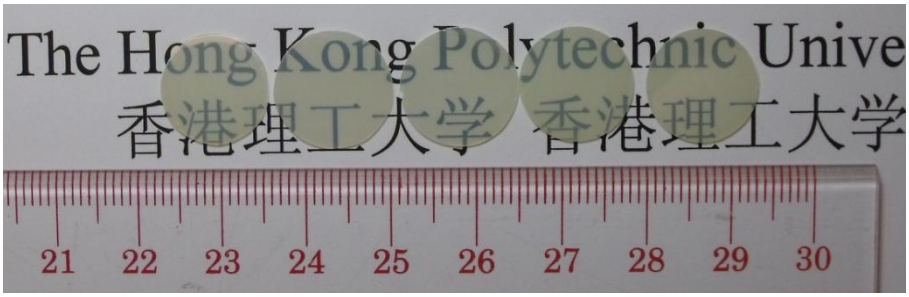


(a) (b) (c) (d) (e)

Figure 6.4 Photograph of the KNNLB-5-y transparent ceramics: (a) y=0; (b) y=1; (c) y=2; (d) y=3; (e) y=4.

As shown in Fig.6.5, the observed T (at any wavelength) increases slightly as y increases from 0 to 2, and then decreases with increasing y. For each ceramic, the observed T increases considerably from zero as the wavelength increases from ~390 nm, and then becomes almost saturated in the near-IR region (Fig. 6.6). As shown both in Figs. 6.5 and 6.6, the KNNLB-5-2 ceramic exhibits the highest transmittance in the wavelength range studied. This may be partly due to the more cubic-like crystal structure (Fig. 6.1), which would reduce the optical anisotropy and then the light scattering of the ceramic. The decrease in transmittance for the ceramics with y > 2 may be due to the slightly larger grains (Fig. 6.3). It should be noted that the observed optical transmittance is also strongly dependent on the polishing process which had been kept almost the same for all the ceramics in this work. On the basis of the

results, it is apparent that the excess $Bi_2O_3$ does not have significant effect on the optical properties of the KNNLB-5-y ceramics.

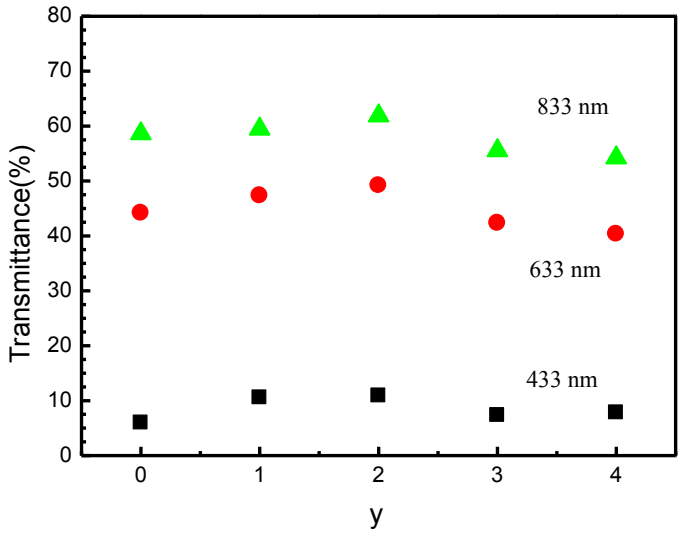


Figure 6.5 Optical transmittances measured at different wavelength for the KNNLB-5-y ceramics.

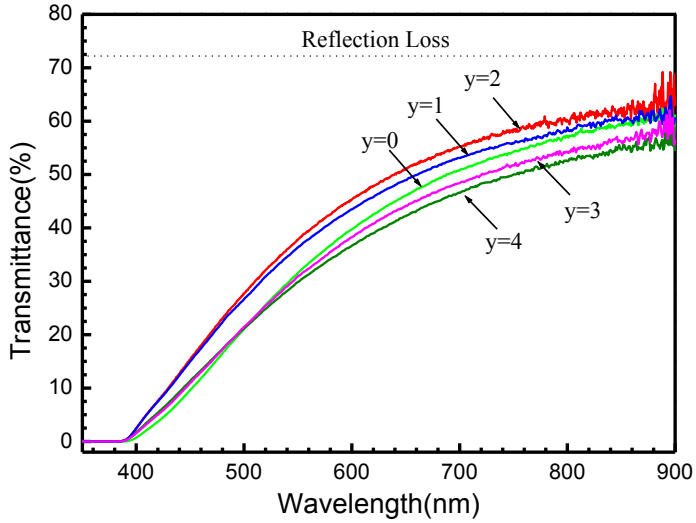


Figure 6.6 Optical transmittance spectra for the KNNLB-5-y ceramics.

Following similar procedures, the optical band gap energy $E_g$ for the KNNLB-5-y ceramics have been evaluated, giving the results listed in Table 6.4. It can be seen that the observed $E_g$ for the ceramics is very similar, ranging from 3.07 to 3.11, which is also close to the values obtained for the KNNLB-100x ceramics

(Table 5.1) and the value reported for KNN nanorods (3.09 eV) (Wang, 2010). It has been shown that the optical band gaps may be affected by the synthesis method, sample shape (powder, crystal or thin film) and synthesis conditions (Aguiar, 2011). For KNN, the band gap originates from a transition from the top of the valence bands occupied by $O_{2p}$ electron states to the bottom of the conduction bands dominated by the empty $Nb_{4d}$ electron states.

Table 6.4 Optical band gap energy $E_g$ for the KNNLB-5-y ceramics.

| y | 0 | 1 | 2 | 3 | 4 |
|---|---|---|---|---|---|
| $E_g$ (eV) | 3.09 | 3.07 | 3.11 | 3.09 | 3.09 |

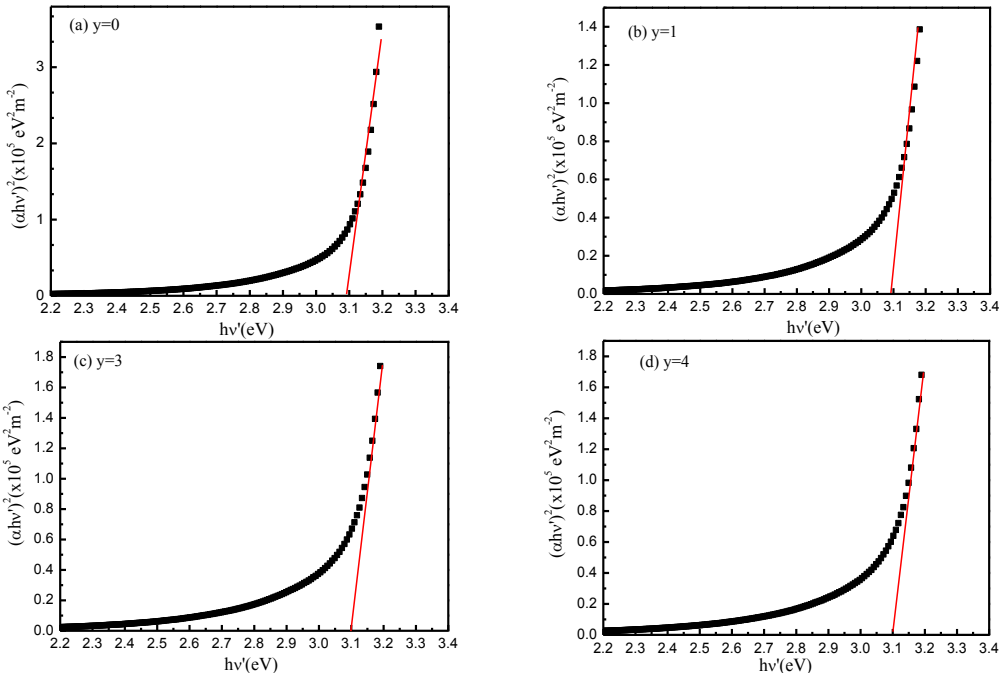


Figure 6.7 Plots of $(\alpha hv')^2$ versus $hv'$ for the KNNLB-5-y ceramics, from which the optical band gap energy $E_g$ obtained by extrapolating the linear region of the curve to zero.

## 6.5 Dielectric Properties

The temperature dependence of $\varepsilon_r$ for the KNNLB-5-y ceramics is shown in Fig. 6.8. Similarly, the observed $\varepsilon_r$ at 100 kHz are plotted for eliminating the effects of space-charge polarization at low frequencies and high temperatures. As y increases, the temperature of maximum $\varepsilon_r$ ($T_m$) decreases gradually and the cubic-tetragonal transition peak becomes more broadened (Fig. 6.8), indicating that the ceramic becomes more relaxor-like. This may be partly due to the diffusion of the excess $Bi^{3+}$ into the A-sites of the lattices. As $Bi^{3+}$ has a higher valence than $K^+$, $Na^+$ and $Li^+$, in order to preserve charge neutrality, the $Bi^{3+}$ ion would be accommodated by the formation of oxygen vacancies $V_{ö}$. Each dipolar defects is capable of polarizing a relatively large region around it, and thus favoring the formation of polar nano-regions and enhancing the relaxor-like characteristics (Shvartsman, 2012).

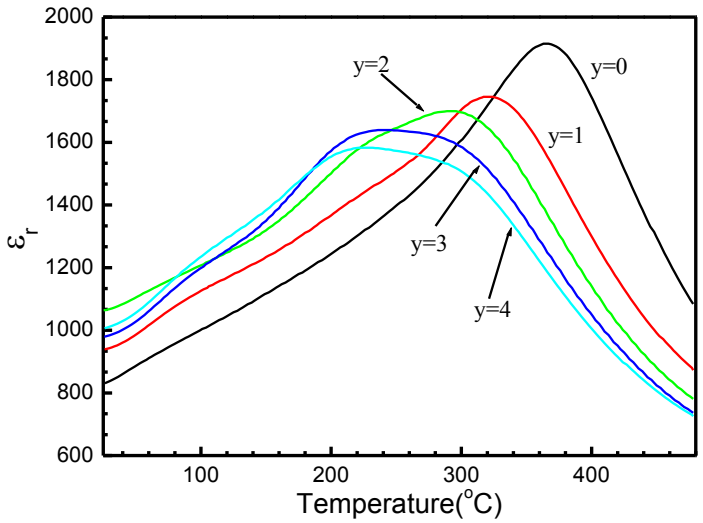


Figure 6.8 Temperature dependence of $\varepsilon_r$ for the KNNLB-5-y ceramics.

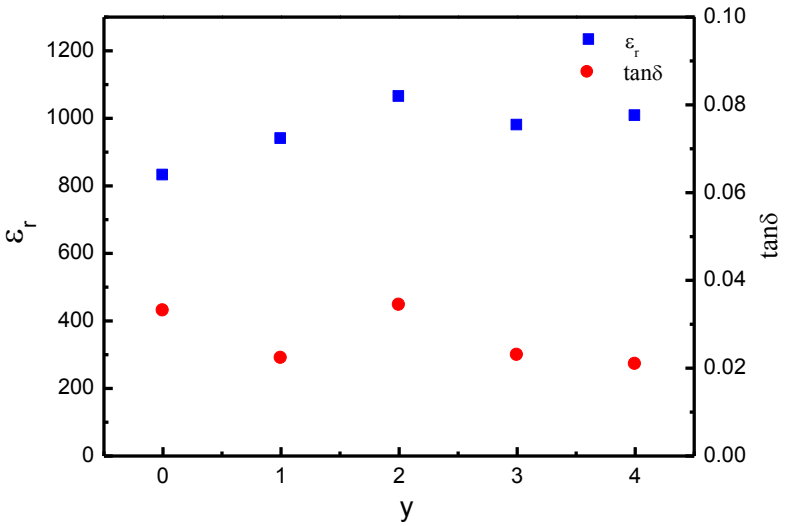


Figure 6.9 Variations of $\varepsilon_r$ and tanδ with y for KNNLB-5-y ceramics at room temperature and 100 kHz.

The dependences of $\varepsilon_r$ and tanδ on the Bi content at room temperature for the KNNLB-5-y ceramics are shown in Fig. 6.9. As y (i.e., the content of excess Bi) increases, the observed $\varepsilon_r$ increases from ~830 to ~1000 while the observed tanδ decreases slightly from 0.03 to 0.02. As discussed, some of the excess $Bi_2O_3$ may diffuse into the A-sites for compensating the loss of the alkaline elements, and some of them may also diffuse into the B-sites for compensating the loss of $Bi^{3+}$. As $Bi^{3+}$ has a higher valence than $K^+$, $Na^+$ and $Li^+$, the excess $Bi^{3+}$ may act as donor doponts, and thus causing the increase in $\varepsilon_r$. On the other hand, the compensation of B-site bismuth may reduce the oxygen vacancy concentration and hence the electrical conductivity.

## 6.6 Ferroelectric Properties

Fig. 6.10 shows the ferroelectric hysteresis (*P-E*) loops for the KNNLB-5-y ceramics. The *P-E* loops were measured at a frequency of 100 Hz under an electric field of 8.4 kV/mm at room temperature.

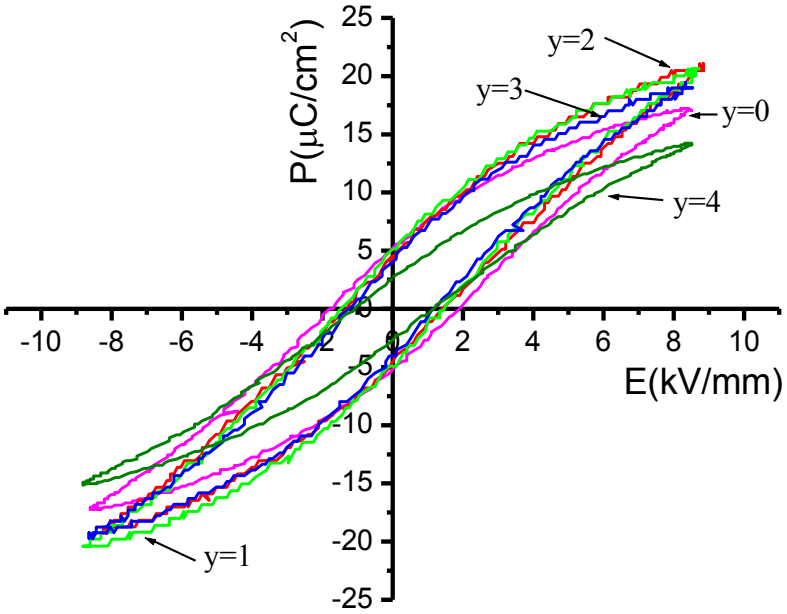


Figure 6.10 Hysteresis loops (at 100 Hz) of KNNLB-5-y ceramics at room temperature.

Probably due to the relaxor characteristics, all the ceramics exhibit a slant and flattened *P-E* loop. The observed remnant polarization $P_r$ and coercive field $E_c$ of the ceramics are presented in Fig. 6.11. The observed $P_r$ decreases with increasing y, giving a maximum value of ~5.2 μC/cm$^2$ at y = 0, while the observed $E_c$ decreases slightly as y increases. Similar to $\varepsilon_r$, the decrease in $P_r$ and $E_c$ may be partly attributed to the donor doping of $Bi^{3+}$ in the A-sites. However, as the ceramics become more cubic and relaxor-like, $P_r$ becomes decreased as y increases from 0.

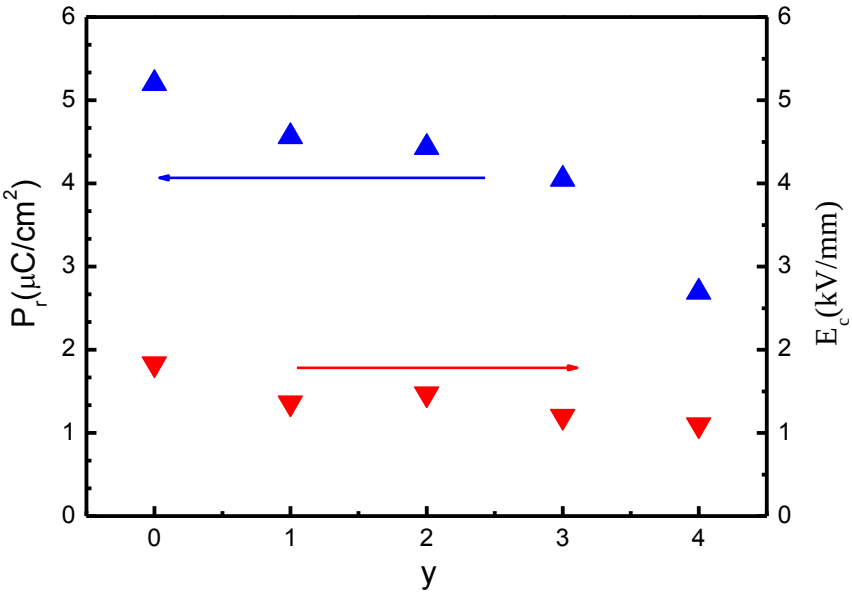


Figure 6.11 Variations of $P_r$ and $E_c$ for KNNLB-5-y ceramics at room temperature and 100 Hz.

## 6.7 Electro-Optic Properties

The effective linear EO coefficient $r_c$ of the KNNLB-5-y ceramics have been measured using the modified Sénarmont method, as introduced in chapter 3. The results are shown in Fig. 6.12. The ceramics were polarized under a d.c. field of 5kV/mm at 150$^o$C for 30 min, and the measurements were carried out one day after the poling. A $n_e$ value of 2.257 (approximated by the value of an un-poled sample) was used to calculate the $r_c$. (Eq. 3.34).

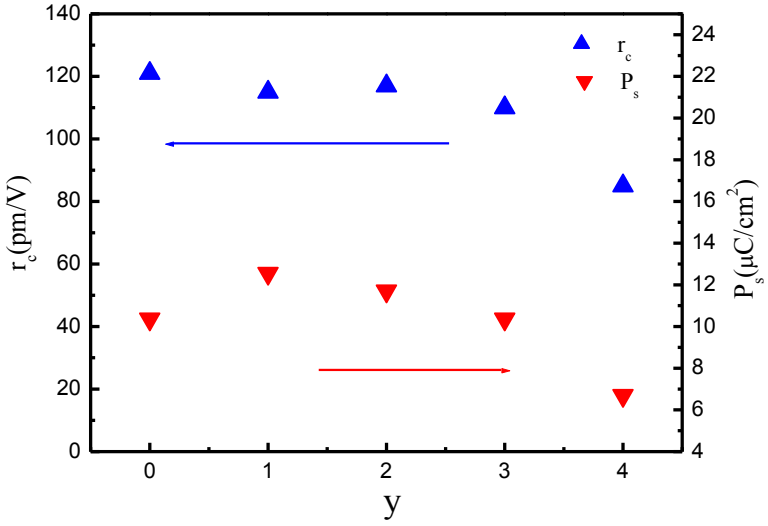


Figure 6.12 Variations of $r_c$ and $P_s$ (at room temperature) for the KNNLB-5-y ceramics.

As shown in Fig. 6.12, the observed $r_c$ remains almost unchanged at a value of ~120 pm/V as y increases from 0, and then starts to decrease at y = 3. According to Fig. 6.9 and Eq. 5.3 which states the relation between $r_c$ and $\varepsilon_r$, the observed $\varepsilon_r$ should increase with increasing y for the KNNLB-5-y ceramics. However, probably due to the change to a more cubic-like crystal structure (Fig. 6.1) and the increase in relaxor characteristics (Fig. 6.8), the observed $r_c$ remains almost unchanged at a value of ~120 pm/V as y increases from 0, and then starts to decrease at y = 3.

## 6.8 Conclusions

Lead-free transparent electro-optic ceramics $(K_{0.5}Na_{0.5})_{0.95}Li_{0.05}Nb_{0.95}Bi_{0.05}O_3$ + y mol% excess bismuth have been successfully fabricated by hot-press sintering. Our results reveal that the crystal structure of the ceramics with excess $Bi_2O_3$ becomes more cubic-like. The excess $Bi_2O_3$ does not have significant effect on the grain growth of the ceramics. And then, all the ceramics possess a dense

microstructure with basically identical grain shape and similar sizes. As a result, the KNNLB-5-y ceramics present similar optical property, indicating that the excess $Bi_2O_3$ does not have significant effect on the optical properties of the KNNLB-5-y ceramics. Partly due to the diffusion of the excess $Bi^{3+}$ into the A-sites of the lattices, the ceramics become more relaxor-like, and thus exhibiting a slant and flattened *P-E* loop. The KNNLB-5-y ceramics exhibit good EO response, giving a large effective linear EO coefficient $r_c$ ~120 pm/V. However, probably due to the change to a more cubic-like crystal structure and the increase in relaxor characteristics, the observed $r_c$ starts to decrease when the excess bismuth content is over 3%.

# Chapter7 Preparing Transparent EO Ceramics by Pressureless Sintering

## 7.1 Introduction

Transparent KNNLB ceramics have been successfully prepared by hot-press sintering, as introduced in previous chapters. The good optical clarity of the ceramics should be partly due to the reduced scattering of visible and IR lights by the fine grains (Apetz, 2003). It is believed that the fine grains are produced as a result of the effective suppression of the grain growth by the Bi-doping (Skidmore, 2010, Wang, 2004). Therefore, this suggests that the hot-press sintering technique may not be needed in preparing the new KNNLB transparent ceramics. In this chapter, the feasibility of preparing the transparent EO KNNLB ceramics by pressureless sintering is investigated. KNNLB-10-z ceramics, i.e., $(K_{0.5}Na_{0.5})_{0.9}Li_{0.1}Nb_{0.9}Bi_{0.1}O_3$ + z mol% excess $Bi_2O_3$, are mainly used for this investigation. The ceramics were sintered at 1060°C for 32 h under atmospheric pressure. The sintered ceramics were polished to 0.5mm with 1-μm diamond paste for the following measurements.

## 7.2 Optical Properties

Fig. 7.1 shows the photograph of the KNNLB-10-z ceramics with z = 0, 2, 4, 6, 8, while their optical transmittances T measured in the range of 350-900 nm are shown in Fig. 7.2.

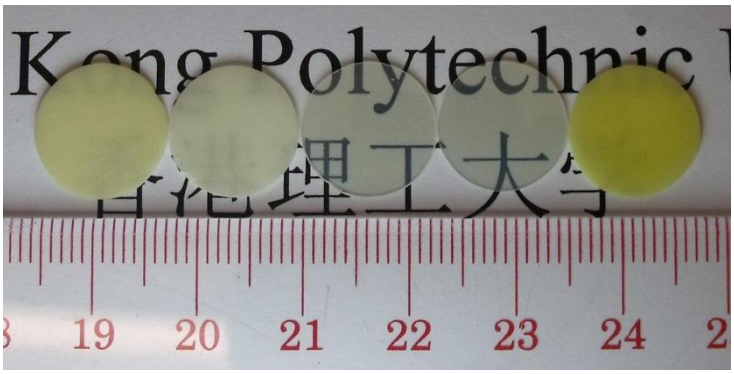


(a) (b) (c) (d) (e)

Figure 7.1 Photograph of the KNNLB-10-z ceramics with the thickness of 0.5mm: (a) z=0; (b) z=2; (c) z=4; (d) z=6; (e) z=8.

The excess Bi content plays an important role in the enhancement of the optical transparency. As demonstrated in Fig. 7.1, the KNNLB-10-4 and KNNLB-10-6 ceramics are transparent while the others are opaque. The difference in optical transparency is also revealed in the measured optical transmittance. As shown in Fig.7.2b, the observed T increases significantly as z increases from 2 to 4, and then decreases abruptly as z increases from 6 to 8. For the ceramics with z = 4 and 6, the transmittance begins to increase abruptly at around 390 nm, indicating an optical absorption edge in ultraviolet region, and becomes almost saturated in the near-IR region (Fig. 7.2a). It can also be seen that the KNNLB-10-6 ceramic exhibits the highest transmittance in the wavelength range studied. The observed T reaches a

very high value of ~70% in the near-IR region. If proper anti-reflection coating is applied to eliminate the reflection loss at the air-ceramic interfaces, the transmittance of the ceramic can exceed 95%.

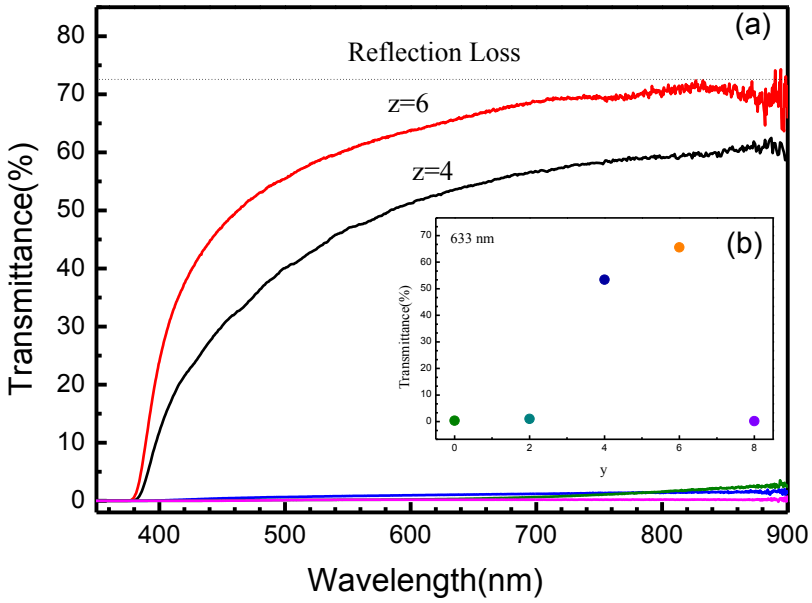


Figure 7.2 (a) Optical transmittance spectra for the KNNLB-10-z ceramics; (b) Optical transmittances measured at 633 nm for the KNNLB-10-z ceramics.

## 7.3 Crystalline Structure

Fig. 7.3 shows the X-ray diffraction patterns of the KNNLB-10-z ceramics at room temperature. It is evident that the KNNLB ceramics with $z \leq 6$ possess a single-phase perovskite structure. Probably due to the small amount, no secondary phases relating to the excess $Bi_2O_3$ are observed. Similar to the KNNLB-5-y ceramics prepared by hot-press sintering, some of the excess $Bi_2O_3$ may evaporate during the process and some of them may diffuse into the KNN lattices, causing changes of the XRD patterns for the KNNLB-10-z ceramics (Fig. 7.3).

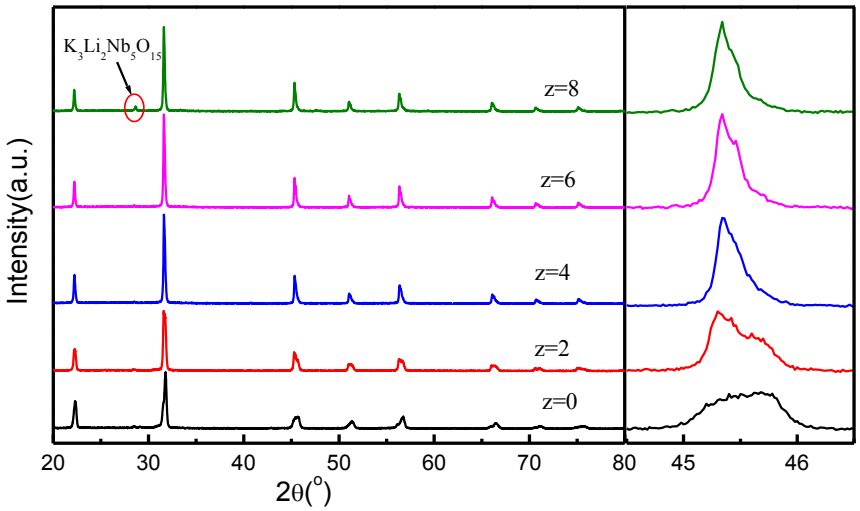


Figure 7.3 XRD patterns for the KNNLB-10-z ceramics.

As shown in Fig. 7.3, as z (the content of excess $Bi_2O_3$) increases, the merged peak of (202) and (020) in the $2\theta$ ranges of 44.5-46.5° becomes sharper. As discussed in the previous chapter, the merging of the (202) and (020) peaks is ascribed to the very similar lattice constants of the ceramics. The lattice constants of the ceramics were refined using all the diffraction peaks shown in Fig. 7.3 by the Rietveld method. Similar to the KNNLB-100x ceramics, a monoclinic *Pm* model was used in the refinement for the KNNLB-10-z ceramics. As shown in Table 7.1, the lattice constants become closer as z increases. For the KNNLB-10-6 ceramic, the difference between *b* and *c* is only about 0.011Å. This indicates that the crystal structure of the ceramics with excess $Bi_2O_3$ becomes more cubic-like, and hence the optical scattering arisen from birefringence should be reduced and the optical transparency could be improved. The change in the crystal structure may be caused by the distortion of the lattices resulting from the diffusion of the excess Bi ions into the KNN lattice. The XPS spectrum revealing the 3+ valance state of the Bi ions (Fujimoto, 2010) in the KNNLB-10-6 ceramic is shown in Fig. 7.4.

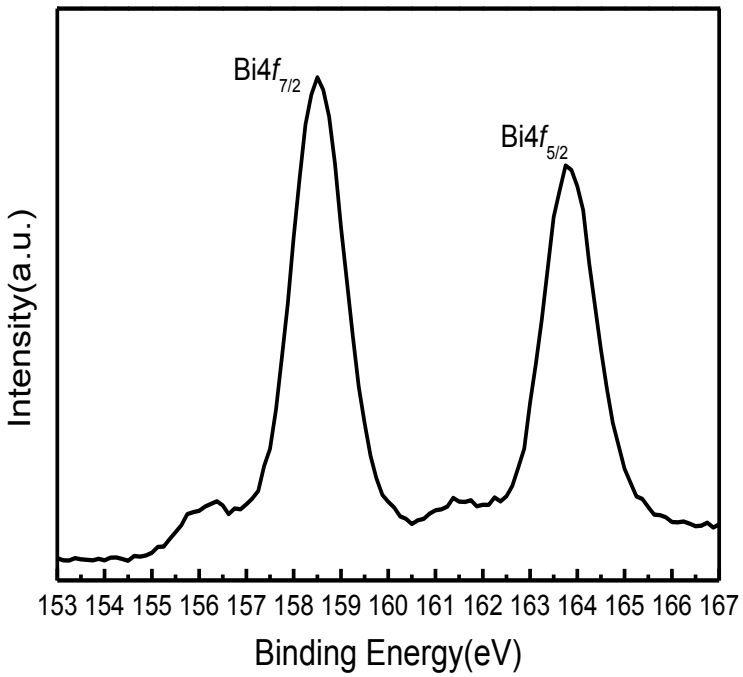


Figure 7.4 X-ray photoelectron spectroscopy (XPS) core-level spectrum of Bi4*f* for the KNNLB-10-6 ceramic.

Table 7.1 Lattice constants *a*, *b* and *c* for the KNNLB-10-z ceramics.

| z | *a* (Å) | *b* (Å) | *c* (Å) | *b*-*c* (Å) | *β* (°) |
|---|---|---|---|---|---|
| 0 | 3.985 | 3.964 | 4.005 | 0.041 | 90.39 |
| 2 | 3.976 | 3.985 | 4.000 | 0.015 | 90.15 |
| 4 | 3.975 | 3.991 | 3.993 | 0.002 | 90.25 |
| 6 | 3.996 | 3.986 | 3.997 | 0.011 | 90.01 |
| 8 | 3.996 | 3.990 | 3.998 | 0.008 | 90.01 |

For the KNNLB-10-8 ceramic, diffraction peaks relating to secondary phases are observed at around 28° (Fig.7.3). This may be ascribed to the volatilization losses of K, Na, Li and Bi, and may indicate that the solubility of Li decreases with increasing excess Bi. According to the PDF card (No. 34-0122), the secondary phase should be $K_3Li_2Nb_5O_{15}$ (Du, 2007). As discussed before, the scattering of light at

grains, grain boundaries, pores, and second-phase inclusions are the main factors affecting the transmittance of ceramics (Moulson, 2003, Grimm, 1971, Krell, 2006). Therefore, the poor optical transparency of the KNNLB-10-8 ceramic (Fig. 7.1) may be partly due to the light scattering at the secondary phase.

## 7.4 Microstructure

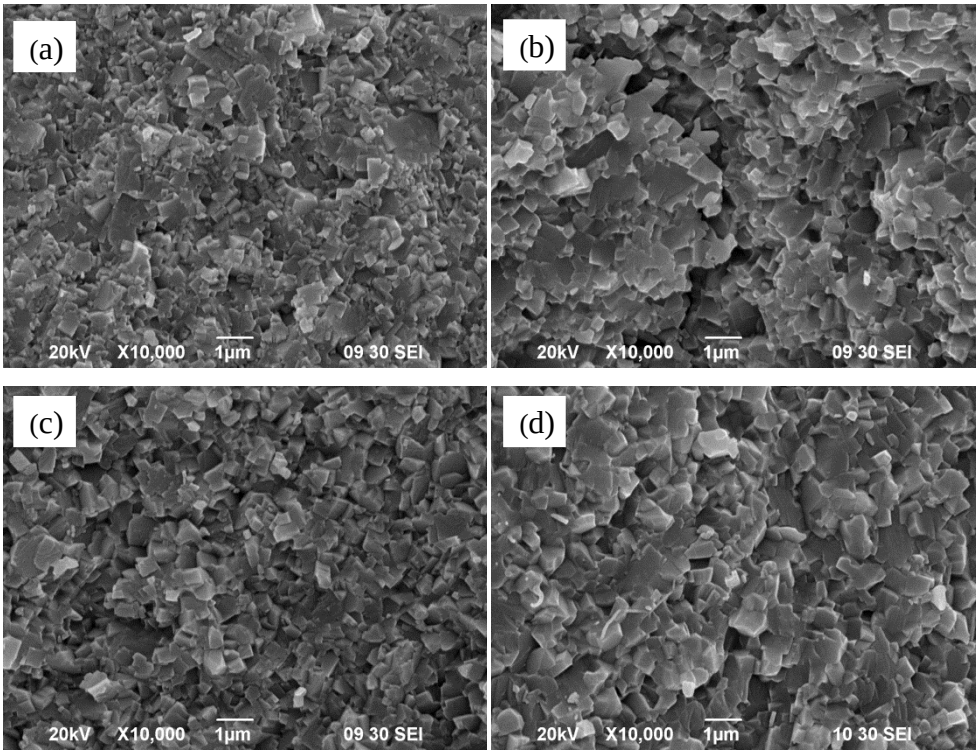


Figure 7.5 SEM images of the fracture surfaces of the KNNLB-10-z ceramics: (a) z=0; (b) z=2; (c) z=4; (d) z=6.

Fig. 7.5 shows the SEM micrographs for the fracture surfaces of the KNNLB-10-z ceramics with z = 0, 2, 4, 6. Characteristic quasi-cubic grains are observed randomly distributed in the ceramics. For all the ceramics, the grains are small, generally ~ 0.8 μm. The grain size decreases only slightly with increasing z,

as shown in Table 7.2. This suggests that the grain growth of the ceramics should be suppressed mainly by the Bi-doping (Skidmore, 2010, Wang, 2005, Aguiar, 2011), and the effect of excess $Bi_2O_3$ is small. Nevertheless, the densification of the ceramics improves and becomes more uniform with increasing z (the content of excess $Bi_2O_3$), as shown in Table 7.3. More pores are observed randomly distributed in the ceramics with z = 0 and 2.

Table 7.2 Average grain size for the KNNLB-10-z ceramics.

| z | 0 | 2 | 4 | 6 | 8 |
|---|---|---|---|---|---|
| Grain size (μm) | 0.87 | 0.84 | 0.84 | 0.81 | 0.73 |

Table 7.3 Density results for the KNNLB-10-z ceramics.

| z | 0 | 2 | 4 | 6 | 8 |
|---|---|---|---|---|---|
| Density ($g/cm^3$) | 4.29 | 4.33 | 4.49 | 4.48 | 4.49 |
| Relative density (%) | 90.1 | 91.2 | 94.5 | 94.7 | 95.1 |

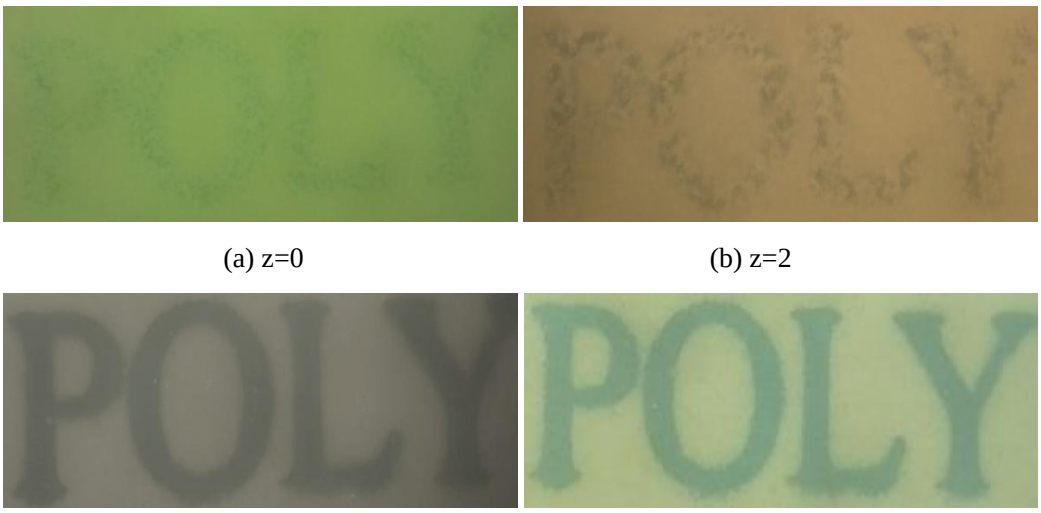


(a) z=0 (b) z=2

(c) z=4 (d) z=6

Figure 7.6 Photographs of the KNNLB-10-z ceramics.
(the letters covered by the samples are in 8 point Times New Roman font)

Owing to the light scattering at the pores, the optical transparency deteriorates and the ceramics become opaque, with a lot of white spots distributed in a transparent matrix as shown in Fig. 7.6. On the other hand, both the KNNLB-10-4 and KNNLB-10-6 ceramics possess a dense structure, which can reduce the optical scattering at the pores and then improve the optical transparency as shown in Figs. 7.1 and 7.6. On the basis of the results, it is suggested that the excess $Bi_2O_3$ may act as a sintering aid for promoting uniform densification under pressureless sintering. For the KNNLB ceramics, a large amount of excess $Bi_2O_3$ (e.g. > 4 mol%) is required for achieving uniform densification and then good optical properties.

## 7.5 Dielectric Properties

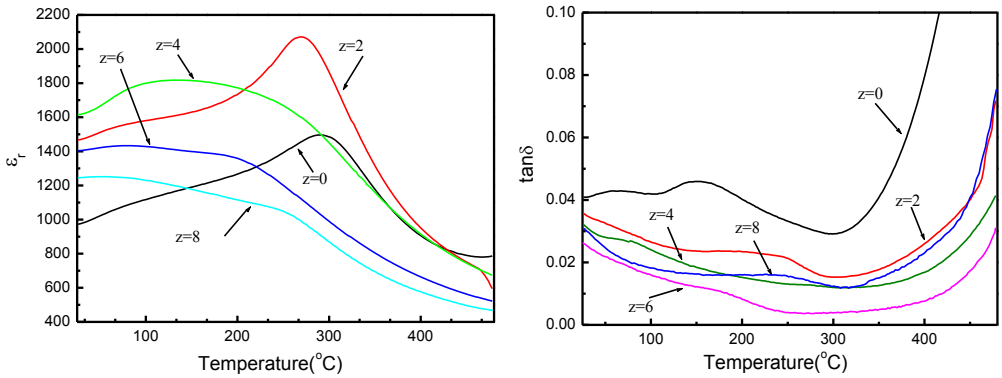


Figure 7.7 Temperature dependence of $\varepsilon_r$ and tanδ for the KNNLB-10-z ceramics at 100 kHz.

Fig. 7.7 shows the temperature dependence of the relative permittivity $\varepsilon_r$ for the KNNLB-10-z ceramics. Similarly, the observed $\varepsilon_r$ at 100 kHz data are plotted for eliminating the effects of space-charge polarization at low frequencies and high temperatures. As z increases, the temperature of maximum $\varepsilon_r$ ($T_m$) decreases

gradually and the cubic-tetragonal transition peak becomes more broadened (Fig. 7.7), indicating that the ceramic becomes more relaxor-like. This may be partly due to the diffusion of the excess $Bi^{3+}$ into the A-sites of the lattices. As $Bi^{3+}$ has a higher valence than $K^{+}$, $Na^{+}$ and $Li^{+}$, quenched random electric fields may be produced within the grains, and thus favoring the formation of polar nano-regions and enhancing the relaxor-like characteristics (Shvartsman, 2012). Owing to the increase in the polar nano-regions, the light scattering at the domain walls is reduced and hence the optical properties would be enhanced.

## 7.6 Ferroelectric Properties

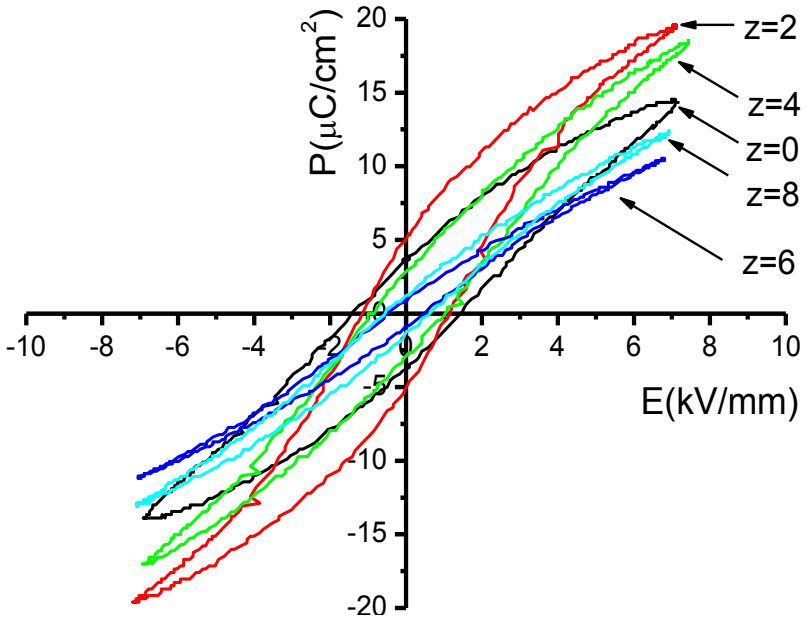


Figure 7.8 Hysteresis loops (at 100 Hz) of KNNLB-10-z ceramics at room temperature.

Fig. 7.8 shows the *P-E* loops for the KNNLB-10-z ceramics. The loops were measured at a frequency of 100 Hz under an electric field of 7 kV/mm. Probably due to the relaxor characteristics, all the ceramics exhibit a slant and flattened *P-E* loop.

The observed remnant polarization $P_r$ and coercive field $E_c$ of the ceramics are shown in Fig. 7.9. Probably due to the donor doping of $Bi^{3+}$ in the A-sites, the observed $P_r$ increases and $E_c$ decreases as z increases to 2. However, as the ceramics become more cubic and relaxor-like, $P_r$ starts to decrease at z > 2.

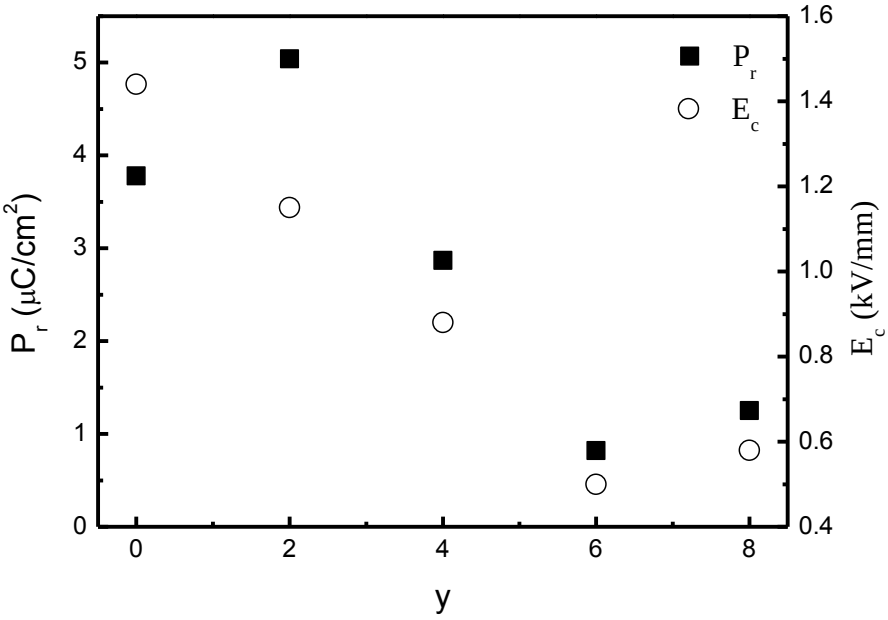


Figure 7.9 The composition dependence of $P_r$ and $E_c$.

## 7.7 Electro-Optic Properties

The effective linear EO coefficient $r_c$ of the KNNLB-10-4 and KNNLB-10-6 ceramics have been measured using the modified Sénarmont method, as introduced in chapter 3. The variations of the field-induced phase retardation $\Gamma_m$ (Eq. 3.28b) with the amplitude of an a.c. voltage at 1 kHz ($V_o$) for the ceramics are shown in Fig.7.10. It can be seen that a good linear relationship between $\Gamma_m$ and $V_o$, suggesting that the ceramics are linear EO materials. By using the fitted slop of the curves and a $n_e$ value of 2.257 (approximated by the value of an un-poled sample), $r_c$ for the

KNNLB-10-4 and KNNLB-10-6 ceramics are calculated as 40 pm/V and 29 pm/v, respectively. The low $r_c$ values of the ceramics should be attributed to the more cubic-like crystal structure and more relaxor-like characteristics.

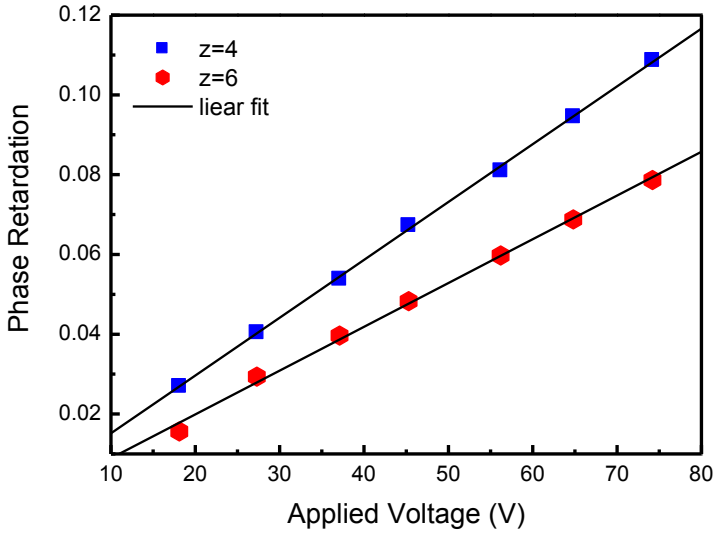


Figure 7.10 The plot of the phase retardations as a function of an a.c. applied field with a modulation frequency 1 kHz for the KNNLB-10-4 and KNNLB-10-6 ceramics.

## 7.8 Conclusions

Lead-free ceramics $(K_{0.5}Na_{0.5})_{0.9}Li_{0.1}Nb_{0.9}Bi_{0.1}O_3$ + z mol% excess $Bi_2O_3$ have been successfully prepared by pressureless sintering. Due to the effective suppression of the grain growth by the Bi-doping, the KNNLB-10-z ceramics prepared by pressureless sintering also possess a fine-grained structure. However, our results reveal that the excess $Bi_2O_3$ is effective in promoting uniform densification under pressureless sintering. Because of the reduction of defects such as pore, the KNNLB-10-4 and KNNLB-10-6 ceramics possess a dense structure and become optical transparent, exhibiting a high optical transmittance (60-70%) in the near-IR region. The good optical transparency may also be resulted from the changes to the more cubic-like crystal structure and more relaxor-like characteristics arisen from the diffusion of the excess $Bi^{3+}$ into the A-sites of the lattices. Nevertheless, the EO responses of the ceramics become weakened, showing a low effective linear EO coefficient of 40 pm/V and 29 pm/v, respectively.

# Chapter 8 Conclusions

New lead-free transparent ceramics $(K_{0.5}Na_{0.5})_{1-x}Li_xNb_{1-x}Bi_xO_3$ (KNNLB-100x) with good EO properties have been successfully developed. Via the co-modifications with Li and Bi, the optical transparency of potassium sodium niobate $(K_{0.5}Na_{0.5})NbO_3$ ceramics has been improved. The ceramics can be either prepared by hot-press sintering or pressureless sintering. The effects of the sintering pressure, and the content of $Li^+$, $Bi^{3+}$ as well as excess $Bi_2O_3$ on the optical, microstructure, dielectric and electro-optic properties of the ceramics have been investigated systematically.

Our results reveal that the sintering pressure is effective in improving the optical properties of the KNNLB-5-2 ceramics. It is found that a low pressure (e.g. 2 MPa) is enough to enhance the optical transmittance of the ceramics, and the optimum sintering pressure is about 10 MPa. Unlike the lead-based EO ceramics, the sintering pressure does not have significant effect on the grain growth. It is effective in improving the densification of the KNNLB ceramics. The enhancement in the optical transmittance should hence be partly due to the reduction of defects such as pores. Due to the better densification, the dielectric properties are also improved. However, the EO responses of the ceramics are not dependent on the sintering pressure. For the KNNLB-5-2 ceramic sintered under a pressure of 10 MPa, the optical transmittance and effective EO linear coefficient reach a high value of ~60% in the IR-region and ~115 pm/V, respectively.

After the co-modification with Li and Bi, the grain growth of the KNNLB-100x ceramics (sintered under a pressure of 10 MPa) is considerably suppressed. The ceramics generally possess a dense and fine-grained structure with the grain size below 0.7 μm. Our results also reveal that the co-modification induces a transformation of crystal structure from orthorhombic to nearly cubic. The co-modification also induces a diffuse phase transition, making the ceramics become more relaxor-like and contain more polar nano-regions. These would reduce the light scattering by the grains, at the grain boundaries and at the domain walls, respectively, and thus making the KNNLB-100x ceramics (with $x \geq 0.05$) become optically transparent. Owing to the large distortion of $BO_6$ octahedron and increase in $\varepsilon_r$ arisen from the substitution of $Li^+$ in the KNN lattices, the ceramics exhibit strong EO response, giving a large effective linear EO coefficient (120-200 pm/V), which is about 10 times greater than that of $LiNbO_3$ crystal (a widely used EO material in industries). The ceramics are also as good as the PMN-PT single crystals with rhombohedral structure and better than those with tetragonal structure.

Unlike the Bi-doping, the excess $Bi_2O_3$ does not have significant effect on the grain growth of the KNNLB-5 ceramics (prepared by hot-press sintering). All the ceramics possess a dense microstructure with basically identical grain shape and similar sizes. On the other hand, probably due to the diffusion of the excess $Bi^{3+}$ into the A-sites of the lattices, the crystal structure of the ceramics become more cubic and the ferroelectric behavior become more relaxor-like. Nevertheless, the optical transmittance and effect linear EO coefficient are not affected by the excess $Bi_2O_3$, remaining at a high value of 60% in the near-IR region and 120 pm/V, respectively.

Our result also reveal that the excess $Bi_2O_3$ is effective in promoting uniform densification of the KNNLB ceramics, making the preparation of transparent EO KNNLB ceramics by pressureless sintering become possible. Because of the reduction of defects such as pores, the KNNLB-10 ceramics added with 4 and 6mol% excess $Bi_2O_3$ possess a dense structure and become optical transparent, exhibiting a high optical transmittance (60-70%) in the near-IR region. The good optical transparency may also be resulted from the changes to the more cubic-like crystal structure and more relaxor-like characteristics arisen from the diffusion of the excess $Bi^{3+}$ into the A-sites of the lattices. Nevertheless, the EO responses of the ceramics become weakened, showing a low effective linear EO coefficient of 40 pm/V and 29 pm/v, respectively.

# References

http://en.wikipedia.org/wiki/Maxwell's_equations.

Aguiar, E. C., Simões, A. Z., Moura, F., Cilense, M., Longo, E. and Varela, J. A. "Piezoresponse force microscopy behaviour of $Bi_4Ti_3O_{12}$ ceramics with various excess bismuth." *Processing and Application of Ceramics* 5, no. 1 (2011): 1-11.

Ahn, Z. S. and Schulze, W. A. "Conventionally sintered $(Na_{0.5}\ K_{0.5})NbO_3$ with barium additions." *Journal of the American Ceramic Society* 70, no. 1 (1987): 18-21.

Aillerie, M., Fontana, M. D., Abdi, F., Carabatos-Nedelec, C., Theofanous, N. and Alexakis, G. "Influence of the temperature-dependent spontaneous birefringence in the electro-optic measurements of $LiNbO_3$." *Journal of Applied Physics* 65, no. 6 (1989): 2406.

Aillerie, M., Théofanous, N. and Fontana, M. D. "Measurement of the electro-optic coefficients: description and comparison of the experimental techniques." *Applied Physics B: Laser and Optics* 70, no. 3 (2000): 317-334.

Andreas, K., Thomas, H. and Jens, K. "Physics and Technology of Transparent Ceramic Armor:Sintered $Al_2O_3$ vs Cubic Materials." *Nanomaterials Technology for Military Vehicle Structural Applications.* Dresden, Germany, 2006. 14.

Apetz, R. and Bruggen, M. P. B. V. "Transparent Alumina: A Light-Scattering Model." *Journal of the American Ceramic Society* 86, no. 3 (2003): 480-486.

Bailey, A. E. "Ceramics and Glasses." In *Electronic Materials and Processes Handbook*, by Charles A. Harper. New York: McGraw-Hill Professional; 3rd edition, 2004.

Bass, M., Franken, P. A., Ward, J. F. and Weinreich, G. "Optical Rectification." *Physical Review Letters* 9, no. 11 (December 1962): 446-448.

Basu, B. and Balani, K. "Thermomechanical Sintering Methods." Chap. 6 in *Advanced Structural Ceramics*. New Jersey: John Wiley & Sons, Inc., 2011.

Birol, H., Damjanovic, D. and Setter, N. "Preparation and characterization of $(K_{0.5}Na_{0.5})NbO_3$ ceramics." *Journal of the European Ceramic Society* 26, no. 6 (2006): 861-866.

Bobnar, V., Bernard, J. and Kosec, M. "Relaxorlike dielectric properties and history-dependent effects in the lead-free $K_{0.5}Na_{0.5}NbO_3$–$SrTiO_3$ ceramic system." *Applied Physics Letters* 85, no. 6 (2004): 994.

Bokov, A. A. and Ye, Z. G. "Recent progress in relaxor ferroelectrics with perovskite structure." *Journal of Materials Science* 41, no. 1 (2006): 31-52.

Burns, G. and Smith, A. "Properties of new and useful tungsten-bronze niobates." *IEEE Journal of Quantum Electronics* 4, no. 10 (1968): 584-587.

Chen, Q., Chen, L., Li, Q., Yue, X., Xiao, D., Zhu, J., Shi, X. and Liu, Z. "Piezoelectric properties of $K_4CuNb_8O_{23}$ modified $(Na_{0.5}K_{0.5})NbO_3$ lead-free piezoceramics." *Journal of Applied Physics* 102, no. 10 (2007): 104109.

Clark, I. J., and McColm, N. J. *Forming, Shaping and Working of High Performance Ceramics.* first edition. New York: Blackie, 1988.

Cross, L. E. "Relaxor ferroelectrics." *Ferroelectrics* 76, no. 1 (1987): 241-267.

Dekker, M. *Ceramic materials for electronics.* Edited by Relva C. Buchanan. Marcel Dekker, 1991.

DrDomenico, M. and Wemple, S. H. "Oxygen-Octahedra Ferroelectrics. I. Theory of Electro-optical and Nonlinear optical Effects." *Journal of Applied Physics* 40, no. 2 (1969): 720.

Du, H. L., Li, Z. M., Tang, F. S., Qu, S. B., Pei, Z. B. and Zhou, W. C. "Preparation and piezoelectric properties of $(K_{0.5}Na_{0.5})NbO_3$ lead-free piezoelectric ceramics with pressure-less sintering." *Materials science & engineering. B, Solid-state materials for advanced technology* 131, no. 1-3 (2006): 83-87.

Du, H. L., Luo, F., Qu, S., Pei, Z. B., Zhu, D. M. and Zhou, W. C. "Phase structure, microstructure, and electrical properties of bismuth modified potassium-sodium niobium lead-free ceramics." *Journal of Applied Physics* 102, no. 5 (2007): 054102.

Du, H. L., Zhou, W., Luo, F., Zhu, D., Qu, S. and Pei, Z. "Perovskite lithium and bismuth modified potassium-sodium niobium lead-free ceramics for high temperature applications." *Applied Physics Letters* 91, no. 18 (2007): 182909.

Egerton, L. and Dillon, D. M. "Piezoelectric and Dielectric Properties of Ceramics in the System Potassium-Sodium Niobate." *Journal of The American Ceramic Society*

42, no. 9 (1959): 438-442.

Erling, R. and Thom, W. "Lead-free piezoceramics based on alkali niobates." *Journal of the European Ceramic Society* 25, no. 12 (2005): 2701-2706.

Ewsuk, K. G., Cesarano, J., Cochran, R. J., Blackwe, B. F. and Adkin, D. R. "Characterizing and Modeling Organic Binder Burnout from green ceramic compacts." *the 27th International SAMPE Technical Conference.* Albuquerque, NM,, 1995. 914-926.

Fang, W. B., Hu, L. X., He, W. X., Wang, E. D. and Li,X. Q. "Microstructure and properties of a TiAl alloy prepared by mechanical milling and subsequent reactive sintering." *Materials Science and Engineering: A* 403, no. 1-2 (2005): 186-190.

Fujimoto, Y. "Local Structure of the Infrared Bismuth Luminescent Center in Bismuth-Doped Silica Glass." *Journal of the American Ceramic Society*, 2010: 581-589.

Gonzaga, C. C., Cesar, P. F., Okada, C. Y., Federicci, C., Neto, F. B. and Yoshimura, H. N. "Mechanical properties and porosity of dental glass-ceramics hot-pressed at different temperatures." *Materials Research* 11, no. 3 (2008): 301-306.

Goovaerts, E., Wenseleers, W. E., Garcia, M. H. and Cross, G. H. "Handbook of Advanced Electronic and Photonic Materials and Devices." Chap. 3 in *Handbook of Advanced Electronic and Photonic Materials and Devices*, by Hari Singh Nalwa, 127-191. San Diego: Academic Press, 2001.

Grimm, N., Scott, G. E. and Sibold, J. D. "Infrared Transmission Properties of High-Density Alumina." *The Bulletin of the American Ceramic Society* 50, no. 12 (1971): 962-965.

Guo, Y. P., Kakimoto, K. and Ohsato, H. "$(Na_{0.5}K_{0.5})NbO_3$–$LiTaO_3$ lead-free piezoelectric ceramics." *Materials Letters* 59, no. 2-3 (2005): 241-244.

Guo, Y. P., Kakimoto, K. and Ohsato, H. "Phase transitional behavior and piezoelectric properties of $(Na_{0.5}K_{0.5})NbO_3$–$LiNbO_3$ ceramics." *Applied Physics Letters* 85, no. 18 (2004): 4121.

Guo, Y., Kakimoto, K. and Ohsato, H. "Phase transitional behavior and piezoelectric properties of $(Na_{0.5}K_{0.5})NbO_3$–$LiNbO_3$ ceramics." *Applied Physics Letters* 85, no. 18 (2004): 4121.

Haertling, G. H. "Properties of hot-pressed ferroelectric alkali niobate ceramics." *Journal of the American Ceramic Society* 50, no. 6 (1967): 329-330.

Hao, S. G., Zhou, G., Wang, X. S., Wu, J., Duan, W. H. and Gu, B. L. "Spontaneous polarizations of ultrashort-period epitaxial $KNbO_3$/$(KTaO_3)$m superlattices: An ab initio investigation." *Applied Physics Letters*, 2005: 232903.

Hartling, G. H. and Land, C. E. "Hot-Pressed $(Pb,La)(Zr,Ti)O_3$ Ferroelectric Ceramics for Electrooptic Applications." *Journal of the American Ceramic Society* 54, no. 1 (1971): 1-11.

Hartling, G. H. and Land, C. E. "Hot-Pressed $(Pb,La)(Zr,Ti)O_3$ Ferroelectric

Ceramics for Electrooptic Applications." *Journal of the American Ceramic Society* 54, no. 1 (1971): 1-11.

Hartling, G. H. "PLZT electro-optic materials and applications—a review." *Ferroelectrics* 75 (1987): 25-55.

He, C. J., Chen, H. B., Sun, L., Wang, J. M., Xu, F., Du, C. L., Zhu, K. J. and Liu, Y. W. "Effective electro-optic coefficient of $(1–x)Pb(Zn_{1/3}Nb_{2/3})O_3–xPbTiO_3$ single crystals." *Crystal Research and Technology* 47, no. 6 (2012): 610-614.

Hollenstein, E., Damjanovic, D. and Setter, N. "Temperature stability of the piezoelectric properties of Li-modified KNN ceramics." *Journal of the European Ceramic Society* 27, no. 13-15 (2007): 4093-4097.

Jaeger, R. E. and Egerton, L. "Hot-press of potassium sodium niobates." *Journal of the American Ceramic Society* 45, no. 5 (1962): 209-213.

Jiang, H., Zou, Y. K., Chen, Q., Li, K. K., Zhang, R., Wang, Y., Ming, H. and Zheng, Z. Q. "Transparent electro-optic ceramics and devices." *Proceedings of the SPIE* 5644 (2005): 380-394.

Kakimoto, Y. P. K. and Ohsato, H. "Phase transitional behavior and piezoelectric properties of $(Na_{0.5}K_{0.5})NbO_3–LiNbO_3$ ceramics." *Applied Physics Letters* 85, no. 18 (2004): 4121.

Keith, M. L. and Roy, R. "Structural Relations Among Double Oxides of Trivalent elements." *American Mineralogist* 39, no. 1-2 (1954): 1-23.

Kido, M., Tokuda, T., Wang, R. and Suzumura, F. "Influence of Additives and Hot-Press Sintering on Mechanical and Lipophilic Properties of Silicon Nitride Ceramics." *Materials Transactions* 46, no. 9 (2005): 2041-2046.

Kim, J. K., Wo, D. Z., Zhou, L. M., Huang, H. T., Lau, K. T. and Wang, M. "Electrical Properties of Hot Press Sintered NASICON Ceramics." *Key Engineering Materials* 334-335 (2007): 149-152.

Konuma, T., Nishi, T., Shimizu, M., Mori, H., Moriya, K.and Murakami, S. Liquid-Crystal Electro-optic Apparatus and Method of Manufacturing the Same. US Patent US 7561246 B2. July 14, 2009.

Kosec, M., Bobnar, V., Hrovat, M., Bernard, J., Malic, B. and Holc, J. "New lead-free relaxors based on the $K_{0.5}Na_{0.5}NbO_3$–$SrTiO_3$ solid solution." *Journal of Materials Research* 19, no. 06 (2004): 1849-1854.

Kosec, M., Malic, B., Bencan, A. and Rojac, T. "KNN-Based Piezoelectric Ceramics." In *Piezoelectric and Acoustic Materials for Transducer Applications*, edited by Safari A, 82. New York: Springer Science + Business Media, LLC, 2008.

Krell, A. Hutzler, T. and Klimke, J. "Physics and Technology of Transparent Ceramic Armor:Sintered Al2O3 vs Cubic Materials." *Nanomaterials Technology for Military Vehicle Structural Applications.* Dresden, Germany, 2006. 14.

Krell, A., Blank, P., Ma, H. W. and Hutzler, T. "Transparent Sintered Corundum with High Hardness and Strength." *J. Am. Ceram. Soc.*, 2003: 12-18.

Kroupa, J., Petzelt, J., Malic, B. and Kosec, M. "Electro-optic properties of KNN-STO lead-free ceramics." *Journal of Physics D: Applied Physics* 38, no. 5 (2005): 679-681.

Kuo, Y. H. "Enhanced thermal stability of electrooptic polymer Modulators using the diels-alder crosslinkable polymer." *Photonics Technology Letters, IEEE* 18, no. 1 (2006): 175-177.

Kwok, K. W., Li, F. L. and Lin, D. M. "A novel lead-free transparent ceramic with high electro-optic coefficient." *Functional Materials Letters* 4, no. 3 (2011): 237.

Li, H. D., Shih, W. H. and Shih, W. Y. "Synthesis of $Na_{0.5}K_{0.5}NbO_3$ Piezoelectrics by a Solution Coating Approach." *International Journal of Applied Ceramic Technology* 6, no. 2 (March 2009): 205-215.

Li, J. F., Wang, K., Zhang, B. P. and Zhang, L. M. "Ferroelectric and Piezoelectric Properties of Fine-Grained $Na_{0.5}K_{0.5}NbO_3$ Lead-Free Piezoelectric Ceramics Prepared by Spark Plasma Sintering." *Journal of the American Ceramic Society* 89, no. 2 (2006): 706-709.

Li, K., Li, F. L., Wang, Y., Kwok, K. W. and Chan, H. L. W. "Hot-pressed $K_{0.48}Na_{0.52}Nb_{1-x}Bi_xO_3$ (x = 0.05–0.15) lead-free ceramics for electro-optic applications." *Materials Chemistry and Physics* 131, no. 1-2 (2011): 320-324.

Lin D. M., Kwok, K. W. and Chan, H. L. W. "Dielectric and piezoelectric properties of $K_{0.5}Na_{0.5}NbO_3$–$AgSbO_3$ lead-free ceramics." *Journal of Applied Physics* 106, no.

3 (2009): 034102.

Lin D. M., Kwok,K.W. and Chan, H. L. W. "Microstructure, phase transition, and electrical properties of $(K_{0.5}Na_{0.5})_{1-x}Li_x(Nb_{1-y}Ta_y)O_3$ lead-free piezoelectric ceramics." *Journal of Applied Physics* 102, no. 3 (2007): 034102.

Lin, D. M., Kwok, K. W. and Chan, H. L. W. "Phase transition and electrical properties of $(K_{0.5}Na_{0.5})(Nb_{1-x}Ta_x)O_3$ lead-free piezoelectric ceramics." *Applied Physics A: Materials Science & Processing* 91, no. 1 (2008): 167-171.

Lin, D. M., Kwok, K. W. and Chan, H. L. W. "Structure, dielectric, and piezoelectric properties of CuO-doped $K_{0.5}Na_{0.5}NbO_3$–$BaTiO_3$ lead-free ceramics." *Journal of Applied Physics* 102, no. 7 (2007): 074113.

Ma, R. Z., Wu, J., Wei, B. Q., Liang, J. and Wu, D. H. "Processing and properties of carbon nanotubes–nano-SiC ceramic." *Journal of materials science* 33, no. 21 (1998): 5243-5246.

Maeder, M. D., Damjanovic, D. and Setter, N. "Lead Free Piezoelectric Materials." *Journal of Electroceramics* 13, no. 1-3 (2004): 385-392.

Matsubara, M., Yamaguchi, T., Kikuta, K. and Hirano, S. "Sinterability and Piezoelectric Properties of $(K,Na)NbO_3$ Ceramics with Novel Sintering Aid." *Japanese Journal of Applied Physics Part 1 - Regular Papers, Short Notes & Review Papers* 43, no. 10 (2004): 7259-7163.

MAUD. http://www.ing.unitn.it/~maud/index.html.

Mendelso, M. I. "Average Grain Size in Polycrystalline Ceramics." *J. Am.Ceram. Soc.*, 1969: 443-446.

Mgbemere, H. E., Hinterstein, M. and Schneider, G. A. "Electrical and structural characterization of $(K_xNa_{1-x})NbO_3$ ceramics modified with Li and Ta." *Journal of Applied Crystallography* 44, no. 5 (2011): 1080-1089.

Moulson, A. J. and Herbert, J. M. *Electroceramics: Materials, Properties, Applications.* 2nd edition. UK: Hoboken : John Wiley & Sons, Ltd, 2003.

Murata, M., Wakino, K., Tanaka, K. and Hamakawa, Y. "Chemical preparation of PLZT powder from aqueous solution." *Materials Research Bulletin* 11, no. 3 (1976): 323-327.

Nagata, H., Shinya, T., Hiruma, Y., Takenaka, T., Sakaguchi, I. and Haneda, H. "Piezoelectric Properties of Bismuth Sodium Titanate Ceramics." *Ceramic Transactions* 167 (2005): 213-222.

Naser, M. A., Zaliman, S., Uda, H. and Yarub, A-D. "Investigation of the absorption coefficient, refractive index, energy band gap, and film thickness for $Al_{0.11}Ga_{0.89}N$, $Al_{0.03}Ga_{0.97}N$, and GaN by optical transmission method." *Int. J. Nanoelectronics and Materials* 2, no. 2 (2009): 189-195.

Newnham, R. E. "Tunable Transducers: Nonlinear Phenomena in Electroceramics." *National Institute of Standards and Technology Special Publication 804* 19 (1991): 39-52.

Nye, J. F. *Physical Properties of Crystals.* London: Oxford Science Publications, 1976.

Park, H. Y., Ahn, C. W., Cho, K. H., Nahm, S., Lee, H. G., Kang, H. W., Kim, D. H. and Park, K. S. "Low-Temperature Sintering and Piezoelectric Properties of CuO-Added 0.95($Na_{0.5}K_{0.5}$)$NbO_3$-0.05$BaTiO_3$ Ceramics." *Journal of the American Ceramic Society* 90, no. 12 (2007): 4066-4069.

Park, H. Y., Ahn, C. W., Song, H. C., Lee, J. H., Nahm, S., Uchino, K., Lee, H. G. and Lee, H. J. "Microstructure and piezoelectric properties of 0.95($Na_{0.5}K_{0.5}$)$NbO_3$–0.05$BaTiO_3$ ceramics." *Applied Physics Letters* 89, no. 6 (2006): 062906.

Park, S. J., Park, H. Y., Cho, K. H., Nahm, S., Lee, H. G., Kim, D. H. and Choi, B. H. "Effect of CuO on the sintering temperature and piezoelectric properties of lead-free 0.95($Na_{0.5}K_{0.5}$)$NbO_3$–0.05$CaTiO_3$ ceramics." *Materials Research Bulletin* 43, no. 12 (2008): 3580-3586.

Pockels, F. *Ueber den Einfluss des elektrostatischen Feldes auf das optische Verhalten piezoelektrischer Krystalle.* Gottingen: Dieterichsche Verlags-Buchhandlung, 1894.

Ran, M. W., Chen, X. F. and Cao, Z. Q. "Measurement of Quadratic Electro-Optic Coefficient of PMN-PT Transparent Ceramics Based on Ultrahigh-Order Guide Modes." *Acta Optica Sinica* 31, no. 10 (2011): 1012002.

Reed, J. S. *Introduction to the Principals of Ceramic Processing.* New York: John Wiley & Sons, 1988.

Retherford, R. S., Sabia, R. and Sokira, V. P. "Effect of surface quality on transmission performance for (111) $CaF_2$." *Applied Surface Science* 183, no. 3-4 (2001): 264-269.

Richerson, D. W. *Modern Ceramic Engineering.* second edition. New York: Marcel Dekker, Inc, 1992.

Ringgaard, E. and Wurlitzer, T. "Lead-free piezoceramics based on alkali niobates." *Journal of the European Ceramic Society* 25, no. 12 (2005): 2701-2706.

Rubio-Marcos, F., Ochoa, P. and Fernandez, J. F. "Sintering and properties of lead-free (K,Na,Li)(Nb,Ta,Sb)$O_3$ ceramics." *Journal of the European Ceramic Society*, 2007: 4125-4129.

Rubio-Marcos, F., Romero, J. J., Mart ń-Gonzalez, M. S. and Fern ández, J. F. "Effect of stoichiometry and milling processes in the synthesis and the piezoelectric properties of modified KNN nanoparticles by solid state reaction." *Journal of the European Ceramic Society* 30, no. 13 (2010): 2763-2771.

Saito, Y., Takao, H., Tani, T., Nonoyama, T., Takatori, K.,Homma, T., Nagaya, T. and Nakamura, M. "Lead-free piezoceramics." *Nature* 432, no. 7013 (2004): 84-87.

Samara, G. A. "The relaxational properties of compositionally disordered $ABO_3$ perovskites." *Journal of Physics-condensed Matter*, 2003: R367-R411.

Santos, I. A., Endo, C., Zanin, A. L., Lente, M. H., Eiras, J. A. and Garcia, D. "Hot-pressed transparent PLZT ceramics from low cost chemical processing." *Materials Research* 4, no. 4 (2001): 291-295.

Sawyer, C. B., and Tower, C. H. "Rochelle salt as a dielectric." *PhysicalL Review* 35, no. 3 (1930): 269-273.

Senyshyn, A. Ehrenberg, H. Vasylechko, L. Gale, J. D. and Bismayer, U. "Computational study of $LnGaO_3$ (Ln=La–Gd) perovskites." *Journal of Physics: Condensed Matter* 17, no. 39 (2005): 6217.

Shih, C. C. and Yariv, A. "A theoretical model of the linear electro-optic effect." *Journal of Physics C: Solid State Physics* 15, no. 4 (1982): 825-846.

Shirane, G., Newnham, R. and Pepinsky, R. "Dielectric properties and phase transitions of NaNbO3 and $(Na,K)NbO_3$." *Physical Review* 96, no. 3 (1954): 581-588.

Shiratori, Y., Magrez, A. and Pithan, C. "Particlesizeeffect on the crystalstructure symmetry of $K_{0.5}Na_{0.5}NbO_3$." *Journal of the European Ceramic Society*, 2005: 2075-2079.

Shrout, T. R., Chang, Z. P., Kim, N. and Markgraf, S. "Dielectric behavior of single crystals near the $(1-x)Pb(Mg_{1/3}Nb_{2/3})O_3$-$(x)PbTiO_3$ morphotropic phase boundary." *Ferroelectrics Letters Section* 12, no. 3 (1990): 63-69.

Shvartsman, V. V. and Lupascu, D. C. "Lead-free relaxor ferroelectrics." *Journal of*

*the American Ceramic Society*, January 2012: 1-26.

Singh, K. C., Jiten, C., Laishram, R., Thakur, O. P. and Bhattacharya, D. K. "Structure and electrical properties of Li- and Ta-substituted $K_{0.5}Na_{0.5}NbO_3$ lead-free piezoelectric ceramics prepared from nanopowders." *Journal of Alloys and Compounds* 496, no. 1-2 (2010): 717-722.

Sinyukov, A. M. and Hayden, L. M. "Efficient Electrooptic Polymers for THz Applications." *The Journal of Physical Chemistry B* 108, no. 25 (May 2004): 8515-8522.

Skidmore, T. A., Comyn, T. P. and Milne, S. J. "Dielectric and Piezoelectric Properties in the System: $(1-x)[(Na_{0.5}K_{0.5}NbO_3)_{0.93}–(LiTaO_3)_{0.07}]–x[BiScO_3]$." *Journal of the American Ceramic Society* 93, no. 624-626 (2010): 624-626.

Smolenskii, G. A. and Agronovskaya, A. I. "Dielectric Polarization and Losses of Some Complex Compounds." *Soviet Physics Technical Physics* 3, no. 7 (1958): 1380-1382.

Snow, G. S. "Fabrication of Transparent Electrooptic PLZT Ceramics by Atmosphere Sintering." *Journal of the American Ceramic Society* 56, no. 2 (1973): 91-96.

Stojanovic, B. D. Zaghete, M. A. Paiva-Santos, C. O. Cilense, M. Magnani, R. Longo, E. and Varela, J. A. "Hot-pressed 9.5/65/35 PLZT prepared by the polymeric precursor method." *Ceramics International* 26, no. 6 (2000): 625-630.

Stojanovic, B. D., Zaghete, M. A., Foschini, C. R., Cavalheiro, A. A., Paiva-Santos,

C. O., Cilense, M., Longo, E. and Varela, J. A. "Synthesis and characterization of 9.5/65/35 PLZT prepared from the polymeric precursors." *Materials Chemistry and Physics* 67, no. 1-3 (2001): 282-287.

Tauc, J. and Menth, A. "States in the gap." *Journal of Non-Crystalline Solids* 8-10 (1972): 569-585.

Tellier, J., Malic, B., Dkhil, B., Jenko, D., Cilensek, J. and Kosec, M. "Crystalstructure and phasetransitions of sodiumpotassiumniobateperovskites." *Solid State Sciences*, 2009: 320-324.

Thomson, J. "Chemical Preparation of PLZT Powders from Aqueous Nitride Solution." *American Ceramic Society Bulletin* 53 (1974): 421-433.

Uchino, K. ,. *Piezoelectric Actuators and Ultrasonic Motors*,. Boston: Kluwer Academic Publishers,, 1996.

Uchino, K. and Nomura, S. "Critical Exponents of the Dielectric Constants in. Diffused-Phase-Transition Crystals." *Ferroelectrics* 44, no. 3 (1982): 55-61.

Uchino, K. "Electro-optic Devices." In *Ferroelectric Devices*, 221. New York: Marcel Dekker, Inc, 2000.

Uchino, K., Nomura, S., Cross, L. E., Jang, S. J. and Newnham, R. E. "Electrostrictive effect in lead magnesium niobate single crystals." *Journal of Applied Physics* 51, no. 2 (1980): 1142.

Viswanathan, V., Laha, T., Balani, K., Agarwal, A. and Seal, S. "Challenges and

advances in nanocomposite processing techniques." *Challenges and advances in nanocomposite processing techniques* 54, no. 5-6 (2006): 121-285.

Wan, X. M., Luo, H. S., Zhao, X. Y., Wang, D. Y., Chan, H. L. W. and Choy, C. L. "Refractive indices and linear electro-optic properties of $(1-x)Pb(Mg_{1/3}Nb_{2/3})O_3-xPbTiO_3$ single crystals." *Applied Physics Letters* 85, no. 22 (2004): 5233.

Wang, R. P., Xie, R. J., Sekiya, T. and Shimojo, Y. "Fabrication and characterization of potassium–sodium niobate piezoelectric ceramics by spark-plasma-sintering method." *Materials Research Bulletin* 39, no. 11 (2004): 1709-1715.

Wang, R. P., Xie, R. J., Sekiya, T., Shimojo, Y., Akimune, Y., Hirosaki, N. and Itoh, M. "Piezoelectric Properties of Spark-Plasma-Sintered $(Na_{0.5}K_{0.5})NbO_3$–$PbTiO_3$ Ceramics." *Japanese Journal of Applied Physics* 41, no. 11B (2002): 7119-7122.

Wang, X. X., Kwok, K. W., Tang, X. G., Chan, H. L. W. and Choy, C. L. "Electromechanical properties and dielectric behavior of $(Bi_{1/2}Na_{1/2})_{(1-1.5x)}Bi_xTiO_3$ lead-free piezoelectric ceramics." *Solid State Communications* 129, no. 5 (2004): 319-323.

Wang, X. X., Tang, X. G., Kwok, K. W., Chan, H. L. W. and Choy, C. L. "Effect of excess $Bi_2O_3$ on the electrical properties and microstructure of $(Bi_{1/2}Na_{1/2})TiO_3$ ceramics." *Applied Physics A: Materials Science & Processing*, February 2005: 1071-1075.

Wang, Y., Li, Y. X., Kalantar-zadeh, K., Wang, T. B., Wang, D. and Yin, Q. R. "Effect of $Bi^{3+}$ ion on piezoelectric properties of $K_xNa_{1-x}NbO_3$." *Journal of Electroceramics* 21, no. 1-4 (2008): 629-632.

Wang, Z. , Gu, H. S., Hu, Y. M., Yang, K., Hu, M. Z., Zhou, D. and Guan, J. G. "Synthesis, growth mechanism and optical properties of (K,Na)$NbO_3$ nanostructures." *CrystEngComm* 12, no. 10 (2010): 3157-3162.

Wei, X. Y., Feng, Y. J. and Yao, X. "Dielectric relaxation behavior in barium stannate titanate ferroelectric ceramics with diffused phase transition." *Applied Physics Letters*, 2003: 2031.

Wood, E. A. "Polymorphism in potassium niobate, sodium niobate, and other $ABO_3$ Compounds." *Acta Crystallographica* 4, no. 4 (1951): 353-362.

Wu, L., Zhang, J. L., Wang, C. L. and Li, J. C. "Influence of compositional ratio K/Na on physical properties in $(K_xNa_{1-x})NbO_3$ ceramics." *Journal of Applied Physics*, 2008: 084116.

Wu, S. H., Wei, X. S., Wang, X. Y., Yang, H. X. and Gao, S. Q. "Effect of $Bi_2O_3$ Additive on the Microstructure and Dielectric Properties of $BaTiO_3$-Based Ceramics Sintered at Lower Temperature." *Journal of Materials Science & Technology*, 2010: 472-476.

Yokosuka, M., Ochiai, T. and Marutake, M. "$Ba(La_{1/2}Nb_{1/2})O_3$-$PbZrO_3$-$PbTiO_3$ Ferroelectric Ceramics." *Japanese Journal of Applied Physics* 31 (1992): 3170-3173.

Yu, Z., Sun, K., Li, L. Z., Liu, Y. F., Lan, Z. W. and Zhang. H. W. "Influences of $Bi_2O_3$ on microstructure and magnetic properties of MnZn ferrite." *Journal of Magnetism and Magnetic Materials*, March 2008: 919-923.

Zang, G. Z., Wang, J. P., Chen, H. C., Su, W. B., Wang, C. M., Qi, P., Ming, B. Q., Du, J., Zheng, L. M., Zhang, S. Z. and Shrout, T. R. "Perovskite $(Na_{0.5}K_{0.5})_{1-x}(LiSb)_xNb_{1-x}O_3$ lead-free piezoceramics." *Applied Physics Letters* 88, no. 21 (2006): 212908.

Zhang, W., Lu, T. C., Wei, N., Wang, Y. Z., Ma, B., Li, F., Lu, Z. W. and Qi, J. "Assessment of light scattering by pores in Nd:YAG transparent ceramics." *Journal of Alloys and Compounds* 520 (2012): 36-41.

Zou, K. Y., Chen, Q. S., Li, K. W. K., Zhang, R. and Jiang, H. "Characterization of new electro-optic ceramics." *Proc . CLEO 2004.* San Francisco, California, 2004. CWA31.

Zuo, R. Z., Ye, C. and Fang, X. S. "$Na_{0.5}K_{0.5}NbO_3$–$BiFeO_3$ lead-free piezoelectric ceramics." *Journal of Physics and Chemistry of Solids* 69, no. 1 (2008): 230-235.